UNIVERSIDADE D
COIMBRA

Andreia Sofia Feitor Gaudêncio

# Entropy measure algorithms for biomedical applications

Dissertação no âmbito do Mestrado Integrado em Engenharia Biomédica, em Instrumentação Biomédica, orientada pelo Professor Doutor João Manuel Rendeiro Cardoso e pela Professora Doutora Anne Marie Humeau-Heurtier e apresentada à Faculdade de Ciências e Tecnologias da Universidade de Coimbra.

Setembro de 2019

1 2 9 0
FACULDADE DE CIÊNCIAS E TECNOLOGIA
UNIVERSIDADE D COIMBRA

# Entropy measure algorithms for biomedical applications

Andreia Sofia Feitor Gaudêncio

Thesis submitted to the University
of Coimbra for the degree of Master
in Biomedical Engineering

*Supervised by PhD Professor João Manuel Rendeiro Cardoso (LIBPhys-UC, University of Coimbra, Portugal) and PhD Professor Anne Humeau-Heurtier (LARIS, University of Angers, France)*

**September, 2019**

This work was developed in collaboration with:

LIBPhys-UC



*À minha família e amigos...*

*"The good things of prosperity are to be wished;*
*but the good things that belong to adversity are to be admired"*
***Lucius Annaeus Seneca***

# Acknowledgments

I would like to begin by thanking Angers. What an amazing city that welcome me so well. The very first person I would like to thank is Professor Anne Humeau-Heurtier, who was amazing not only during my stay in Angers but throughout my entire academic year. I had the opportunity to work with an extraordinary teacher that helped me whenever I needed.

When I mention Angers and my work in this amazing city, I must mention Mirvana Hilal. Mirvana was incredible with me, always ready to provide advices so I could improve my work and available to discuss goals and results. My stay in France was not that scary since you helped a lot in that way by receiving me, having those nice lunches and showing me around the beautiful Angers castle. In addition, I also must thank Therese, Stephanie and Mohamed for letting me know a bit more about Lebanon. To finish, I also want to thank the other lab's members for welcoming me so well.

To complete my enormous thanking note to Angers, I must thank so much the Anjou Derby Girls (ADG) team that made me their friend from day one. My journey without a doubt was extraordinary because of our adventures together namely all the games and showing me around new places. It was amazing to make part of such a wonderful team. Being able to share the team's evolution and being able to improve myself as a team member due to your advices and techniques was awesome!!! I can not wait for the day I will be joining you again, on track and in life!

Merci Angers!

Parecendo que não, já passaram uns dois anos no LIBPhys. Gostaria de começar por agradecer a todos que me receberam tão bem desde o primeiro dia de estágio: o mítico estágio em que arrumei parafusos e, do qual não me arrependo absolutamente nada. Ao Professor Correia, por todos os conselhos, e pelo facto de ter sido responsável pelo ínicio desta aventura no GEI, deixo o meu obrigado muito especial!

Mencionar este projeto é sem dúvida mencionar o excelente trabalho da orientação do Professor João Cardoso . Foi incrível como "batalhou" para que o meu estágio em França se tornasse possível e como decidiu embarcar nesta aventura comigo. Agradeço por toda a disponibilidade e todo o trabalho de forma a poder terminar esta etapa! Toda a colaboração entre o Professor João e a Professora Anne foram sem dúvida fulcrais para que este projeto acontecesse e culminasse neste documento. Agradeço bastante aos dois por esse trabalho fantástico. Além deles, devo agradecer também bastante ao Pedro Vaz por toda a paciência, por todas as conversas e discussão de ideias ao longo deste percurso, que foram sem dúvida fundamentais para que o projeto se tornasse no que é hoje!

Quero ainda agradecer ao Tiago Marçal pela disponibilidade desde o ínicio, tanto nos estágios como posteriormente no projeto de tese, ao Miguel Correia por todos os bons momentos passados, ao Miguel Silva por todas as vezes que disse "Cansas-me a beleza!", "Gostei deste bocadinho" ou "Cafézinho?", à Sara Anjo por toda a ajuda e momentos que partilhamos e, claro, à Filipa Fernandes pela partilha de secretária e deveras aventuras!

Quero desejar boa sorte à Mariana Oliveira e à Daniela Amaral e, agradecer por partilharem comigo este último ano de curso, que foi com certeza mais especial por

causa de vocês! Foi comprido, demorou, mas conseguimos!

Aos meus restantes amigos, Maria, Lúcia, Ana, Oshley, Margarida, Sampaio e Abençoada: obrigada por partilharem comigo todas as recordações que levo comigo. Partilhámos etapas, aventuras, momentos de alegria e de frustração e, por isso, agradeço-vos bastante! Claro que também estás incluída aqui Daniela!

À minha melhor amiga, Joana Simões, que me viu crescer e que me conhece tão bem, obrigada! Sempre foste fantástica comigo,tendo partilhado já tantos momentos juntas. Espero ter o previlégio de continuar a partilhar muitos mais nesta nova fase da minha vida!

Às minhas equipas, Nexgym e Rocket Dolls, tanto treinadores como pessoas que aqui conheci, fizeram de alguma forma parte da minha vida e, estiveram presentes em momentos inesquecíveis. Bruno sou a atleta e pessoa que sou muito por causa de ti! Obrigada!

Vitor, obrigada pela compreensão, pela paciência para me aturar e o resto já sabes! Obrigada por me teres apoiado em tudo! Quero também agradecer à família Teixeira por me apoiarem nos meus objetivos desde que me conheceram.

Finalmente, às pessoas mais importantes de sempre, quero agradecer a toda a minha família! Aos primos, aos tios, aos avós e obviamente, aos meus pais e à minha irmã! Foi esta pequena, grande família, que me moldou, que me levou a ser a pessoa que sou hoje e a querer conquistar os meus objetivos! São poucas as palavras para poder agradecer aos meus pais e à minha irmã que fizeram sempre parte da minha vida. Foi toda uma jornada que culminou neste ponto e na qual toda a família colaborou de uma maneira ou de outra para que eu chegasse aqui! Tenho um bocadinho de todos comigo e sou mais feliz por isso!

Obrigada Coimbra!

# Resumo

Atualmente, os sinais e imagens biomédicas são fundamentais para o diagnóstico clínico. No entanto, em alguns casos, para um clínico menos experiente a sua interpretação poderá ser uma tarefa bastante difícil. Para algumas doenças, até médicos com vasta experiência podem demonstrar dificuldades em quantificar e identificar os vários estádios da doença em questão devido à sua natureza.

Desde os anos 1990' e, de acordo com a teoria da informação, surgiram várias medidas de entropia com o intuito de estudar a complexidade de sinais e imagens biomédicas. Além disso, a análise de múltiplos fatores de escala foi introduzida com o intuito de permitir uma visão detalhada dos dados em questão. Um valor de entropia elevado num sinal, imagem, ou volume revela uma elevada irregularidade do mesmo. Até agora, foram efetuados poucos avanços científicos no âmbito das medidas de entropia para a análise de volumes.

Baseado no conceito de entropia difusa ("*fuzzy entropy*"), foram propostos três novos algoritmos de medidas de entropia, todos revelando inovações. Antes da sua aplicação em dados biomédicos, estes foram testados e validados em dados sintéticos, de acordo com os métodos na literatura.

Em primeiro lugar, foi desenvolvida uma definição alternativa de de entropia difusa unidimensional ($FuzEn_{1D}$) bem como a sua versão multi-escala ($MFE_{1D}$), por forma a analisar a complexidade de sinais áudio de roncos bem como os estádios associados de síndrome de apneia-hipopneia do sono (SAHS). Este método revelou ser uma ferramenta interessante, que uma vez aperfeiçoado, poderá vir a ser utilizado no futuro para mais estudos.

Posteriormente, com o intuito de processar imagens dermoscópicas, foi introduzida a entropia difusa bidimensional colorida ($FuzEn_{C2D}$) para conduzir um estudo de microcirculação sanguínea e, um estudo para identificação de lesões de pele. Conseguiu-se provar que $FuzEn_{C2D}$ poderá ser de grande interesse para ambos os estudos. No caso do estudo de microcirculação sanguínea, demonstrou-se que existem diferenças estatísticas entre uma região da pele em repouso e, uma região vasodilatada do mesmo tamanho e no mesmo indivíduo. Adicionalmente, provou-se que são verificadas diferenças estatísticas entre as demais lesões da pele consideradas no estudo (*nevos comuns*, *nevos atípicos* e, *melanoma*).

Finalmente, é proposta ainda a entropia difusa tridimensional ($FuzEn_{3D}$) e a sua versão multi-escala ($MFE_{3D}$), para avaliar conjuntos de scans CT como um só volume de modo a proceder à identificação e ao estudo da progressão da doença Fibrose Pulmonar Idiopática (IPF). Neste último estudo, foi possível identificar a existência desta doença extremamente mortal entre dois grupos diferentes (um grupo de indivíduos saudáveis e, um grupo de indivíduos que sofrem de IPF).

**Palavras-chave:** *teoria da informação, medida de entropia, irregularidade, análise multi-escala, dados multidimensionais*

# Abstract

Nowadays, biomedical signals and images are of utmost importance for medical diagnosis. Nevertheless, in some cases, for a less experienced doctor, their interpretation can become a very hard task. For some diseases, even experienced doctors can have difficulties in quantifying and identifying several stages due to the disease's nature.

Since the 1990s, based on information theory, several entropy measures emerged to study biomedical signals and images' complexity. Moreover, multiple scale analysis has been introduced to have a more detailed view of the studied data. A high entropy value on a signal, image or volume reveals a high irregularity level. So far, little scientific advances have been made in analyzing volumes with entropy measures.

Based on fuzzy entropy, we propose three new entropy algorithms measures, all with innovations in the field. Before applying them to biomedical data, all of them were tested and validated on synthetic data, according to previous literature approaches.

First, an alternative unidimensional fuzzy entropy ($FuzEn_{1D}$) definition and the multiscale version ($MFE_{1D}$) has been developed to analyze snoring audio signals' complexity and Sleep Apnea-Hypoapnea Syndrome (SAHS) stages. This method revealed to be an interesting tool, that with some improvements, might be used in the future for further studies.

Moreover, to process dermoscopic images a bidimensional colored fuzzy entropy ($FuzEn_{C2D}$) algorithm was introduced to perform a cutaneous microcirculation study and the identification of skin lesions. It has been proven that $FuzEn_{C2D}$ can be of great interest to both microcirculatory assessment and melanoma identification. For the microcirculation study, statistical differences have been found between a relaxed skin region and vasodilated one of the same sizes for the same individual. Additionally, statistical differences have also been verified between the skin lesions considered (*common nevi*, *atypical nevi*, and *melanoma*).

Finally, a tridimensional fuzzy entropy ($FuzEn_{3D}$) and its multiscale version ($MFE_{3D}$) is proposed to evaluate sets of CT scans as volumetric data for identification of idiopathic pulmonary fibrosis (IPF) and stage progression. In this study, the existence of this deathly disease between two different groups (a group of healthy subjects and one group of subjects diagnosed with IPF) was identified.

**Key-Words:** *information theory, entropy measure, irregularity, multiscale analysis, multidimensional data*

# Contents

# List of abbreviations

| | |
|---|---|
| AHI | **A**pnea-**H**ypopnea **I**ndex |
| $\text{ApEn}_{1D}$ | **Ap**proximate **En**tropy for **1 D**imensional data |
| $\text{ApEn}_{2D}$ | **Ap**proximate **En**tropy for **2 D**imensional data |
| $\text{ApEn}_{3D}$ | **Ap**proximate **En**tropy for **3 D**imensional data |
| CAD | **C**omputer **A**ided **D**esign |
| CB | **C**olored **B**rodatz |
| CDK2NA | **C**yclin-**D**ependent **K**inase **I**nhibitor **2A** |
| $\text{CMSE}_{1D}$ | **C**omposite **M**ultiscale **S**ample **E**ntropy for **1 D**imensional data |
| CT | **C**omputerized **T**omography |
| $\text{DispEn}_{2D}$ | **Disp**ersion **En**tropy for **2 D**imensional data |
| $\text{DistrEn}_{2D}$ | **D**istribution **En**tropy for **2 D**imensional data |
| ECG | **E**lectro**c**ardio**g**ram |
| ECM | **E**xtra**c**ellular **M**atrix |
| EEG | **E**lectro**e**ncephalo**g**ram |
| ELM | **E**pi**l**uminescence **M**icroscopy |
| EMG | **E**lectro**m**yo**g**raphy |
| EOG | **E**lectro**o**culo**g**ram |
| ePDF | **e**mpirical **P**robability **D**ensity **F**unction |
| $\text{FuzEn}_{1D}$ | **Fuz**zy **En**tropy for **1 D**imensional data |
| $\text{FuzEn}_{2D}$ | **Fuz**zy **En**tropy for **2 D**imensional data |
| $\text{FuzEn}_{3D}$ | **Fuz**zy **En**tropy for **3 D**imensional data |
| $\text{FuzEn}_{C2D}$ | **Fuz**zy **En**tropy for **C**olored **2 D**imensional Data |
| $\text{FuzzyEn}_{1D}$ | **Fuzzy En**tropy for **1 D**imensional data (original definition) |
| HRCT | **H**igh-**R**esolution **C**omputerized **T**omography |
| i.i.d. | **i**ndependent **i**dentically **d**istributed |
| ILD | **I**nterstitial **L**ung **D**isease |
| IPF | **I**diopathic **P**ulmonary **F**ibrosis disease |
| LDF | **L**aser **D**oppler **F**lowmetry |
| LDI | **L**aser **D**oppler **I**maging |
| LSCI | **L**aser **S**peckle **C**ontrast **I**maging |
| $\text{MIX}_{1D}(p)$ | **MIX($p$)** processes for **1 D**imensional data |

| | |
|---|---|
| $\text{MIX}_{2D}(p)$ | **MIX($p$)** processes for **2 D**imensional data |
| $\text{MIX}_{3D}(p)$ | **MIX($p$)** processes for **3 D**imensional data |
| MEG | **M**agneto**e**ncephalo**g**ram |
| $\text{MFE}_{1D}$ | **M**ultiscale **F**uzzy **E**ntropy for **1 D**imensional data |
| $\text{MFE}_{3D}$ | **M**ultiscale **F**uzzy **E**ntropy for **3 D**imensional data |
| $\text{ModMSE}_{1D}$ | **Mod**ified **M**ultiscale **S**ample **E**ntropy for **1 D**imensional data |
| $\text{ModMSE}_{2D}$ | **M**ultiscale **Mod**ified **S**ample **E**ntropy **2 D**imensional |
| $\text{MSE}_{1D\sigma^2}$ | **M**ultiscale **S**ample **E**ntropy for **1 D**imensional data based on variance ($\sigma^2$) |
| $\text{MSE}_{1D}$ | **M**ultiscale **S**ample **E**ntropy for **1 D**imensional data |
| $\text{MSE}_{2D}$ | **M**ultiscale **S**ample **E**ntropy **2 D**imensional |
| | |
| OA | **O**ral **A**ppliances |
| OSA | **O**bstructive **S**leep **A**pnea |
| OSAHS | **O**bstructive **S**leep **A**pnea-**H**ypopnea **S**yndrome |
| | |
| $\text{PerEn}_{1D}$ | **Per**mutation **En**tropy for **1 D**imensional data |
| $\text{PerEn}_{2D}$ | **Per**mutation **En**tropy for **2 D**imensional data |
| PF | **P**ulmonary **F**ibrosis disease |
| PSD | **P**ower **S**pectral **D**ensity |
| PSG | **P**oly**s**omna**g**raphy |
| PTEN | **P**hosphatase and **Ten**sin Homologue |
| PXE | **P**seudo**x**anthoma **E**lasticum |
| | |
| $\text{RCMFE}_{1D}$ | **R**efined **C**omposite **M**ultiscale **F**uzzy **E**ntropy for **1 D**imensional data |
| $\text{RCMFE}_{1D\sigma}$ | **R**efined **C**omposite **M**ultiscale **F**uzzy **E**ntropy for **1 D**imensional data based on standard deviation ($\sigma$) |
| $\text{RCMSE}_{1D}$ | **R**efined **C**omposite **M**ultiscale **S**ample **E**ntropy for **1 D**imensional data |
| RDI | **R**espiratory **D**isturbance **I**ndex |
| RERAs | **R**espiratory **E**ffort **R**elated **A**rousal**s** |
| ROI | **R**egion **O**f **I**nterest |
| | |
| SAHS | **S**leep **A**pnea-**H**ypopnea **S**yndrome |
| $\text{SampEn}_{1D}$ | **Samp**le **En**tropy for **1 D**imensional data |
| $\text{SampEn}_{2D}$ | **Samp**le **En**tropy for **2 D**imensional data |
| $\text{SampEn}_{MF}$ | **M**ultidimensional and **F**uzzy **Samp**le **En**tropy |
| SD | **S**tandard **D**eviation |
| SE | **S**hannon's **E**ntropy |
| SRS | **S**nore **R**elated **S**ignals |

UIP **U**sual **I**nterstitial **P**neumonia

WHO **W**orld **H**ealth **O**rganisation

# List of Figures

# List of Tables

# 1 Introduction

This chapter content reveals the main goals of this project and the motivations behind it. Afterwards, the context of the project and the main topics regarding the biological applications proposed in this work are discussed. Besides, the chapter includes the project framework, calendar, the team involved, and the scientific contribution. Finally, the thesis document structure will presented to the reader.

## 1.1 Goals and motivations

Nowadays, medical specialists look for the best resources and tools to make a correct diagnosis based on valuable information. According to this, assisted medical diagnosis by new technological tools has been developed throughout the years in several medical fields. Many studies using entropy measure algorithms have been proposed to reveal important information about biomedical signals. Those algorithms can be used for the detection of a certain disease, including its characterization and if possible identification of its stage. The applications can be many, either based on unidimensional data or multidimensional data.

Based on bioinformatic knowledge and signal processing, and according to information theory, entropy measures have been developed. They can help in classifying the presence/absence of the approached diseases, having in consideration the importance of also quantifying the disease.

Entropy measures can offer detailed information on a biomedical signal or image, helping the physician to make a decision based on both medical experience and computer-based assistance. For young doctors, it can be even more essential because it might prevent false diagnosis or missed ones.

## 1.2 Context

This dissertation has been developed during the last year of the *Integrated Master of Biomedical Engineering* program of the University of Coimbra, Portugal, to obtain the Master's degree.

This project involved an inter university collaboration of two teams: *Laboratório de Instrumentação, Engenharia Biomédica e Física da Radiação - UC* (LIBPhys-UC), University of Coimbra, Portugal and *Laboratoire Angevin de Recherche en Ingénierie des Systèmes* (LARIS), University of Angers, France.

In coordination with the LARIS, the work involved one-dimensional and multidimensional fuzzy entropy measures. The initial goal was to validate the developed algorithms to be *a posterior* applied to biomedical data. Taking into account the biomedical applications of this project, the next task involved the detection of some diseases.

Snoring audio signals have been used to study sleep apnea-hypopnea syndrome, as the application of the proposed unidimensional algorithm. These signals were previously collected for the PhD project of a LIBPhys-UC member, MSc *Tiago Marçal*.

During an ERASMUS+ internship, the multidimensional algorithms have been developed and tested on synthetic signals. A report containing some notes regarding the tests performed during that time and some conclusions is presented in appendix C.

Regarding the multidimensional data, dermoscopic images and high-resolution CT scans have been provided in collaboration with the *University Hospital of Angers*, France, and *University Hospital of Rennes*, France, respectively. Additionally, a public database containing several dermoscopic images on skin lesions has been tested.

## 1.3 Biomedical applications

Herein, the biomedical applications of this project for both uni-, bi-, and tridimensional entropy measures are presented.

### 1.3.1 Snoring and sleep apnea-hypopnea syndrome

Snoring is a prevalent disorder among $20 - 40\%$ of general population [1] and is one of the earliest and most consistent symptoms of *Sleep Apnea-Hypopnea syndrome* (SAHS) [2, 3].

The snore results from the vibration in pharyngeal airway. Young *et al.* [4] conducted a study on 4925 adults between 30 and 60 years old, concluding that at least 80% of all moderate to severe cases of SAHS are most likely missed.

SAHS is characterized by several breath cessations. Snoring can be present in the inhalation or trough the entire breathing cycle [2, 5].

Both snoring and *obstructive sleep apnea-hypoapnea syndrome* (OSAHS) can consequently be associated with the existence of other diseases like heart related ones, metabolic dysfunction, neurocognitive dysfunction and also, increased mortality [3, 6].

Respiratory sounds can be classified using the *Apnea-Hypopnea Index* (AHI) or *respiratory disturbance index* (RDI) to reveal how severe are the snores. AHI corresponds to the number of apneas and hypopneas per hour of sleep [2, 5, 7] and RDI can be defined as the total number of apneas, hypoapneas and *respiratory effort related arousals* (RERAs) per hour [7] .

OSAHS is present when AHI is superior to 5 apneas and hypopneas per hour of sleep. Otherwise, if both apneas or hypopneas are not registered during the sleep time of the subject, it is stated that only *simple snoring* is present [2].

Besides clinical information and symptoms, information from *polysomnography* (PSG) must be analyzed by the medical doctor [3, 6, 7]. To treat the syndrome *oral appliances* (OA) have been increasingly used [3, 6]. An additional PSG study or an attended cardio-respiratory sleep study can be used to ensure that the treatment is working [6].

### 1.3.2 Melanoma

Melanoma is the deadliest skin cancer, with an increasing incidence [8]. According to Bray *et al.* [9], melanoma represents 1.6% of all new cases of cancer world wide, and 0.6% global deaths by cancer, affecting mainly exposed skin regions like face, neck, arms and legs [10]. When detected early, medical doctors are able to increase the survival rate over 90% [11].

The European guideline for diagnosis and melanoma treatment [12] states that melanoma can be defined as a malignant type of tumor, arousing from melanocytic cells with location primarily in the skin [12]. Besides the high death rates, melanoma holds a very high potential to metastasize even for small sized tumors [12].

The associated risk factors are family history, multiple benign lesions, atypical nevi presence, previous melanoma, immunosuppression, sun skin sensitivity and exposure to ultra-violet radiation [13].

Melanomas evolve in size, shape and color [14]. The colors black, red, white and blue-gray are more frequent in these lesions than in non-malignant ones [15].

Currently, the best treatment is still early diagnosis and surgical excision [16]. Dermoscopy is the technique used by specialists to aid in skin lesions diagnosis [8, 16]. The first consensus Net meeting on Dermoscopy took place in Rome, 2001 [16].

Early detection can reduce the unnecessary and painful biopsies as well raise the probability of preventing metastatic lesions [10].

### 1.3.3 Microcirculatory assessment

Microcirculation system participates in nutrient's exchange and oxygenation [17, 18]. To guarantee *hemodynamic coherence* microcirculation should be monitored [19]. Moreover, several pathologies need vascular assessment namely cardiovascular diseases, diabetes and hypertension [18].

When resuscitation techniques are applied, if they only normalized the systemic values but were not efficient in improving microcirculation and oxygenation this means there is a loss of hemodynamic coherence [19].

One can conclude that it is of great importance to measure microcirculatory activity. To evaluate microcirculation, morphological (ex: vessel density, rate of perfused vessels and vessel diameter, ...) and functional parameters (ex: pharmacological tests, post occlusive reactive hyperemia, ...) can be measured [17]. Imaging techniques can be used like video microscopy-based ones, *laser Doppler flowmetry* (LDF), *laser Doppler imaging* (LDI) and *laser Doppler contrast imaging* (LSCI) [17, 18].

With the need to improve and establish new medical diagnosis using signal processing tools that are safe, cheap and easy to use [18], like entropy measures, the goal was to assess if entropy measures can distinguish two different microvascular states.

### 1.3.4 Idiopathic pulmonary fibrosis

*Pulmonary Fibrosis* (PF) is a deathly disease, characterized by a "progressive and irreversible destruction of the lung architecture caused by scar formation" [20].

Idiopathic pulmonary fibrosis (IPF) is a very severe form of PF with a short life expectancy [20] of 3 years average mortality [21]. *Marshall* et al. [21] reported that both incidence and mortality rates are rising. IPF is the most common type of idiopathic interstitial pneumonia among the group [22].

Based on the WHO database, within Europe, United Kingdom, Finland and Portugal are the three countries with the highest death rates by that order and France represents the $8^{th}$ highest death rate country [21]. So far, the only effective treatment is lung transplantation [20]. IPF prevails mainly in elderly male subjects [21].

In order to determine the presence of a typical usual interstitial pneumonia (UIP) pattern, honeycombing characteristic must be present, usually associated with traction bronchiectasis, being localized essentially in the basal and peripheral region of the lungs [23–26].

Since the current medical drugs and treatments still do not have the ability to cure IPF [21], it would be interesting to develop a measure that determines the existence of this disease and, more importantly, that is able to quantify it. Quantification can be a great tool to monitor the drugs efficiency and disease evolution.

## 1.4 Project framework

Due to the large applicability of entropy measures, this project involved three different applications: snoring events and SAHS disease, skin dermoscopic images and CT scans to identify idiopathic pulmonary fibrosis (IPF). This was mainly based on previous paper works but also contains innovations namely the bi-dimensional algorithm being now applied in colored images and a new tri-dimensional approach in 3D datasets of images.

Regarding one of the applications of this project, an entropy measure has been applied on snore related signals. This dataset has been provided by MSc *Tiago Marçal*, (LIBPhys-UC, University of Coimbra, Portugal) and collected during his PhD program with the collaboration of Dr. *José Moutinho* from Centro de Medicina do Sono, CHUC. The main goal using this type of one-dimensional signals was to detect snoring events and possibly quantify the disease stage for different individuals.

Afterwards, in parallel with the previous work mentioned, during an internship at LARIS, University of Angers, France, this project involved the development and validation of two new multidimensional entropy measures.

The validation tests have been performed during an internship in LARIS, University of Angers, France. In addition, some initial tests with biomedical images have also been performed. The description of the work developed during the internship can be consulted in Appendix *C*.

These bi-dimensional and tri-dimensional measures have been developed in order to assess the irregularity patterns of colored dermoscopic images and volumetric CT scans, respectively. In the first case, the ultimate goal has been identifying microcirculatory states and differentiating skin lesions, having the collaboration of University Hospital of Angers, France, on the first application. On the other hand, the tri-dimensional measure has been developed having in mind the identification

of *Idiopathic Pulmonary Fibrosis*, a deathly lung's disease, in high-resolution CT scans, provided by the University Hospital of Rennes, France.

## 1.5 Calendar

The project developed applied entropy measures algorithms to assess irregularity of biomedical signals and assist in medical diagnosis of snoring related diseases, skin lesions and pulmonary fibrosis. Several tasks were performed these last months with the collaboration of two universities and are presented in figure 1.1.

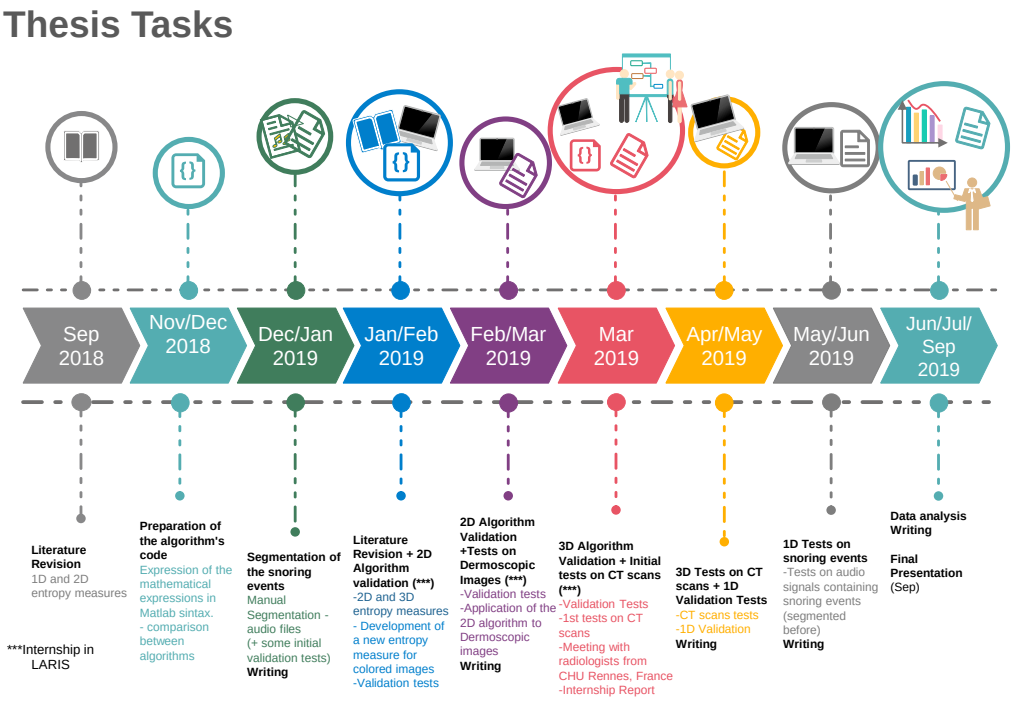


**Figure 1.1:** Thesis time line and the corresponding tasks performed during the project.

## 1.6 Team and partners

This project involved several partners during its development namely: LIBPhys-UC, Portugal, LARIS, France, University Hospital of Angers (CHU Angers), France and University Hospital of Rennes (CHU Rennes), France. The team members of this project are represented in table 1.1.

**Table 1.1:** Team members involved in the project.

| Team members | Function | Institution |
|---|---|---|
| PhD Professor João Cardoso | Supervisor | LIBPhys-UC |
| PhD Professor Anne Humeau-Heurtier | Supervisor | LARIS |
| PhD Pedro Vaz | Consultant/Junior Researcher | LIBPhys-UC |
| MSc Mirvana Hilal | Consultant/PhD student | LARIS |
| Dr. Clémence Martin | Dermatologist | CHU Angers |
| Dr. Ludovic Martin | Dermatologist | CHU Angers |
| Dr. Mathieu Lederlin | Radiologist | CHU Rennes |
| Dr. Guillaume Mahé | Vascular Medicine | CHU Rennes |
| MSc Miguel Silva | PhD student | LIBPhys-UC |
| MSc Tiago Marçal | PhD student | LIBPhys-UC |

## 1.7 Scientific contribution

In table 1.2, it is shown the scientific contribution of this project in an international conference paper, resulting from the collaboration of both investigation groups involved.

**Table 1.2:** Reference of scientific contribution.

| ***International conference proceeding paper*** | ***Ref.*** |
|---|---|
| Mirvana Hilal, Andreia Sofia F. Gaudêncio, Clémence Berthin, Pedro G. Vaz, João Cardoso, Ludovic Martin, and Anne Humeau-Heurtier. "Bidimensional Colored Fuzzy Entropy Measure: a Cutaneous Microcirculation Study". In: 5th International Conference on Advances in Biomedical Engineering (ICABME19), Lebanon. 2019 (accepted) | [75] |

## 1.8 Thesis structure

The thesis document is divided into 6 main chapters and appendices.

The following chapter, *State of the Art*, presents entropy measures and the biomedical applications in a more detailed view. Regarding biomedical applications, it is described snoring, skin lesions including melanoma development, microcirculation, and idiopathic pulmonary fibrosis.

In the chapter entitled *Materials*, the synthetic signals, images, and tridimensional data that has been used for validation are presented. In addition, the goals of using that data for the project are explained. Then, it is described the biomedical data used, revealing the goals of the biomedical tests performed. Audio signals of snoring, dermoscopic images and volumetric CT scans have been used to assess entropy and perform the final biomedical tests.

Thereupon, in chapter 4 entitled as *Methods*, the developed algorithms during the Master thesis project are discussed as well as the methodology used to obtain the final results.

Afterwards, a chapter is dedicated to the results. The final chapter, the *Conclusion*, mentions the main conclusions of this project, future work to develop and final remarks regarding the thesis.

Attached to this document, the *Appendices* are also shown.

# 2 State of the art

The current chapter will include some theoretical background regarding the biomedical applications of this thesis project. Moreover, it will also describe the existing entropy measure algorithms and their evolution in a more detailed view for one-dimensional and multidimensional data and their multiscale versions.

## 2.1 Theoretical background

### 2.1.1 Snoring and snore related signals

Snoring, a prevalent disorder among $20 - 40\%$ of the general population, results from the vibration in pharyngeal airway anatomical structures and can be influenced by several factors such as body position, presence of sleeping disorders, sleep stage, among others. Snoring and snore related signals (SRS) carries important information like the obstructed site of the airway [1, 2, 6].

Sleep Apnea-Hypopnea syndrome (SAHS), a sleep disorder, is characterized by several breath cessations, leading to hypoxemia and sleep disruption. One of the earliest and most consistent symptoms in SAHS is snoring [2, 3]. Snoring can occur during inhalation or be present during the entire respiratory cycle (inhalation and exhalation) [2, 5].

This biological process occurs due to an airway obstruction and is an heterogeneous acoustic phenomena, *i.e.*, there can be variations from night to night and even in the same night these variations can occur [2]. Obstructive sleep apnea-hypoapnea syndrome (OSAHS) is associated to upper airway obstruction due, for example, to obesity or cranio-facial abnormalities [3]. Due to increased resistance in the upper airway, the airflow becomes turbulent, producing vibrations in the pharyngeal tissues. In the end, when snoring, a subject has oscillations in several locations like the soft palate, pharyngeal walls, epiglottis, and tongue [2].

Snoring and OSAHS are, in most cases, associated with the existence of other diseases like cardiac ones and increased mortality [3, 6].

There are two different types of snores [5]:

**Regular:** Snores happening successively and during consecutive breathing cycles.

**Non-Regular:** Snores that are separated by non-breathing cycles and/or apneas.

An apnea can be defined as the absence of breathing for at least 10 seconds and an hypopnea is considered as a decreased breathing (not completely absent one) for at least 10 seconds [2]. Additional information like for example different types of apneas is included in table 2.1 based on information provided by Kushida *et al.* [7].

To classify the respiratory sounds there is an Apnea-Hypopnea Index (AHI), revealing the severeness of snores. AHI corresponds to the number of apneas and hypopneas per hour of sleep [2, 5, 7].

When AHI is superior to 5 and excessive daytime sleeping is verified, an obstructive sleep apnea (OSA) syndrome is present. Otherwise, the absence of apnea or hypopnea during sleep time means the existence of *simple snoring* [2].

**Table 2.1:** Breathing sleep events definitions. Adapted from [7].

| *Breathing Events* | *Definition* |
|---|---|
| **Obstructive Apnea** | **Clinical Def.:** Absence of airflow for at least 10 seconds. Considered obstructive if during the event there is difficulty in breathing.<br>**Research Def.:** A decrease of at least 50% from baseline in amplitude of a valid measure of breathing, for at least 10 seconds. |
| **Central Apnea** | **Clinical Def.:** Absence of airflow for at least 10 seconds (apnea) without difficulty in breathing.<br>**Research Def.:** Same definition as the obstructive but the lack of breathing difficulty must be verified with an esophageal balloon. |
| **Mixed Apnea** | **Clinical Def.:** Absence of airflow for at least 10 seconds, starting as a central apnea.Presence of an effort in breathing at the end. |
| **Hypopnea** | **Clinical Def.:** Abnormal respiratory event with a reduction of thoracoabdominal movement (or airflow) of at least 30 % compared to the baseline, during 10 at least 10 seconds. An oxygen desaturation higher than 4% must be verified.<br>**Research Def.:** Clear amplitude decrease (less than 50%) of breathing validated measure during sleep. Oxygen desaturation is higher than 3% or arousal. Use of esophageal balloon to confirm central or obstructive hypopnea. |
| **Respiratory-Effort Related Arousal (RERA)** | **Clinical Def.:** No agreement.<br>**Research Def.:** A sequence of breaths showing an increased difficulty in breathing. Associated with higher negative esophageal pressure for at least 10 seconds. |

Besides the previous index, the respiratory disturbance index (RDI) can be defined as the total number of apneas, hypoapneas and respiratory effort related arousals (RERAs) per hour [7]. Nevertheless, sometimes it is used synonymously with AHI [7]. The severity criteria based on sleep related obstruction breathing events is represented in table 2.2.

**Table 2.2:** Severity criteria according to the number of obstructive sleep breathing events per hour. Adapted from [3].

| **Severity Criteria** | **Sleep related obstruction breathing events per hour** |
|---|---|
| Snoring | $< 5$ |
| Mild/Light | $5 - 15$ |
| Moderate | $15 - 30$ |
| Severe | $> 30$ |

For the diagnosis of apnea disease details like clinical information, symptoms and polysomnography (PSG) findings must be included [3, 6, 7]. Kushida *et al.* [6] suggests that the standard process of determining the correct treatment must include "the severity of sleep related respiratory problems". Nowadays, oral appliances (OA) are being used as treatment for OSA increasingly [3, 6] and, to insure the medicine is working, the patients should undergo polysomnography or an attended cardio-respiratory sleep study [6]. This study can be very expensive and time-consuming since multiple biosignals are recorded [5].

For an attended PSG setting, where an overnight study is performed, the standard recording montage includes the following multichannel monitoring [3]:

- Electroencephalogram (EEG)
- Electrooculogram (EOG)
- Chin Electromyography (EMG)

- Electrocardiogram (ECG)
- Airflow
- Respiratory effort
- $SpO_2$ (by oximeter)
- Anterior tibialis EMG

An analysis based on snoring acoustics can have a better potential to differentiate individuals with 'simple snoring' from OSAHS suffering individual [1].

As Mesquita *et al.* [5] mention, there is a current need of simplifying the diagnosis method namely, the process of PSG, since it requires monitoring several biosignals. This can imply reducing the number of signals screened or even analyze only one like breath and snore sounds.

As an heterogeneous and turbulent phenomena, snoring has a variable range of sound spectrum. Moreover, there is also the need of quantifying objectively snoring [2]. Having that in mind, the project of this thesis included a study of snoring sounds. The audio signals containing snoring events, i.e., snoring related signals have been studied with the proposed entropy measurement algorithm with the goal of revealing the intrinsic irregularity of this biological event.

### 2.1.2 Dermoscopy study: melanoma and microcirculation assessment

#### 2.1.2.1 Melanoma

Melanoma is a malignant type of tumor, arousing from melanocytic cells with location primarily in the skin [12]. It is also the deadliest skin cancer, with an increasing incidence [8]. If detected early the survival rate can be increased over 90% [11]. The main risk factors are family history, multiple benign lesions or atypical nevi and previous melanomas [13]. Additionally, immunosuppression, sun sensitivity and exposure to UV light can represent a higher risk of developing melanoma [13].

Melanomas usually present asymmetry, irregular borders, uneven color distributions and a diameter wider than 6 $mm$ evolving therefore, in size, shape and color [14]. Usually, malignant lesions are associated with more than three different colors [15] and the best treatment is early diagnosis and surgical excision [16].

Figure 2.1 shows melanoma progression from normal melanocytes to malignant lesion according to the Clark model [13]. The stage one is characterized by the development of benign nevi, composed by neval melanocytes. Although these cells growth is uncontrolled, the nevus growth is limited. When the dysplastic nevi is present, the existent abnormalities will affect cell growth, DNA repair and susceptibility to cell death [13].

The gene CDK2NA (cyclin-dependent kinase inhibitor 2A) is inactive in $25-40\%$ of familial melanoma cases due to genetic defect. This gene is responsible for encoding two tumor suppressor proteins (p16 and p19). On the other hand, for

non-familial cases, PTEN gene (Phosphatase and Tensin Homologue), also a tumor suppressor, is inactivated due to genetic mutations [13].

In radial-growth phase, a decreased differentiation is observed as well as unlimited hyperplasia. Upcoming, in the vertical-growth stage, cells cross the basal membrane and form the tumor. Finally, in a metastatic stage, the cancer can spread to the lungs, liver or even to the brain [13].

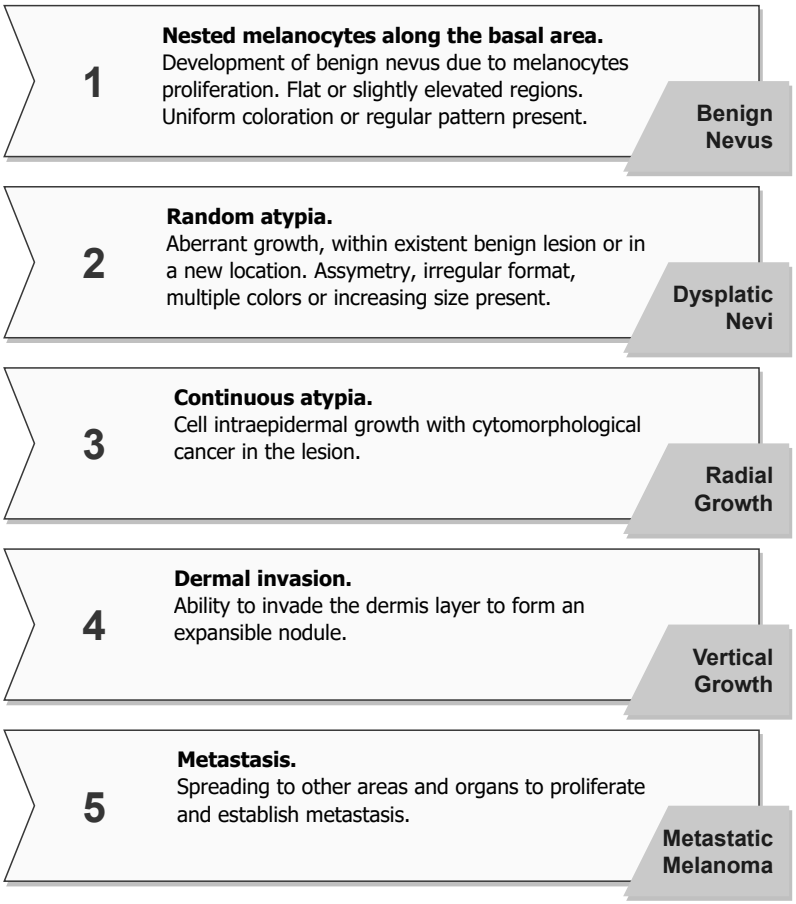


**Figure 2.1:** Clark model explaining the progression model of melanoma, based on Miller and Mihm [13] representation.

According to Garbe *et al.* [12], the melanoma can be identified, clinically and histologically, in four subtypes and other rare forms (see table 2.3).

Melanoma's death is associated with increased number of *nevi* in patients [27]. Small pigmented skin lesions are still difficult to distinguish between non-melanoma and melanoma [28]. Typical common moles (pigmented lesions), i.e., *common nevi* are clinically and histologically different from atypical moles, i.e., *atypical nevi* [1] [29]. Atypical nevi can have different sizes but are usually larger than common nevi.

Initially, the diagnosis depended only on medical doctor's visual inspection of lesions [8, 14, 16, 30, 31]. This unaided procedure lacked in accuracy [8, 16, 30] and identifying early stages of the disease was a difficult task, leading to unnecessary

[1] In 1992, it was given the recommendation by NHI Consensus Conference to abandon the term *dysplastic nevus*.

**Table 2.3:** Melanoma subtypes according to the European guideline for Melanoma diagnosis and treatment [12].

| Melanoma subtype | Main features and characteristics |
|---|---|
| ***Superficial spreading melanoma*** | Starts with an intraepidermal growth (horizontal or radial) and evolves to a plaque shape. Malignant melanocytes spread throughout the epidermis. Presents multiple colors and pale areas of regression. |
| ***Nodular melanoma*** | Mainly nodular with brown-black color, often eroded or bleeding tumor. It presents a vertical aggressive growth phase (little or no horizontal growth phase). Early identification is almost impossible. |
| ***Lentigo maligna melanoma*** | Located predominantly on sun damaged areas of elder people. Lentiginous proliferation of atypical melanocytes. |
| ***Acral lentiginous melanoma*** | Tipically, palmoplantar and subungual. Irregular pigmentation is present. Nodular region can be visible due to invasive growth. |
| **Rare forms**: desmoplastic, amenalotic and polypoid melanomas (less than 5% of the cases). | |

biopsies [8].

In 1663, skin surface microscopy was used to study small vessels and later on, this technique started to use immersion oil and glass spatulas [16]. Already in the $20^{th}$ century, Saphier [32] introduced the term "*Dermatoscopy*". Further on, to evaluate pigmented skin lesions for the first time Goldman [33] introduced "*Dermoscopy*".

Nowadays, the trained specialists use dermoscopic images to assist skin lesions diagnosis. Dermoscopy or Epiluminescence Microscopy [2] (ELM) is a high-resolution, *in vivo* method and non invasive technique. It allows the visualization of deeper skin structures with improved accuracy compared to clinical visual inspection [8, 14–16]. Hence, dermoscopy allows to look into the visual and morphological characterization of skin pigmented lesions [30].

If this technique is not performed by trained dermatologists there can be limitations in the accuracy levels [8, 12, 30]. Even for the specialists, diagnosis remains subjective [8, 30] and with an estimated accuracy of 70% [12].

This field still have space to improve in aided diagnosis since there is a need for an automated system to differentiate melanoma, non-melanoma, and benign skin lesions [14].

Follow-up of skin lesions with dermoscopy can be also a major task to identify early melanoma. Both early detection and treatment are very important for a good prognosis of patients showing primary cutaneous melanoma [28].

One common task involving dermoscopy is color identification [15, 31]. However, this can be subjective, representing a huge challenge on the field [34].

Some studies focus on CAD systems to detect automatically melanoma. These studies require defining a region of interest (ROI) for the melanoma classification [10]. Segmentation can be difficult due to the different melanoma's characteristics like shape, size and color. Moreover, hair and small vessels can interfere both in melanoma detection and segmentation [10].

[2]Also known as Dermatoscopy and Amplified Surface Microscopy [16]

The goal of using entropy techniques is to reveal new information about the dermoscopic images and hopefully, in the future, aid in the diagnosis of skin lesions and cancer, improving the accuracy of diagnosis.

#### 2.1.2.2 Microcirculatory assessment

The microcirculatory system is defined by small arteries (also resistance arteries and with diameter less than $< 150\ \mu m$), capillaries, arterioles and venules [17]. It is involved in nutrient's supply as well as oxygenation [17, 18]. Monitoring microcirculation can be of great importance to determine for example, *hemodynamic coherence* after resuscitation procedures being applied [19]. On the other hand, several pathologies need vascular assessment like cardiovascular diseases, diabetes, hypertension, foot ulcers, atherosclerosis, among others [18].

One can conclude that it is of great importance to quantify the microvascular activity. To evaluate microcirculation, morphological (ex: vessel density, rate of perfused vessels and vessel diameter, ...) and functional parameters (ex: pharmacological tests, post occlusive reactive hyperemia, ...) can be measured [17]. Imaging techniques can be used like video microscopy based ones, laser Doppler flowmetry (LDF), laser Doppler imaging (LDI) and laser Doppler contrast imaging (LSCI) [17, 18].

Video microscopy allows direct visualization. However, pressure artifacts are associated [17]. LDF and LDI are techniques that provide interesting information but with a difficult usage in some particular clinical situations [18]. LSCI overcomes some of the previous techniques disadvantages [18].

Humeau-Heurtier *et al.* [18] pointed out two important aspects: to improve and establish new medical diagnosis, signal processing tools following safety requirements, that are cheap and easy to use, can be a future option; the second aspect is that determining values for microvascular tests is a demand.

According to this, entropy measures can be image processing tools of great interest in the future to determine and quantify microcirculation states. The goal of the project was to use entropy measures to differentiate dermoscopic images for subjects at rest and after applying heat to their skin, i.e., differentiating regular microcirculatory states and vasodilated microcirculations, respectively.

### 2.1.3 Idiopathic pulmonary fibrosis

Pulmonary Fibrosis (PF) is a deathly disease, with the only effective treatment being the lung transplantation [20]. This disease is characterized by a "progressive and irreversible destruction of the lung architecture caused by scar formation" [20].

Idiopathic pulmonary fibrosis (IPF) is a chronic, progressive, specific type of PF, defined by the patterns existence of usual interstitial pneumonia (UIP) [23–26]. This very severe disease of unknown cause [24, 25] has a short life expectancy [20] of 3 years average mortality [21]. Therefore, an early diagnosis is imperative as well as an assessment of the disease stage. Recently, new antifibrotic agents have been developed, slowing down the disease progression. However, these medicines are not a cure and have poor outcomes [21].

IPF has an incidence mainly in male subjects, with advancing age [21, 24, 25] and smoking history [24, 25]. The potential risk factors are smoking habits, gastroesophageal reflux, chronic viral infections, hepatitis C and family history of other interstitial lung disease (ILD) [24, 25]. Marshall *et al.* [21] reported that both incidence and mortality rates are rising.

Pires *et al.* [22] verified, among their patients, a reduced lung diffusion and exercise capacity impairment.

Diagnosing IPF must fulfill the following three requirements [24, 25]:

1. Exclude other known ILD causes like environmental exposures (metal dusts, wood dust, farming, drug toxicity, ...);

2. Identification of UIP pattern on high-resolution computerized tomography (HRCT) scans;

3. Specific combinations of HRCT and histological patterns in patients that were subjected to lung's biopsy.

The fibrotic scar can be developed after a wound healing response getting out of control, leading to extracellular matrix (ECM) components accumulation at the injury site [20]. Such components can be hyaluronic acid, fibronectin, proteoglycans, collagen, among others [20].

There are four main stages regarding the wound healing repair process and they are [20, 21]:

1. Coagulation

2. Migration of inflammatory cells

3. Migration, proliferation and activation of fibroblasts

4. Tissue remodeling

If instead of having wound repair as expected, a deregulation of one of those stages, wound severeness or, persistent damaged tissue is observed, consequently, fibrosis is being developed [20, 21].

Once there is damaged tissue, an anti-fibronolytic coagulation cascade is initiated, caused by the release of inflammatory mediators from epithelial and/or endothelial cells and triggering clotting as well as the development of provisional ECM (stage 1) [20].

As a consequence of platelet aggregation and degranulation, vasodilation occurs and increased permeability is verified, allowing recruitment of inflammatory cells like neutrophils, macrophages, lymphocytes and eosinophils (stage 2) [20].

Firstly, neutrophils are the most abundant cells in wound repair early stages, being shortly after substituted by macrophages once the neutrophil's degranulation occurs. Any invading organisms are eliminated by both activated macrophages and neutrophils (stage 2). Afterwards, these cells produce cytokines and chemokines that will not only amplify this inflammatory response but also trigger proliferation and recruitment of fibroblasts. The activated fibroblasts transform themselves into

myofibroblasts capable of secreting ECM components. During the wound remodeling phase, in a completely normal process, wound contraction is promoted by these myofibroblasts. Otherwise, fibrosis is developed contributing to the excess of ECM deposition [20].

Many stages of the wound repair process can go wrong, which can explain the complex nature of PF [20].

Since the active inflammatory response is not a prerequisite, the most common therapies, like anti-inflammatory ones, have shown little effect on the idiopathic form of this disease. This explains the absence of detectable inflammation signs like other types of the disease [20].

In the case of IPF, the possible explanation for fibrosis progression is intrinsic defects in the wound healing response IPF.

To diagnose IPF, HRCT are taken from the patient's chest region through volumetric scanning [23–25]. According to the most recent guideline of Raghu *et al.* [25], the scanning protocol should follow the following technical requirements:

- Non-contrast acquisition;
- Thinnest collimation, shortest rotation time and highest pitch to guarantee motion-free images;
- Both potential and current of the tube must be appropriate to the patient's size (usually 120 kVp and $\leq 240$ mA) and avoid unnecessary radiation exposure.
- Thin ($\leq 1.5$ mm) CT sections (contiguous or overlapping reconstruction);
- 3 different acquisitions with the last being optional: supine - inspiratory (volumetric), supine - expiratory (volumetric or sequential) and prone - inspiratory (sequential or volumetric);
- The inspiratory volumetric acquisition should have a reduced radiation dose of $1 - 3$ mSv but, avoiding ultra-low CT doses.

As said before, the radiologist needs to identify a probable UIP pattern [23–26]. This can exclude the need of a surgical lung biopsy [23]. The pattern identified can be classified into one of four categories: typical UIP CT pattern, probable UIP CT pattern, CT pattern indeterminate for UIP, and CT features most consistent with non-IPF diagnosis [23].

*Honeycombing* is a key characteristic to identify the UIP pattern. This clustered and thick-wall cystic spaces have usually 3 to 5 mm [23–26]. Other markers of lung fibrosis are *traction bronchiectasis* and *bronchiolectasis*. These markers are important in the identification of UIP [23–26]. The first marker, is specially predominant in the peripheral area and presents an irregular appearance, reticulation, and ground glass opacity [23].

In order to determine the presence of a typical UIP pattern, honeycombing characteristic must be present, usually associated with traction bronchiectasis, being localized essentially in the basal and peripheral region of the lungs [23, 25, 26].

### 2.1.4 Evolution of entropy measures

Entropy can be seen as a "rate of information production" [35]. When applying entropy as a measure, the main goal must be to quantify the irregularity of a signal, translating the inherent complexity [35–37]. Based on statistics, entropy is a system's disorder translation [38].

If the entropy value is close to zero, this leads to the conclusion that this system is predictable regular [35–38]. On the other hand, as the signals get more complex (i.e. the irregularities increase) the entropy is higher [35–38]. Basically, a signal tend to have an higher entropy value, when both high variability and data's random nature is verified [39].

This measurement is both intuitive and independent of absolute scales. Visually, a signal can be recognized as periodic or not. It can even be compared with a second signal. One can say if it is more complex than the first one or very similar. In addition, the entropy is not influenced by the amplitude or frequency of the signal [38].

Allied to the power of entropy, the concept of image texture and its classification through entropy can be introduced. An image can have several types of tonal primitives with a certain spatial organization that will determine its texture. So, there will be some properties associated such as fineness, smoothness, granulations and obviously irregularity, among others [40].

## 2.2 Entropy measures and algorithms

Since 1990's, many entropy measures have been developed based on information theory [41]. Entropy algorithms can quantify a signal's regularity based on its entropy values. Entropy can be defined as "the rate of information production" [35].

As Tsallis [42] suggested, entropy deals with the probabilities associated to the systems' energies. Approximate entropy ($\mathrm{ApEn}_{1D}$) [36] emerged with the purpose of quantifying the regularity of a system. Richman and Moorman [35] compared then, approximate entropy with a new measure, sample entropy ($\mathrm{SampEn}_{1D}$), to apply to physiological signals.

Since then, many studies have emerged with different kind of applications namely in the cardiovascular area [35, 39, 43, 44], EMG signals [45, 46], genetic area [39], bearing vibration data [47, 48], image segmentation [49], among others.

Moreover, several applications involved multiscale versions of these entropy measures. Zhang [50] performed the first approach using multiscale in physical systems based on *Shannon*'s entropy [51] but only with the study of *Costa et al.* [39, 43], the coarse-graining procedure started to gain attention due to its applicability to biological systems.

Entropy assessment analysis revealed itself so promising for one dimensional signals that the logical upcoming analysis was to study images' complexity. Silva *et al.* [52] applied the concept of sample entropy to images, comparing patterns of the image itself and defining the presence or absence of similarity between them.

Since those advancements, some of these measures have been extended to bi-dimensional or tri-dimensional (or both) definitions [52–58]. Moreover, several alterations on the coarse-graining procedure have been published [47, 48, 59–61].

Herein, in section 2.2, the main already-existing entropy measures are mentioned and fuzzy entropy, on which the thesis work is based, is also explained . First, the entropy measures developed to be applied into unidimensional data through single scale analysis are discussed. Then, the multiscale algorithms for signals are also approached. Afterwards, entropy measure algorithms to apply on multidimensional data are approached and in case of existence, their multiscale versions are mentioned.

All the algorithms used in this dissertation, that allowed to obtain the shown results, in chapter 5, are in full detail, including the mathematical definitions, in chapter 4.

### 2.2.1 Entropy measures for one dimensional signals

Initially, entropy measures focused only on single scale's entropy value of the signal to analyze the system [35–38, 44–46, 52, 56].

Considering information theory [51] knowledge, many entropy measures have been developed like Shannon's entropy [38, 51, 62], approximate entropy [36], permutation entropy [63], sample entropy [35, 37], fuzzy entropy [44–46, 57, 60, 64], among others. These entropy measures can compare and classify the data as regular, chaotic or random [65].

Multiscale versions of these algorithms only started to appear later, involving a *coarse-graining* procedure with many applications namely, synthetic signals [39, 43, 47, 48, 59, 60, 66], ECG signals [39, 43, 59], bearing vibration signals [47, 48, 57], MEG signals [60] and EEG signals [60]. In the end, multiple values of entropy for the same signal are considered, quantifying entropy over several temporal scales [61].

#### 2.2.1.1 Single scale analysis

According to information theory, *Shannon*'s entropy (SE) [51] was defined and established as an intuitive parameter that is able to relate the amount of disorder in data [38]. SE measures an average uncertainty [67] and depends on a set of probabilities, $p_i$ (see equation (2.1)) [51].

$$SE = H(x) = -\sum p_i \log(p_i) \tag{2.1}$$

In the 1990's, approximate entropy ($\mathrm{ApEn}_{1D}$) [36], a process of entropy determination based on similarities within the studied signals. However, $\mathrm{ApEn}_{1D}$ presented inconsistent behavior at some points [35]. This algorithm defines templates of $m$ points (embedded dimension) and $m+1$ points [36].

Consider a signal $[u(i) : 1 \leq i \leq N]$ of $N$ points. For $\mathrm{ApEn}_{1D}$, a template of $m$ points is defined according to equation 2.2. A template of $m+1$ points is defined similarly.

$$x_m(i) = u(i+k) \text{ with } 0 \leq k \leq m-1 \tag{2.2}$$

To determine the existence of similarity, two templates of the same size are compared [35, 36], based on the Heaviside function (see equation (2.3)) [45]. This comparison is done considering the distance of the two vectors.

The distance, $d_{ij}$, between two templates is defined as the maximum absolute difference of their corresponding scalar components and it is represented by equation 2.4.

$$\theta(i,j) = \begin{cases} 0 & \text{if } d_{ij} > r \text{ (templates not similar)} \\ 1 & \text{if } d_{ij} \leq r \text{ (similar templates)} \end{cases} \tag{2.3}$$

$$d_{ij} = d[x_m(i), x_m(j)] = \max |x_m(i) - x_m(j)| \tag{2.4}$$

If this distance is within the considered tolerance value, $r$, the two vectors are similar. Otherwise, those vectors are not similar (see equation (2.3)) [35, 36]. Since there is no restriction to $i$ being equal to $j$, when this situation happens it is defined as a *self-match*, i.e., the vector is compared with itself giving a positive match.

The following calculations include defining $B_i(r)$ as the number of positive matches for $m$ points and $A_i(r)$ as the number of positive matches for $m+1$ points. Therefore, $B_i^m(r)$ will be the probability of any vector $x_m(i)$ being within $r$ of $x_m(j)$. Similarly, $A_i^m(r)$ defines the probability for any vector $x_{m+1}(i)$ being within $r$ of $x_{m+1}(j)$, considering the same concepts of distance and the same tolerance value. Finally, $B^m(r)$ is defined as the probability of two $m$-sized templates matching each other. $A^m(r)$ is the probability of two $m$-points templates [35].

In the end, Lake *et al.* [37] defines $\text{ApEn}_{1D}$ as being approximately "the negative natural logarithm of the conditional probability that a dataset of length N, having repeated itself within a tolerance $r$ for $m$ points, will also repeat itself for *m+1* points".

Since $\text{ApEn}_{1D}$ [36] considers self-matches, this results in a biased analysis and associated errors [35]. Richman and Moorman [35] studied Cross-$\text{ApEn}_{1D}$, a version that did not admit self-comparisons within the time series. Despite that, lack of relative consistency is revealed [35]. On top of this, a directional dependence exists and sometimes cross-$\text{ApEn}_{1D}$ reveals the existence of undefined values [35].

For these reasons, sample entropy ($\text{SampEn}_{1D}$) [35] emerged as a solution. This measure has similar calculations to $\text{ApEn}_{1D}$ [36] but, excludes self-matches (bias removal) [35, 37, 52] and does not perform a template-wise approach [37]. This translates in defining the equation (2.4) with the restriction $i \neq j$ to exclude self-matches. In this way, the templates are no longer compared with themselves. The following steps are similar to $\text{ApEn}_{1D}$ and the distance value is evaluated once more with the Heaviside function (see equation (2.3)) [35, 37].

Therefore, the entropy definition of $\text{SampEn}_{1D}$ [35] can be considered as exactly "the negative natural logarithm of the conditional probability that a dataset of length N, having repeated itself within a tolerance $r$ for $m$ points, will also repeat itself for *m+1* points, without allowing self-matches" [3] [37]. Besides the consistency improvement, the computational time was also reduced by half when compared to $\text{ApEn}_{1D}$. In addition, this new approach to assess entropy is no longer so dependent on data length [35, 37, 52].

[3] For further detail on $\text{SampEn}_{1D}$ [35], please see chapter 4.

$\text{SampEn}_{1D}$ [35] is considered as an "unbiased estimator" [48]. Nevertheless, having very short signals will affect the $\text{SampEn}_{1D}$'s relative consistency [45, 46]. On the other hand, studying larger signals will be more time consuming due to the cycles involved [45, 46].

Costa *et al.* [39, 43] introduced a multiple scale approach for entropy measurement over multiple scale factors of the signal, after a *coarse-graining* procedure being applied to the signals. The authors used $\text{SampEn}_{1D}$ [35] to measure the entropy values but other entropy measures can be chosen as entropy measures. Once introduced, afterwards, several algorithms were developed using differently the *coarse-graining* procedure, later on discussed.

Viertio-Oja *et al.* [38] considered a combination of frequency-domain and time-domain entropy techniques. This concept is called "Time-frequency balanced spectral entropy" [38]. In the frequency domain, the spectral entropy concept is applied, using the signal's power spectrum to be applied in the *Shannon*'s [51] function. The main advantage of spectral entropy is the separation of any contribution from different range frequencies.

Another alternative is permutation entropy ($\text{PerEn}_{1D}$) [63] an algorithm based on permutation patterns. Consider a time series $\{x_t\}$ for $1 \leq t \leq T$ of length $T$. For each $n!$ permutation, $\pi$, of order $n$ possible the relative frequency, $p(\pi)$, is determined as in equation (2.5) [63].

$$p(\pi) = \frac{\#\{t|t \leq T-n, (x_{t+1}, \ldots, x_{t+n}) \text{ has type } \pi\}}{T-n+1} \tag{2.5}$$

The exact $p(\pi)$ is determined by assuming an infinite time series and consider the limit $T \to \infty$. So, permutation entropy, $H(n)$, of order $n \geq 2$ is defined as in equation (2.6) and the permutation entropy per symbol of order $n$ as $h_n = H(n)/(n-1)$ [63].

$$H(n) = -\sum p(\pi)\log(p(\pi)) \tag{2.6}$$

Bandt and Pompe [63] compares $\text{PerEn}_{1D}$ to zero-crossing rate, suggesting $\text{PerEn}_{1D}$ as complexity parameter for short-time speech analysis. $\text{PerEn}_{1D}$ is assumed as a better indicator than zero-crossing rate. Besides being very fast, this algorithm is highly sensitive to noise which can be a problem for biomedical applications [63].

Afterwards,Chen *et al.* [45, 46] proposed the fuzzy entropy, $\text{FuzzyEn}_{1D}$, an algorithm based on Zadeh's [68] fuzzy sets [4] [45].

As mentioned before, both $\text{SampEn}_{1D}$ [35] and $\text{ApEn}_{1D}$ [36] consider two templates similar or not, i.e, sets the condition to zero or one and are therefore, influenced by *Heaviside* function (a two-state classifier) [46]. Consequently, the points within the considered boundary (tolerance level) have the same weight and the points outside it are excluded [46]. As a result, the tolerance, $r$, will strongly influence the Heaviside function contribution [45, 46].

In fuzzy entropy, the Heaviside function is replaced by a smooth continuous function, fuzzy function, $\mu$, that gives a similarity degree for two template vectors $x_m(i)$

[4] Zadeh [68] considers that, in the physical world, membership criteria might not be that precise. $\text{FuzzyEn}_{1D}$ [45, 46] emerged taking into account the definition of a fuzzy set, i.e, "a class with a continuum of grades of membership" [68].

and $x_m(j)$. The fuzzy function has no rigid boundaries compared to the Heaviside function, leading to smoother results and defined values for entropy analysis [46].

In the original definition by Chen *et al.* [45, 46], the template vector, $x_m(i)$, is defined considering a baseline vector removal (see equation (2.7)), i.e, removing the local mean (see equation (2.8)) [45, 46].

Meanwhile, new publications emerged justifying that this baseline removal will change the system's perception since it no longer takes into account both global and local views [44, 58]. For example, Liu *et al.* [44] had chosen to analyze the signal without local mean and global means. The final entropy is the sum of both signal's entropy. On the other hand, Hilal *et al.* [58] simply chose not to remove any mean. Consequently, the template vectors are represented by equation (2.2), i.e., the template vectors definition is the same as $\text{ApEn}_{1D}$ [36] and $\text{SampEn}_{1D}$ [35].

$$x_m(i) = u(i+k) - u_0(i) \text{ with } 0 \leq k \leq m-1 \tag{2.7}$$

$$u_0(i) = \frac{1}{m}\sum_{k=0}^{m-1} u(i+k) \tag{2.8}$$

As mentioned previously, $\text{FuzzyEn}_{1D}$ [45, 46] is able to measure a similarity degree between two vectors through a *fuzzy function*, using the distance, $d_{ij}$, that is defined by the maximum absolute difference between the vector $i$ and $j$ in equation (2.4) but, with $i \neq j$.

The function chosen by Chen *et al.* [45, 46] was an exponential (see equation (2.9)) owing to the fact that it is well understood and shows a good performance as "fuzzy membership function". This function takes into account the tolerance, $r$, and the fuzzy power, $n$. Afterwards, instead of considering the probabilities $B^m(r)$ and $A^m(r)$ as $\text{ApEn}_{1D}$ [36] and $\text{SampEn}_{1D}$ [35] do, it is obtained the similarity degree ($D_{ij}$) average for $m$ and $m+1$ points, $\phi_i^m$ and $\phi_i^m$, excluding self-matches ($i \neq j$).

Finally, $\Phi^m$ is defined as the average of all $\phi_i^m$, and $\Phi^{m+1}$ as the average of all $\phi_i^{m+1}$, for $1 \leq i \leq N-m$. In the end, $\text{FuzzyEn}_{1D}$ can be defined as the "negative natural logarithm of the deviation of $\Phi^m$ from $\Phi^{m+1}$" [5] [45, 46].

$$\mu = \exp(-(d_{ij}/r)^n) \tag{2.9}$$

The ultimate goal of $\text{FuzzyEn}_{1D}$ was to obtain an unbiased algorithm, able to characterize more complex systems like non-dynamical ones and have consistent results for both short and long time series. Following methods considering fuzzy entropy [45, 46] should consider improving the computational time [45, 46].

Chen *et al.* [46] studied the change of some algorithm parameters and analyzed entropy on synthetic signals. The fuzzy function depends on two parameters, the fuzzy power and the tolerance, and if their values are small, it shows soft and continuous boundaries.

This algorithm presents strong points such as [46]:

- Accuracy

[5] Please note that the both fuzzy entropy algorithms, the original one and the proposed version in this dissertation, are described in full detail in chapter 4.

- Exclusion of self-matches
- Relative Consistency
- Low dependence on time series length
- Less Bias
- Continuity
- Freedom in parameters' selection
- Robust to noise

In the end, $\text{FuzzyEn}_{1D}$ [45, 46] tried to solve the previous algorithms flaws. As it will be shown later, many studies have been using sample entropy [35] to measure signal's irregularity. Regardless, recently, fuzzy entropy [45, 46] is becoming more known due to its proven advantages (over other algorithms) as well as its consistent results. For example, Girault and Humeau-Heurtier [69] also proposed a new strategy to improve the original $\text{FuzzyEn}_{1D}$.

#### 2.2.1.2 Multiscale analysis

The concept of analysis in multiple scales was introduced and involved the procedure called *coarse-graining* [39, 43]. The study over multiple scale factors allows to find out the complexity inherent to biomedical signals, namely the ability to adapt and fit to different environments [60].

Through this procedure of Costa *et al.* [39, 43] an entropy profile over scale factors, $\tau$'s, ia obtained, having the following steps done:

1. A coarse-graining procedure applied on the initial signal, where the system's dynamics is represented in multiple scales.
2. By using $\text{SampEn}_{1D}$ [35], the signals' irregularities are quantified.

Based on this, multiscale sample entropy ($\text{MSE}_{1D}$) [39, 43] used $\text{SampEn}_{1D}$ [35] to measure entropy through several scale factors in order to quantify complexity [61].

Consider a signal $u$ of $N$ points. The coarse-graining procedure down-samples the original signal, $u$, into smaller versions of $N/\tau$, $y^{(\tau)}$, considering $\tau$ a scale factor. The equation (2.10) represents the original method proposed by Costa *et al.* [39, 43].

$$y_j{}^{(\tau)} = \frac{1}{\tau} \sum_{i=(j-1)\tau+1}^{j\tau} u_i,\ 1 \leq j \leq \frac{N}{\tau} \tag{2.10}$$

Basically, the equation (2.10) translates in averaging the data within a $\tau$-sized window first, and then, the average is down-sampled by a factor of $\tau$ (see figure 2.2) [61].

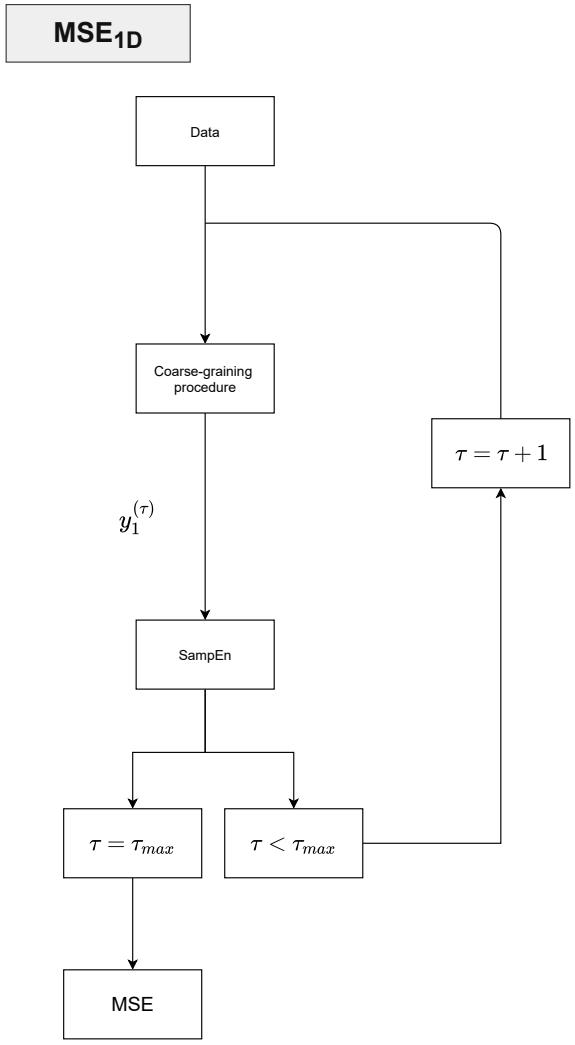


**Figure 2.2:** Flow chart of $\text{MSE}_{1D}$ [39, 43]. Adapted from [48].

These coarse-grained time series, down-sampled versions of the original signal, are used to understand the entropic behavior of the signal besides analyzing the entropy value through the classical method. $\text{MSE}_{1D}$ [39, 43] is used to evaluate complexity efficiently even though there is some issues with short-lengthened data, since the smallest coarse-grained series will be very short [47].

In the coarse-graining step, the data's down-sampling is independent of the entropy measure. Hence, another entropy measure besides $\text{SampEn}_{1D}$ [35] can be chosen in the second step, allowing to obtain a new multiscale approach and study if it outperforms the already existing $\text{MSE}_{1D}$ [39, 43]. The first step, as it will be explained later, can also be modified.

Multiscale entropy analysis can be useful for different systems characterization, namely biological ones. Characterizing pathologic systems and their main differences from healthy ones, combined with their intrinsic complexity can lead to interesting results for many diseases applications [43].

The previous entropy definitions mentioned would only consider entropy on a single scale which could lead to false results [43]. An analysis based on single scale

considers that a higher entropy value corresponds to a more irregular system [35–39, 43].

A system is considered more entropic when there is high variability and more randomness, with the entropy value depending on these two factors [39, 43].

Zhang [50] applied the multiscale approach in physical systems, for the first time, based on *Shannon*'s entropy [51]. Nonetheless, with that approach the data must be noise-free. Hence, making it difficult to analyze and characterize biological systems [43].

$\text{MSE}_{1D}$ [39, 43] is intended to be applied on biological systems. A biomedical (or biological) signal can be studied using classical methods for time series: either by deterministic processes or stochastic ones [39]. Since $\text{MSE}_{1D}$ only quantifies the different complexity degrees [39, 61], it does not assume such classical definitions [39].

This procedure to quantify the complexity can have some drawbacks. For example, since the averaged data becomes smaller as the scale factor, $\tau$, increases, for short data, the entropy's variance values rises rapidly, reducing reliability [61]. Consequently, $\text{SampEn}_{1D}$ [35] can translate imprecise entropy values and determining a short signal's entropy can be a very hard task [61]. For large scale factors, $\text{MSE}_{1D}$ [39, 43] besides inaccurate results, undefined values can be existent due to absence of template's matches [48]. The lack of accuracy and validity will reflect on reliability reduction [66].

Moreover, the equation behind coarse-graining in $\text{MSE}_{1D}$ has been reported as similar to a FIR filter, a low pass filter [70]. These filters have a poor response and aliasing is not prevented upon down-sampling. In consequence, the down-sampled time-series will be biased [61].

As mentioned previously, alterations in the coarse-graining procedure can be introduced and these developments emerged with the necessity of correcting the $\text{SampEn}_{1D}$'s [35] imprecision and lack of reliability in the multiscale procedure [47].

Costa and Goldberger [59] introduces multiscale sample entropy based on variance, $\text{MSE}_{1D\sigma^2}$. $\text{MSE}_{1D}$ [39, 43] uses the mean value for coarse-graining time series whereas $\text{MSE}_{1D\sigma^2}$ uses variance to quantify the system's dynamics. The family of $\text{MSE}_n$ is introduced using different $n$ moments such as the mean (first moment), $\mu$. Variance (second moment), $\sigma^2$, is the one chosen to study cardiac interbeat interval time series, trying to enhance underlying processes with important information probably missed using just $\text{MSE}_{1D}$. Once the coarse-graining procedure is performed, the $\text{SampEn}_{1D}$ [35] is applied for each scale factor [59].

Later on, Wu *et al.* [47] suggested the use of another algorithm: the modified multiscale sample entropy ($\text{ModMSE}_{1D}$[6]) [47], which is also applied to bidimensional data [55]. This technique involved an overlapping moving-average [55]. $\text{ModMSE}_{1D}$ uses a time delay, increasing the number of templates implying therefore, a much higher computational cost. On the other hand, having more templates decreases the probability of having undefined values. The precision is improved, being therefore, more reliable than $\text{MSE}_{1D}$ [39, 43] for short time series [47]. For long time-series, the accuracy is similar between the two methods so, the $\text{ModMSE}_{1D}$ computational cost is not justified. Therefore, $\text{MSE}_{1D}$ is usually the standard choice for those cases

[6] $\text{MMSE}_{1D}$ can also be used to mention modified multiscale sample entropy.

[47].

Furthermore, composite multiscale entropy ($CMSE_{1D}$) [48] was also developed to overcome $MSE_{1D}$'s [39, 43] problems [48]. The $CMSE_{1D}$'s coarse-graining procedure defines $\tau$ coarse-grained time series, $\{y_1^\tau, y_2^\tau, \ldots, y_k^\tau\}$ with $1 \leq k \leq \tau$, in opposition to $MSE_{1D}$ that only has one for each scale factor, $y_1^\tau$ (please see figures 2.2 and 2.3) [48, 61].

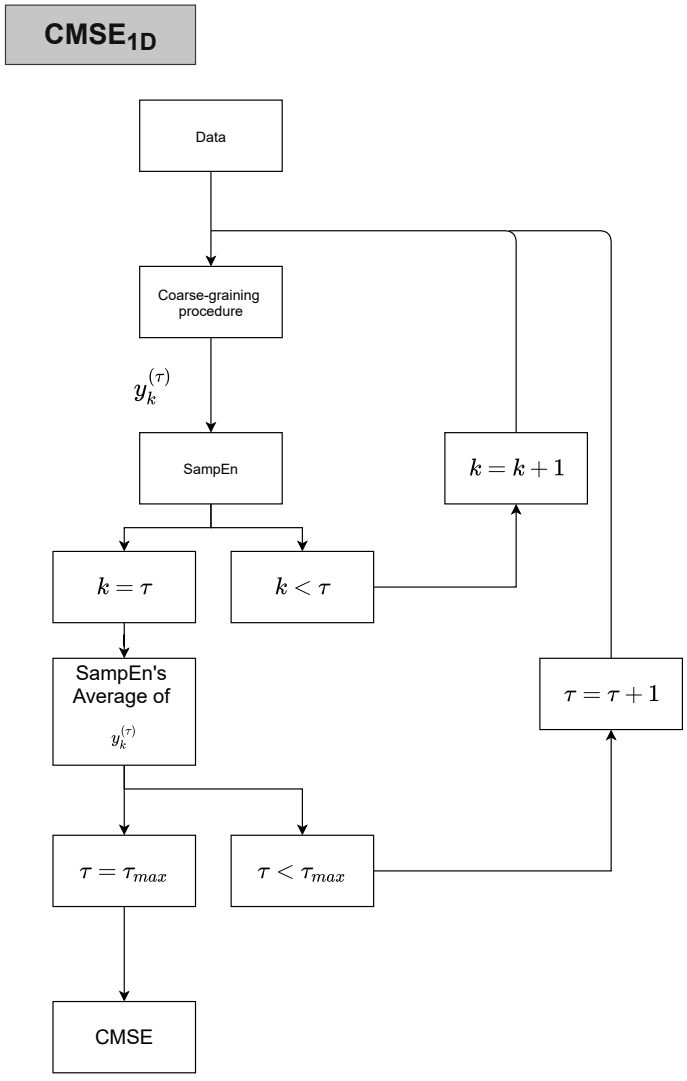


**Figure 2.3:** Flow chart of $CMSE_{1D}$ [48]. Adapted from [48].

$SampEn_{1D}$ [35] is applied to each coarse-grained time series. The entropy's final value for each scale factor must be the mean of the entropy values calculated previously [48]. Wu *et al.* [48] work achieved higher reliability for larger $\tau$'s although showing only slightly better results for the smaller ones. Moreover, accuracy was also improved. In addition, for feature extraction, for the given application (bearing vibration signals), the results obtained with $CMSE_{1D}$ were better [48].

Despite the mentioned advantages, the composite version was not able to solve the issue of having undefined entropy values when considering large scale factors. Since $CMSE_{1D}$ [48] has more logarithmic calculations for each scale factor associated

to a posterior average procedure, the probability of having undefined values is in fact higher than for $MSE_{1D}$ [39, 43] [66].

As a solution for the previous problem, Refined Composite Multiscale Entropy [66], $RCMSE_{1D}$, was developed, being able to improve accuracy. Similarly to $CMSE_{1D}$ [48], for each scale factor there are $\tau$ coarse-grained time series, $y_k^{(\tau)}$ (please compare figures 2.3 and 2.4). In order to reduce the probability of having undefined values, the authors suggested obtaining first the mean value of the number of matches for $m$ and $m+1$-points for every $\tau$ coarse-grained series within each scale factor [66].

Figure 2.4 shows that for every $y_k^{(\tau)}$ the number of matches for templates of $m$ and $m+1$ points, $n_{k,\tau}^m$ and $n_{k,\tau}^{m+1}$, respectively, is calculated [66]. Then, it is obtained the mean value of $n_{k,\tau}^m$ and $n_{k,\tau}^{m+1}$ between $1 \leq k \leq \tau$, $\bar{n}_{k,\tau}^m$ and $\bar{n}_{k,\tau}^{m+1}$. Afterwards, the logarithm operation involved in $SampEn_{1D}$ [35] is performed on those values (see figure 2.4) [66].

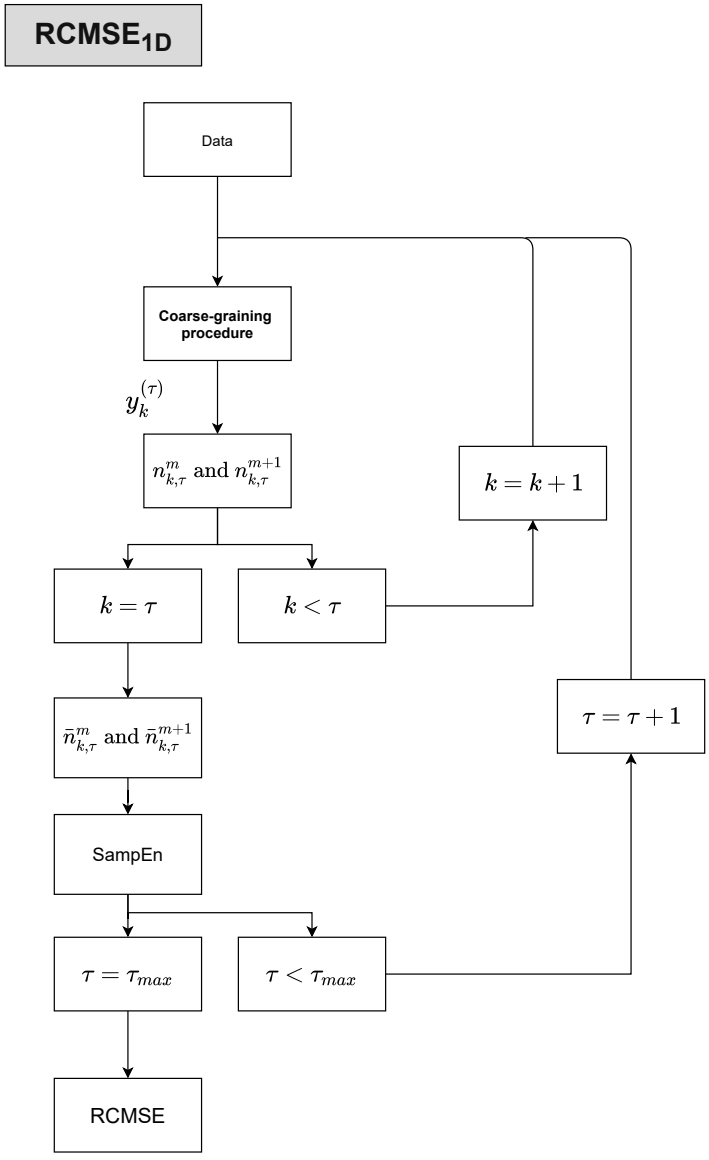


**Figure 2.4:** Flow chart of $RCMSE_{1D}$ [66].

$RCMSE_{1D}$ [66] have not shown undefined values in opposition to the previous versions. Hence, it was proven to be superior in terms of validity. Besides being more accurate, $RCMSE_{1D}$ seems to be less dependent on data length, showing more consistency than $MSE_{1D}$ [39, 43] and $CMSE_{1D}$ [48]. Moreover, $RCMSE_{1D}$ showed slightly better computational time than $CMSE_{1D}$ since it only requires a logarithm operation instead of $\tau$ times as $CMSE_{1D}$ does. However, $MSE_{1D}$ still outperforms this last two in terms of computational cost (only has one coarse-grained time series per scale factor) [61, 66]. Since for large signals, $RCMSE_{1D}$'s improvements have not been very significant when compared to $MSE_{1D}$, for this situations the standard choice is $MSE_{1D}$ [60].

Taking into account the fuzzy entropy [45, 46] advantages, like a smaller standard deviation and best entropy characterization, multiscale versions have been developed. Multiscale fuzzy entropy ($MFE_{1D}$) [64] uses the first step of coarse-graining the data, as explained for $MSE_{1D}$ [39, 43] with only changing the entropy measure applied in the second step. Therefore, when measuring entropy with $FuzzyEn_{1D}$ [45, 46], better accuracy, more relative consistency, freedom in parameter selection, and higher computational cost are expected [45, 46].

Liu *et al.* [44] and Xiong *et al.* [57] also proposed a multiscale version of fuzzy entropy with some changes in the original fuzzy entropy definition [45, 46]. In both articles, the multiscale procedure remains similar to Costa *et al.*'s [39, 43] definition.

Furthermore, Azami *et al.* [60] introduced Refined Composite Multiscale Fuzzy Entropy, $RCMFE_{1D}$, and Refined Composite Multiscale Fuzzy Entropy based on standard deviation, $RCMFE_{1D\sigma}$. These algorithms establish coarse-graining procedures similar to $RCMSE_{1D}$ [66] and $MSE_{1D\sigma^2}$ [59], respectively. The difference between the two refined algorithms is in the definition of the coarse-grained series that can involve either a mean definition based procedure or a variance definition based procedure [60]. Both $RCMFE_{1D}$ algorithms were shown to be the most stable entropy evaluators among the 12 algorithms tested by Azami *et al.* [60] and multiscale methods based on SD may have better performances for short scale factors than those based on variance [60].

Although better computational time is achieved with $SampEn_{1D}$ [35], entropy based on fuzzy sets allows stronger relative consistency and less dependence on the data's length [46, 60]. Herein, the proposed fuzzy entropy, $FuzEn_{1D}$, and multiscale version will be shown in section 4.1.2, where a detailed mathematical view and main characteristics are presented.

### 2.2.2 Entropy measures for multidimensional data

In order to analyze images and volumes, the need to apply entropy evaluators in multidimensional data emerged, based on previously presented concepts of approximate [36], sample [35] and fuzzy entropy [45, 46] as well as their multiscale versions [39, 43, 44, 57, 64]. Bioinformatic imaging can be able to extract important information from images [71].

Entropy measures extended to bidimensional definitions extracts information for the studying images' irregularity, using similarity patterns concept [58]. Some bidimensional entropy measures have been proposed with many applications in the

biomedical area. Recently, the concern to study sets of images, composing 3D volumes, has emerged with the goal of assisting on medical diagnosis [53, 54] or to characterize cell structure [71].

#### 2.2.2.1 Single scale analysis

Entropy measurement algorithms rapidly became tools of great interest for multidimensional area, especially for application on images. Later on, towards a deeper analysis, multiscale studies emerged to reveal the complexity behavior of images.

Bidimensional data can be classified using bidimensional permutation entropy ($\text{PerEn}_{2D}$) [65], a simple method that uses the distribution of permutation probability in order to obtain the entropy. The final entropy definition is based on *Shannon*'s entropy [51]. Even though this method is very fast, like the one-dimensional version, $\text{PerEn}_{2D}$ is very sensitive to noise [65].

Sample entropy's concept was extended to be analyze texture of images [52]. Bidimensional sample entropy ($\text{SampEn}_{2D}$) [52] aims at separating different sets of images and to discriminating those groups. Even though robustness is verified, the computational cost increases as the image's size increases [52]. Silva *et al.* [52] present this irregularity measure as a better image classifier when compared to *Haralick* and *wavelet descriptors*. Presented as an extension of $\text{SampEn}_{1D}$ [35], the templates are squared windows classified by the *Heaviside* function. If the templates' distance is within the tolerance value, $r$, then a match occurs. Otherwise, the existence of a match is not considered [35, 52]. Additionally, $\text{SampEn}_{2D}$ is expected to have higher entropy (higher irregularity) for more random images. Moreover, increasing the number of pixels will allow to increase accuracy as a result of increased matched patterns [52].

As mentioned before, for very small $N$ length time series, $\text{SampEn}_{1D}$ [35] could present undefined and inaccurate values. Consequently, being an extension of sample entropy's definition, $\text{SampEn}_{2D}$ [52] can also present undefined and/or inaccurate results [56].

Bidimensional distribution entropy [56], $\text{DistrEn}_{2D}$, was developed to be used in both real and synthetic textures. In addition, $\text{DistrEn}_{2D}$ presents a similar advantage to $\text{FuzzyEn}_{1D}$ [45, 46]: more independent choice of parameters and less affected results by size with good performance even for small patterns [56]. The templates are also squared. Upcoming, the entropy is based on a histogram with $M$ bins. Afterwards, empirical probability density function, ePDF, can be estimated and the probabilities of each bin, $p_t$, can be known (with $1 \leq t \leq M$). In the end, entropy measurement is based on the Shannon's [51] entropy definition [56]. $\text{DistrEn}_{2D}$ is faster, less dependent on image's size, without undefined values and detects noise signals and periodical textures [56]. Despite that, this measure is applied to small textures [72].

Recently, Azami *et al.* [72] proposed the dispersion entropy 2D, $\text{DispEn}_{2D}$, with some main advantages over $\text{SampEn}_{2D}$ [52] like the absence of undefined values, faster method and more stable results. This technique maps the pixels in different classes and assign the possible dispersion patterns to the template. Once that step is performed, the relative frequencies of patterns are obtained and used to obtain *Shannon*'s entropy [51].

Due to the advantages shown in uni-dimensional data, the bidimensional version of $\text{FuzzyEn}_{1D}$ [45, 46] could be of great use in multidimensional data. In order to assist in medical diagnosis of *Pseudoxanthoma Elasticum*, PXE, a skin condition,Hilal *et al.* [58] proposed bidimensional fuzzy entropy, $\text{FuzEn}_{2D}$ [7], and its multiscale version. The goal of $\text{FuzEn}_{2D}$ is similar to the 1D version so, maintaining its main characteristics is imperative [58]. The templates are once more defined as squared windows. The authors of $\text{FuzEn}_{2D}$ were able to prove, by opposition to $\text{SampEn}_{2D}$ [52], $\text{FuzEn}_{2D}$ does not depend on the $m$ parameter to have defined values. In addition, the profiles maintained very consistent behavior even for smaller images.

Moreover, in another study, also about bidimensional fuzzy entropy, Hilal and Humeau-Heurtier [73] studied the behavior upon rotation and translation, performed validation on synthetic signals, a common procedure among entropy measures. In addition, presented as biomedical application dermoscopic images for evaluation of melanoma and melanocytic nevi, malignant and benign skin lesions, respectively.

Hilal and Humeau-Heurtier [73] concluded that the low sensitivity to change in parameters is maintained from the one-dimensional version. Also, the algorithm is both invariant upon translation or rotation, and finally, that it is more reliable than $\text{SampEn}_{2D}$ [52]. Furthermore, the authors indicate that $\text{FuzEn}_{2D}$ is suitable to apply on dermoscopic images [58].

Unfortunately, $\text{FuzEn}_{2D}$ [58, 73] and the previous bidimensional entropy measures do not deal with colored images. Consideration of Red (R), Green (G) and Blue (B) color channels in images to evaluate their complexity could reveal interesting and important results. Recently, Santos *et al.* [74] introduced multidimensional and fuzzy sample entropy ($\text{SampEn}_{MF}$) to evaluate colorectal cancer colored histological images. Nonetheless, this measure does not account for particular color channels.

Furthermore, entropy approaches using approximate entropy 2D [71], $\text{ApEn}_{2D}$ and approximate entropy 3D [53, 54], $\text{ApEn}_{3D}$ were published. Marchant *et al.* [71] stated that, so far, little applications of $\text{ApEn}_{2D}$ in images was done. The authors presented a version of $\text{ApEn}_{1D}$ [36] applied to a region of interest surrounding a certain point [53, 54, 71]. $\text{ApEn}_{2D}$ and $\text{ApEn}_{3D}$ definitions are proposed as tools for quantifying orderness of structures, for example, distinguishing cancer cells from normal ones [71].

Since these new definitions modified the concept of distance between templates [8], it needed validation from the authors [53, 71]. Moore and Marchant [54] claimed that the associated unreliability to $\text{ApEn}_{1D}$ [36] is reduced in $\text{ApEn}_{3D}$. However, previous works mentioned several times the lack of accuracy inherent to the use fo approximate entropy [35, 37, 39, 43, 45, 46, 52, 59]. In addition, the authors state that the $\text{ApEn}_{3D}$'s lack of accuracy does not represent an important flaw since it can have high applicability as a regularity indicator [54].

One can say that the future work on biomedical 3D applications can be based on three-dimensional fuzzy entropy, including the multiscale version. Hence, due to the

[7] It was chosen to represent as $\text{FuzEn}_{2D}$ and not $\text{FuzzyEn}_{2D}$ due to the similar modification performed in our proposed algorithms. Hilal *et al.* [58] chose not to perform a baseline removal upon the templates in opposition to the original definition, FuzzyEn [45, 46].

[8] Considering the mean of absolute differences of corresponding pairs instead of their maximum.

need of a colored bidimensional fuzzy entropy [75] (specifying RGB color channels) and of three-dimensional fuzzy entropy measures, on sections 4.2.1.2 and 4.1.2 are shown respectively, the proposed and developed algorithms during this project.

#### 2.2.2.2 Multiscale analysis

In light of the multiscale analysis of signals, with their complexity being revealed, this approach was adapted to bidimensional data for a more detailed analysis on images. Thus, considering definitions of $MSE_{1D}$ [39, 43] and $ModMSE_{1D}$ [47], the coarse-graining procedure suffered an adaptation so $SampEn_{2D}$ [52] could be used in a multiscale approach [55]. Therefore, multiscale sample entropy 2D ($MSE_{2D}$) [55] and modified multiscale sample entropy 2D $ModMSE_{2D}$ [55] emerged.

Silva *et al.* [55] decides to compare both two-dimensional coarse-graining procedures, $MSE_{2D}$ and $ModMSE_{2D}$. Due to the time delay introduction of $ModMSE_{2D}$, there are more pattern to calculate the entropy in $ModMSE_{2D}$. Therefore, this algorithm is slower than $MSE_{2D}$ but shows a much better accuracy, as expected. For $MSE_{2D}$, increasing the number of scale factors into the analysis can mean increasing the probability of having undefined values, diminishing the accuracy even more [55], specially for small images.

As consequence, bidimensional multiscale fuzzy entropy based approaches are more reasonable options. Hilal *et al.* [58] and Hilal and Humeau-Heurtier [73] considered the advantageous fuzzy entropy in their studies. The main characteristics to point out are the insensitivity to rotation and translation, synthetic images discrimination, ability to differentiate complexity levels and insensitivity for parameters change [58, 73].

In the future, many studies focused on three-dimensional multiscale analysis, besides the one proposed in this project, are expected to be proposed.

# 3 Materials

The following chapter describes the one-dimensional and multidimensional data used to test the entropy algorithms developed during this project. First, the synthetic data is presented and afterwards, the biomedical data.

## 3.1 Synthetic signals

For the validation tests performed on the 3 versions of fuzzy entropy, $\text{FuzEn}_{1D}$, $\text{FuzEn}_{C2D}$, and $\text{FuzEn}_{3D}$, synthetic data was used namely, $\text{MIX}(p)$ processes-based signals, images, or volumes, respectively. Moreover, colored noise signals have been used to evaluate $\text{FuzEn}_{1D}$ and $\text{FuzEn}_{3D}$. The Colored Brodatz database [76, 77] allowed to validate $\text{FuzEn}_{C2D}$. Finally, pattern-based cubes were used to test the ability of $\text{FuzEn}_{3D}$ irregularity identification.

### 3.1.1 MIX($p$) processes

$\text{MIX}(p)$ processes [36] corresponds to signals with two different components: a deterministic and a stochastic one [46]. When the deterministic component prevails the entropy value become lower but, if the stochastic component prevails then, the entropy value increases [36].

In the studies including $\text{MIX}(p)$ processes-based signals, it is expected to observe increasing entropy for an increasing $p$-value, as it will be explained afterwards. This will prove the ability of fuzzy entropy to discriminate different levels of irregularity.

To obtain a well defined entropy curve as function of the probability, several $p$-values were considered. For each $p$-value, 10 signals/images[1]/volumes have been generated, presenting, afterwards, the mean entropy value of those signals/images/volumes. Moreover, the curves of original $\text{MIX}(p)$ processes based signals, images or volumes, have been compared with their shuffled versions.

Further on, one-, bi-, and tri-dimensional definitions of $\text{MIX}(p)$ processes are shown and described.

#### 3.1.1.1 Unidimensional definition

Pincus [36] introduces the definition of these synthetic signals and considers a "family of independent identically distributed (i.i.d.) real random variables", $y_j$. The stochastic signal $y_j$ is composed by random numbers uniformly distributed between $[-\sqrt{3}, +\sqrt{3}]$. The deterministic component, $x_j$, is defined as a sinusoidal signal in equation 3.1.

$$x_j \;=\; \sin(\frac{2\pi j}{12}) \tag{3.1}$$

$$MIX(p) = (1 - z_j)x_j \;+\; z_j y_j \tag{3.2}$$

[1] As we will explain later on, we added the $\text{MIX}(p)$ based images to a checkerboard background.

According to the choice of parametric probability $p$ ($0 \leq p \geq 1$), the resultant synthetic signal will be more dominated by the random dynamics or by the sine periodic function [52]. For a higher $p$-value the signal becomes more random and for a $p$-value close to zero the signal is ruled by order. The expression for $MIX_{1D}(p)$ processes is defined as in equation 3.2.

Therefore, $z_j$, a random variable, assume the value 0 with probability of $1 - p$ and is 1 with probability $p$ [46].

The signals generated using this definition and further used in validation tests have a size of $N = 3 \times 10^4$ points each. The first test involving $\text{MIX}_{1D}(p)$ intended to verify if for an increase of $p$, an increase of entropy is observed. Moreover, it also intended to analyze the sensitivity upon the $m$ (embedding dimension) parameter. Then, these type of signals have been used to verify if $\text{FuzEn}_{1D}$ can identify the process of shuffling data. At last, the curves of $\text{FuzEn}_{1D}$ and $\text{FuzzyEn}_{1D}$ [45, 46] are compared.

#### 3.1.1.2 Bidimensional definition

Based on the one dimensional process, $\text{MIX}_{2D}(p)$ [52] can be defined as:

$$MIX_{2D}(p) = (1 - Z_{i,j})X_{i,j} \; + \; Z_{i,j}Y_{i,j} \tag{3.3}$$

The signal $X_{i,j}$ is defined as a sinusoidal image (equation 3.4) and $Y_{i,j}$ is an image composed by random number uniformly distributed with a range of $[-\sqrt{3}, +\sqrt{3}]$. $Z_{i,j}$ is a random variable which can assume the value 0 with probability $1 - p$ or the value 1 with $p$ probability [52].

$$X_{i,j} \; = \; \sin(\frac{2\pi i}{12}) \; + \; \sin(\frac{2\pi j}{12}) \tag{3.4}$$

Once more, when the $p$-value increases, an increase on entropy is expected [52].

As it will be discussed in section 3.1.4, each image tested that contained $\text{MIX}_{2D}(p)$ processes had a size of $256 \times 256$ pixels. These images have been used to test the bidimensional $\text{MIX}(p)$ data theory and the sensitivity to $m$ parameter. Following that, it has been verified if, as expected, the entropy increases with shuffling data.

#### 3.1.1.3 Tridimensional definition

In order to study the performance and behavior of tri-dimensional entropy measures, the $\text{MIX}(p)$ processes 3D definition is proposed as in equation 3.5:

$$MIX_{3D}(p) = (1 - Z_{i,j,k})X_{i,j,k} \; + \; Z_{i,j,k}Y_{i,j,k} \tag{3.5}$$

$$X_{i,j,k} \; = \; \sin(\frac{2\pi i}{12}) \; + \; \sin(\frac{2\pi j}{12}) + \; \sin(\frac{2\pi k}{12}) \tag{3.6}$$

Similarly to the previous versions, $\text{MIX}_{1D}(p)$ and $\text{MIX}_{2D}(p)$, for $\text{MIX}_{3D}(p)$ there are two components behind this synthetic volume: a stochastic and deterministic component. The first, $Y_{i,j,k}$, is a volume constituted by random numbers following an uniform distribution within the interval $[-\sqrt{3}, +\sqrt{3}]$. The second one, $X_{i,j,k}$, is

a volume with sinusoidal behavior (see equation 3.6). Defining $Z_{i,j,k}$ as a random variable assuming the value 0 with $1-p$ probability and the value 1 for $p$ probability, for a higher $p$-value the entropy is expected to be higher.

Further on, the $\text{MIX}_{3D}$ $(p)$ volumes used in validation tests have a size of $50 \times 50 \times 50$ voxels. For these volumes generated with $\text{MIX}_{3D}(p)$, the entropy values were obtained through tridimensional fuzzy entropy algorithm ($\text{FuzEn}_{3D}$) proposed in this dissertation. Their behavior upon change in the $m$ parameter has been also analysed. Following that, it has been verified if, as expected, the entropy increases when shuffling data.

### 3.1.2 Colored noise signals

The colored noise signals were generated by MATLAB® function `randnd` [78]. The noise signals used on this project were white, pink, brown, and blue noise. Based on previous analyze [39, 43], colored noise signals/volumes characterization has been done as a validation method of multiscale entropy measures.

#### 3.1.2.1 Unidimensional data

As said before, a MATLAB® function was used to generate several types of noises. These signals had a mean value of $\mu = 0$ and standard deviation equal to $SD = 1$.

These signals present a power spectral density (PSD) dependence with $1/|f|^{\beta}$: $\beta = 0$ for white noise, $\beta = -1$ for pink noise, $\beta = +1$ for blue noise, and $\beta = -2$ for brown noise. Figure 3.1 shows the PSD of each studied signal and the linear fit performed. The estimated $\beta$ values are shown in table 3.1.

**Table 3.1:** $\beta$ values for colored noise signals with a power spectral density (PSD) dependence of $1/|f|^{\beta}$. The estimated $\beta$ value was obtained doing a linear fit to the noise's PSD.

| Noise | Theoretical $\beta$ | Estimated $\beta$ |
|---|---|---|
| White | 0 | 0.0098 |
| Pink | $-1$ | $-0.9950$ |
| Blue | $+1$ | $+1.0008$ |
| Brown | $-2$ | $-2.0143$ |

Typically, the tested noise signals had a length of $N = 30000$ points. However, to compare the length dependence of sample entropy with the low dependence of fuzzy entropy, we used short pink noise signals of $N = 100$ points. In every analysis, we always consider 10 signals for each noise type and the final value is the mean entropy of those signals.

Moreover, white noise signal has been used to test the fuzzy entropy algorithm's sensitivity to the tolerance parameter. Later on, using the same 10 white noise signals for both algorithms, we compared the $\text{SampEn}_{1D}$ and $\text{FuzEn}_{1D}$ regarding the tolerance sensitivity of the algorithms. Although the tests have been done with

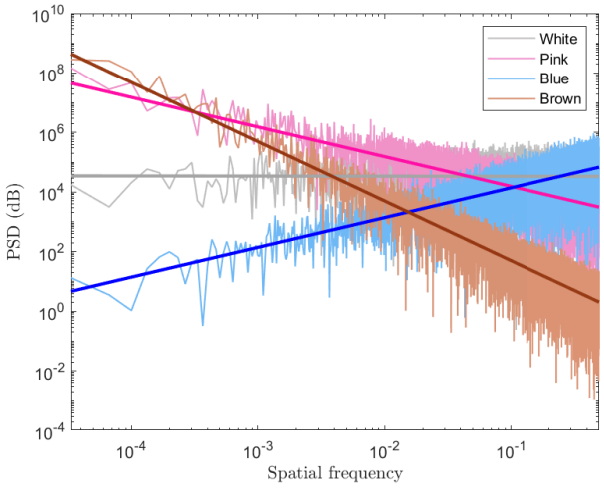


**Figure 3.1:** Power spectral density (PSD) and respective linear fit of white noise (gray), blue noise (blue), pink noise (pink) and brown noise (brown).

white noise, $\beta = 0$, other colored noise or known signal could have been tested. The goal was to simply analyze entropy behavior upon change of tolerance rather than entropy values.

Regarding multiscale analysis, we used white, pink, blue, and brown noise. These signals have been submitted to a multiscale analysis for further algorithm validation, comparing the results with literature. This included a comparison of the entropy curves obtained with $\text{SampEn}_{1D}$ [35] and $\text{FuzEn}_{1D}$. In addition, by extending the analysis to blue and brown noise besides white and pink noise, a complexity characterization of these noises was possible.

As mentioned before, in addition, pink noise signals have been used to compare the length dependence of $\text{SampEn}_{1D}$ with $\text{FuzEn}_{1D}$.

#### 3.1.2.2 Tridimensional data

The tri-dimensional colored noise data, i.e., colored noise volumes, were generated with the same function as for the unidimensional data. Statistically, the data had a mean value of $\mu = 0$ and standard deviation of $SD = 1$. We considered 10 cubes for each noise, presenting the mean entropy value as the final one. In addition, these synthetic volumes have a size of $50 \times 50 \times 50$ voxels.

Similarly to the 1D case, these colored noise volumes show a PSD dependence of $1/|f|^{\beta}$ with $\beta = 0$ for white noise, $\beta = -1$ for pink noise, $\beta = +1$ for blue noise, and $\beta = -2$ for brown noise, as shown in figure 3.1.

These volumes have been used to test the sensitivity of $\text{FuzEn}_{3D}$ to change of $r$ and $m$ values. In order to do that, we used the same 10 white noise volumes to calculate the entropy for each tolerance and embedding dimension. Similarly to $\text{FuzEn}_{1D}$ analysis, the choice of noise is not that important. The goal is once more to analyze the algorithm's behavior and not the values per say.

We tested these signals at a multidimensional level, including brown and blue noise, through a multiscale analysis.

### 3.1.3 Colored Brodatz images

Abdelmounaime and Dong-Chen [76] presented the Colored Brodatz (CB) dataset as an extension of the Brodatz gray-scaled database, used in several other studies for validation. These images are reported to be rich in textural and chromatic content [76]. We chose seven of these images for validation purposes as well (see figure 3.2) [76, 77]. The figure 3.2 (a) of $256 \times 256$ pixels has been used to test the sensitivity of $\text{FuzEn}_{C2D}$ algorithm to change of tolerance values and $m$-values. The remaining figures, figures 3.2 (b)-3.2 (g), were posteriorly sub-divided into 4 smaller images of $320 \times 320$ pixels to test if a smaller portion of a certain image would be recognized as having a similar textural behavior as the original one.

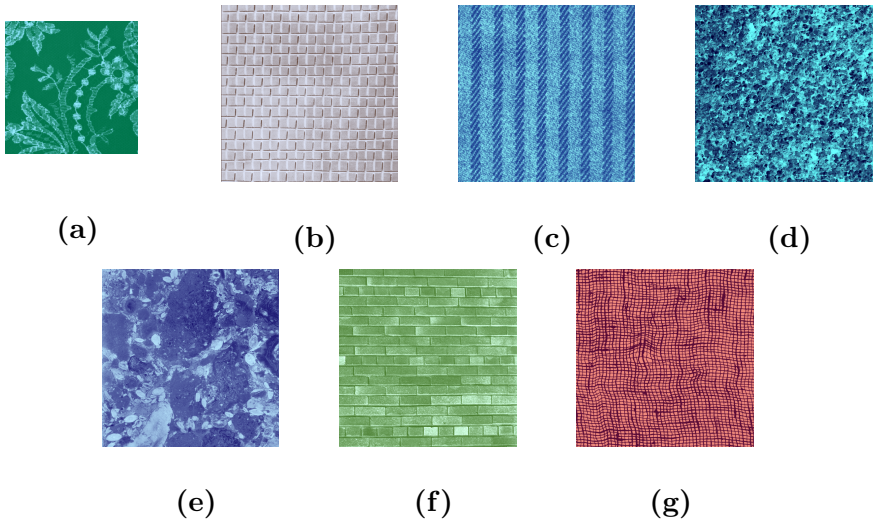


**Figure 3.2:** Colored Brodatz image used for $\text{FuzEn}_{C2D}$ tolerance sensitivity study (a) and textural behavior of sub-images test (b-g) of $256 \times 256$ and $640 \times 640$ pixels, respectively.

### 3.1.4 $\text{MIX}_{2D}(p)$ processes-based image with checkerboard background

We mentioned that $\text{MIX}(p)$ processes can help in the evaluation of an algorithm's ability to differentiate different irregularity levels. Therefore, we generated images composed by $\text{MIX}_{2D}(p)$ processes but, in order to have colored images, we added a background in each channel. Consequently, each image's channel, $\mathbf{U}_C$, is constituted by a checker board background.

In figure 3.3 (c), representing the blue channel, $\mathbf{U}_B$, we can observe that $\mathbf{U}_B$ is actually a version of $\mathbf{U}_R$ and $\mathbf{U}_G$ checkerboard, figures 3.3 (a) and 3.3 (b), respectively, but rotated by 90 degrees. In the end, we obtained a colored image (see figure 3.3 (d)).

The checkerboard pattern is known for having an entropy equal to zero due to its highly regular structure. By choosing this background, thee entropy behavior would only depend on $\text{MIX}_{2D}(p)$ processes-based images and therefore, we could expect that an increase of $p$ should also increase entropy in order to validate the algorithm.

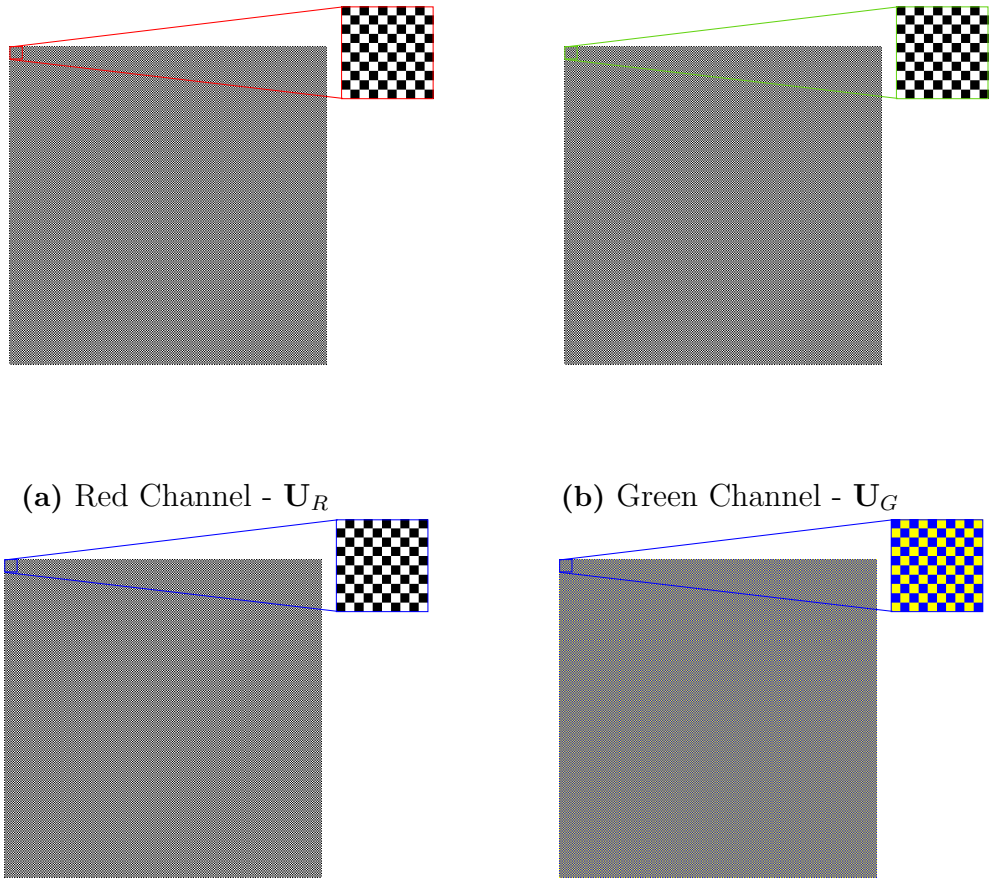

**(a)** Red Channel - $\mathbf{U}_R$ **(b)** Green Channel - $\mathbf{U}_G$

**(c)** Blue Channel - $\mathbf{U}_B$ **(d)** Final checkerboard image,$\mathbf{U}$.

**Figure 3.3:** Representation of the colored image background used for $\text{MIX}_{2D}(p)$ processes with a size of $256 \times 256$ pixels

We represented 3 examples of images with 3 different $p$-values, figures 3.4 (a)-3.4 (c), containing a checker board background with $\text{MIX}_{2D}(p)$-based images. The final images have a size of $256 \times 256$ pixels.

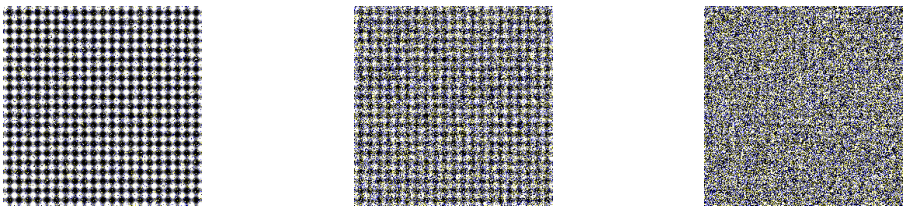

**(a)** $p = 0.1$ **(b)** $p = 0.5$ **(c)** $p = 0.9$

**Figure 3.4:** $\text{MIX}_{2D}(p)$ processes-based images with a checker board background with $256 \times 256$ pixels.

### 3.1.5 Tridimensional patterns

Similarly to what can be performed on bidimensional data, Moore and Marchant [54] identified the most irregular patterns in a volumes group composed by different pattern structures. Based on this analysis, as a validation method and to prove the choice of the embedding dimension parameter, $m$, we tested six different cubes of $50 \times 50 \times 50$ voxels and identified the most irregular cube using $\text{FuzEn}_{3D}$. These cubes are represented in figure 3.5.

The first cube, figure 3.5 (a), has only 1 value very close to zero ($1 \times 10^{-9}$). This value choice is to prove that for a cube constituted by zeros (or close to) the entropy is zero. We did not define each voxel with an exact zero value because that would lead to an undefined entropy value (the only exception on the algorithm). Besides, no real data would have exact zero values but more likely approximately zero values.

In figure 3.5 (b), we represent a cube pattern with an half composed by zeros and the other one by ones. The third cube, figure 3.5 (c), shows a checkerboard pattern. Additionally, the fourth cube, figure 3.5 (d), has diagonal stripes. These first 4 cubes are expected to be more regular than the last 3 due to their pattern nature.

Finally, the cube 5, figure 3.5 (e), follows a Gaussian distribution with a mean $\mu = 10$ and standard deviation of $SD = 1$ and cube 6 is constituted integer values following a uniform random distribution between 1 and 10.

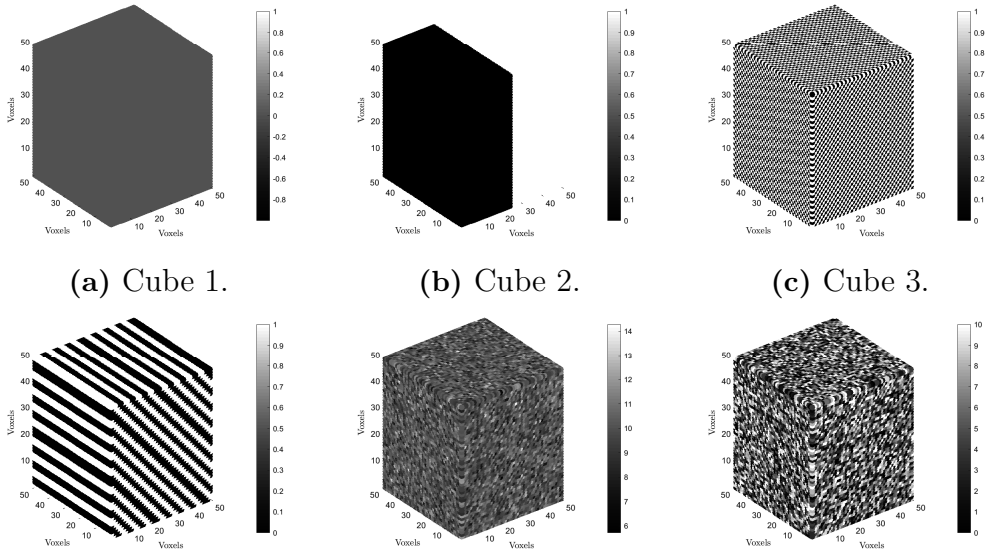


**(a)** Cube 1. **(b)** Cube 2. **(c)** Cube 3.

**(d)** Cube 4. **(e)** Cube 5. **(f)** Cube 6.

**Figure 3.5:** Tri-dimensional patterns used in $50 \times 50 \times 50$ voxels sized cubes, for validation purposes.

This analysis allowed besides validating the algorithm, to quantify the irregularity of different patterns.

## 3.2 Biomedical signals

The following sections are dedicated to explain the details behind signals, images or volumes used in the biomedical applications in this project. First, are mentioned the audio signals containing snoring events provided by MSc *Tiago Marçal* and that previously involved the collaboration of Dr. José Moutinho from Centro de Medicina do Sono, CHUC (article of reference [62]); secondly, are mentioned the dermoscopic images collected by Dr. Clémence Berthin of University Hospital of Angers, France, for the microcirculatory study included in this thesis document and in the article of reference [75], and the dermoscopic images used from a public database [79, 80] to identify melanoma; finally, it is mentioned the volumes (lung's portions) obtained from CT scans data provided by University Hospital of Rennes, France, to identify IPF.

### 3.2.1 Audio snore related signals

We conducted a study on snore related audio signals to find out their entropic behavior. The study involved 25 subjects: 5 of them suffered from severe SAHS, 5 suffered from moderate SAHS, 5 suffered light SAHS, another 5 had simple snoring condition and finally, the last 5 represented group control. As said before, these signals have been provided and collected by MSc *Tiago Marçal*, during his Ph.D. project.

For each subject, we manually selected 50 snores from the corresponding audio file with the original sampling rate of $f_s = 44.1$ kHz. Each snoring signal has been selected to have $N = 6.5 \times 10^4$ points. After recognizing where the snoring event starts, we defined the initial point and consider the $N - 1$ points that follow.

Even though we chose $N = 6.5 \times 10^4$ points, snoring does not always have the same duration. For example, some snores are longer and having $6.5 \times 10^4$ points only includes a snore portion. However, when the snore event is shorter we may include other respiratory sounds. This size allows to have both short and long snoring events without discarding relevant information or including non-relevant additional one. Our goal is towards analysis of the first moments where clearly the air obstruction affects the breathing. Considering that a normal adult has between 12 to 18 breathing events per minute, with this snoring signal size we will be analyzing the equivalent to $30 - 45\%$ of a breathing event.

These signals were tested using a multiscale approach and with the intention of differentiating the complexity associated to each SAHS disease. We obtained the $\mathrm{MFE}_{1D}$ values for each snore of each subject. Afterwards, we conducted the mean of the 50 curves corresponding to the 50 snores, obtaining only one curve for each subject. In the end, we decided to represent the mean values of $\mathrm{MFE}_{1D}$ corresponding for each SAHS stage (including the group control and simple snoring group).

### 3.2.2 Dermoscopic images

$\mathrm{FuzEn}_{C2D}$ testing involved two different biomedical applications: a *Cutaneous Microcirculation study* and a *Melanoma study*. We will approach first the cuta-

neous microcirculation images and their ROI selection. Later on, we refer the ROI of dermoscopic images from a public database containing skin lesions, including melanoma.

#### 3.2.2.1 Cutaneous microcirculation study

In order to discriminate two different microcirculatory states, dermoscopic images were taken before (at rest) and after applying a warmed water bottle (heat) of nine volunteers (8 women and 1 man) with $36.5 \pm 11$ years. The dermoscopic systems uses a *Medicam 800 HD* with a resolution of $1920 \times 1080$ full HD and 2 mega pixels. The dermoscopic images were all taken 3 cm from the antecubital fossa in the left arm of each volunteer (see appendix A).

In figure 3.6, we show an example of one image at rest (figure 3.6 (a)) and one after applying heat (figure 3.6 (b)), for the same subject. The region of interest for each image was defined from the central point of the original image, with a size of $256 \times 256$ pixels.

In addition, in figure 3.7, we show a box plot with the mean values of each image at rest and after applying heat (vasodilation) for the nine subjects.

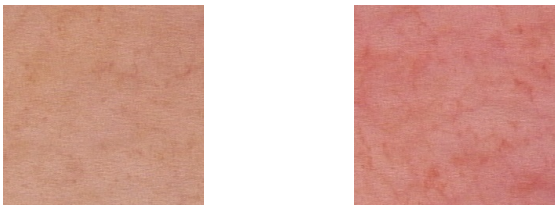

**(a)** Rest. **(b)** Vasodilation.

**Figure 3.6:** Dermoscopic images examples for two microcirculatory conditions, at rest and when vasodilation occurs, for the same subject, with a region of interest of $256 \times 256$ pixels.

Each dermoscopic image has been tested with *Haralick* features which are very common to evaluate an image's texture. The goal is to compare these descriptors with $\text{FuzEn}_{C2D}$ in terms of microcirculatory conditions discrimination. Based on previous studies [52, 55], we considered 6 *Haralick* features to extract information on each RGB channel ($\mathbf{U}_R$, $\mathbf{U}_G$ and $\mathbf{U}_B$) of the dermoscopic images tested and verify if they differentiate the two microcirculation states. The Haralick features used are shown in table 3.2.

Similarly to Silva *et al.* [52, 55] work to study $\text{SampEn}_{2D}$, we used four angles (0, 45, 90 and 135 degrees) to extract the co-occurrence matrices and ten inter pixel distances ($1 \leq D \leq 10$) to cover a variety of images. After obtaining the co-occurrence matrices for each descriptor, we calculated the mean value taking into account all matrices. For each channel, we obtain therefore, six descriptor values. We also performed a *Wilcoxon signed rank test* on the extracted features.

Moreover, the dermoscopic images have been tested using $\text{FuzEn}_{C2D}$. Afterwards, a *Wilcoxon signed rank test* has been performed to assess if there is statistical

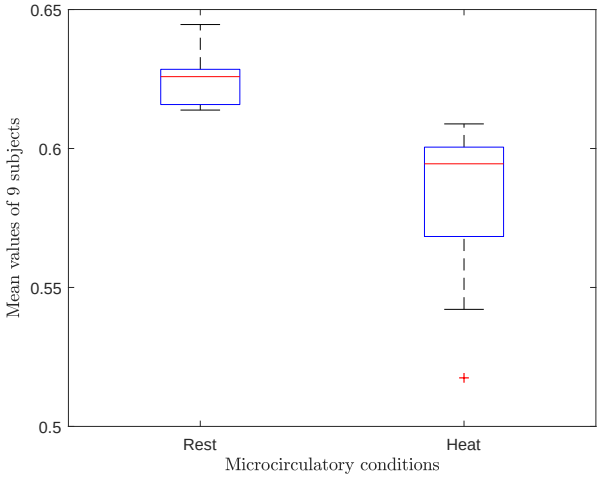


**Figure 3.7:** Mean values of the 9 tested subjects for the two microcirculatory conditions: at rest and after applying heat on skin (vasodilation).

**Table 3.2:** Haralick features used to evaluate the dermoscopic images of the cutaneous microcirculatory study, with *P(i,j)* being an estimation of the probability for each value in the co-occurrence matrix ($P(i,j) = \frac{g_{i,j}}{n}$; $g_{i,j}$- number of times that pixel (i,j) pairs with the intensity of $i$ and $j$ occur in the image $U$; $n$-sum of the elements of the co-occurrence matrix).

| Haralick Features | Definition |
|---|---|
| *Variance (contrast)* | $\sum_i \sum_j (i-j)^2 P(i,j)$ |
| *Entropy (suavity)* | $\sum_i \sum_j P(i,j) \log P(i,j)$ |
| *Uniformity (energy)* | $\sum_i \sum_j P(i,j)^2$ |
| *Homogeneity* | $\sum_i \sum_j P(i,j)/(1+\lvert i-j \rvert)$ |
| *3rd order moment (distortion)* | $\sum_i \sum_j (i-j)^3 P(i,j)$ |
| *Inverse variance* | $\sum_i \sum_j P(i,j)/(1-j)^2$ |

significance between the entropy values of the two microcirculation states: relaxed microcirculation (at rest) and for vasodilation (when heat is applied). Finally, we compared with the Haralick features results.

#### 3.2.2.2 Melanoma study

In order to test the ability of $\text{FuzEn}_{C2D}$ to detect and discriminate images containing melanoma skin lesions or not, we used a public melanoma database [79, 80]. This dataset contained the original dermoscopic images and the lesion segmentation as well as the diagnostic information about each patient.

These images were collected at the *Hospital Pedro Hispano*, Matosinhos, Portugal, using the same conditions and a *Tuebinger Mole Analyzer System*. The collected images have a size of $768 \times 520$ pixels. The database includes 200 dermoscopic images of melanocytic lesions: 80 common nevi, 80 atypical nevi and 40 melanoma [79, 80].

We represent in figure 3.8 the method used in this project for selecting the region of interest (ROI) of the dermoscopic images tested with $\text{FuzEn}_{C2D}$. Basically, with the original image and the segmented lesion, we exclude the skin region that does not contain any portion of the lesion and only test the rectangular area containing the defined lesion by Mendonca *et al.* [79]. Figure 3.8 shows an example of a final ROI for a certain dermoscopic image. These images, due to the ROI's selection procedure, do not necessarily have the same size between each other.

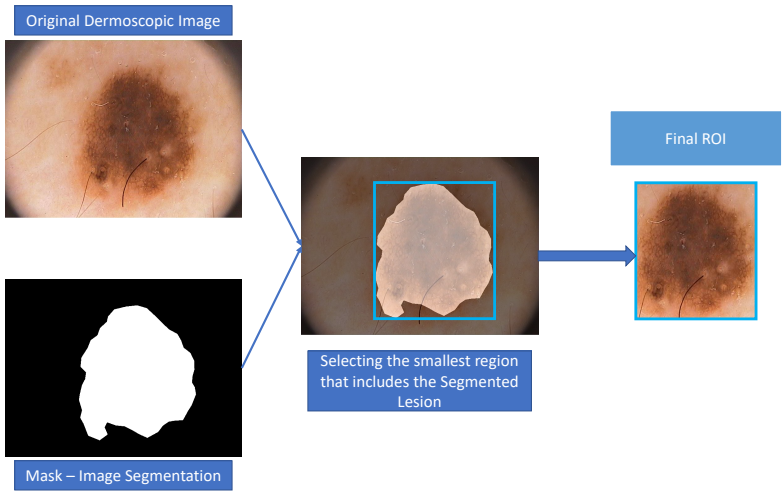


**Figure 3.8:** Schematic view of how the ROI was selected from the public melanoma database [79, 80] used.

It is relevant to mention that we are aware the ROI's can vary a lot in size. However, skin lesions are known for varying in size and shape. If we considered for example, a centered ROI with a specific size, probably some lesions would be completely included in that size or some not. Moreover, on the lesions that were not completely included, this could lead to the exclusion of relevant pixels that might reveal information about the lesion in study. Since by doing an entropy analysis we compare several pixels with each other this could be a problem.

### 3.2.3 Idiopathic pulmonary fibrosis disease study using CT scans

Herein we propose to apply an entropy measure to a tridimensional dataset. Consequently, knowing the advantages of fuzzy entropy, $\text{FuzEn}_{3D}$ has been developed to apply on volumetric CT scans to differentiate subjects suffering idiopathic pulmonary fibrosis from healthy individuals. Figure 3.9 show a CT scan example of a healthy individual (figure 3.9 (a)) and of a patient diagnosed with IPF (figure 3.9 (b)).

Each group, one with healthy individuals and another one with subjects suffering IPF, had 26 individuals so, we tested 52 volumes in total. The CT scans, composing the volumetric data, have been provided by University Hospital of Rennes.

Each subject has a certain number of scans ($N_z$) which can be different for each

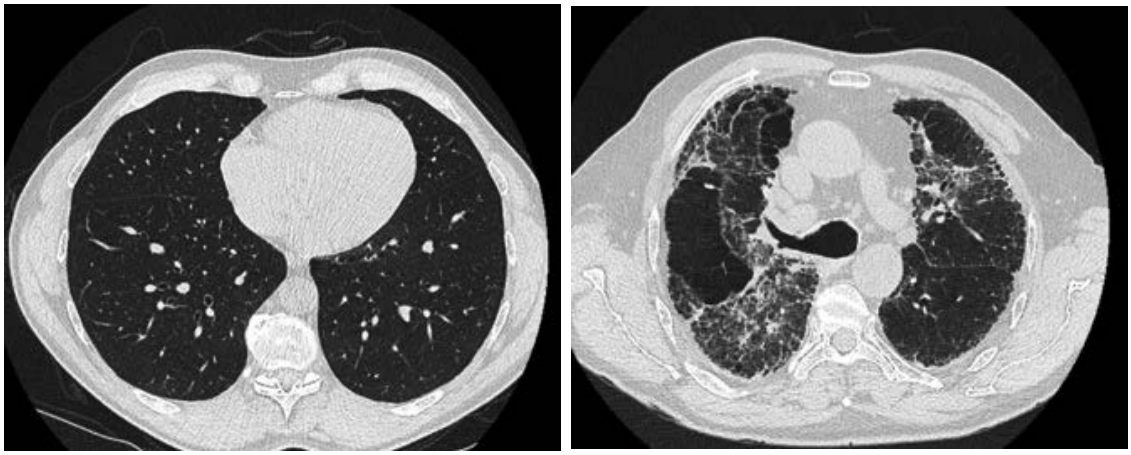

**(a)** Healthy subject. **(b)** IPF patient.

**Figure 3.9:** CT scan example of the tested dataset of a healthy individual and a patient diagnosed with IPF.

subject. However, each $xy$-slice has $512 \times 512$ points and in the end, the number of voxels is $512 \times 512 \times N_z$.

First, we proceeded to the lung's volume segmentation and selected, arbitrarily, the right lung. After that, we eliminated the exceeding zeros outside the lung's boundaries (non-relevant information). Since the individuals that suffer IPF are mostly affected in the basal and peripheral regions of the lung's [23, 25], our ROI selection depended on that.

The final data for each individual had $50 \times 50 \times 50$ voxels and has been extracted from the segmented volume of the right lung. The ROI was set to this size in order to have a relatively big portion of the lung, without compromising much the computational cost. In order to obtain this cube, the segmented volume was analysed, voxel-by-voxel, bottom up, from the most peripheral position to its central region, verifying if the cube having that voxel as a corner contained only 5% of zeros (see figure 3.10). This threshold was defined to avoid that the final volume contained a considerable portion from an exterior region to the lung's volume (non-relevant information).

In case of the condition being verified, we then obtain the most relevant cube in the most peripheral and basal region possible. Otherwise, we continue to go through the data to find the final data volume to be analyzed with $\text{FuzEn}_{3D}$.

Finally, we tested these 52 cubes of $50 \times 50 \times 50$ (26 from each group) with $\text{FuzEn}_{3D}$ and performed a *Wilcoxon rank sum test* (equivalent to the *Mann-Whitney U* test) or the *t-test*, according to normality assessment performed with *Shapiro-Wilk* test. This allowed to verify if statistical differences exist between the two sets of data. If statistical differences are found, this means that the algorithm has the ability to differentiate patients from healthy subjects.

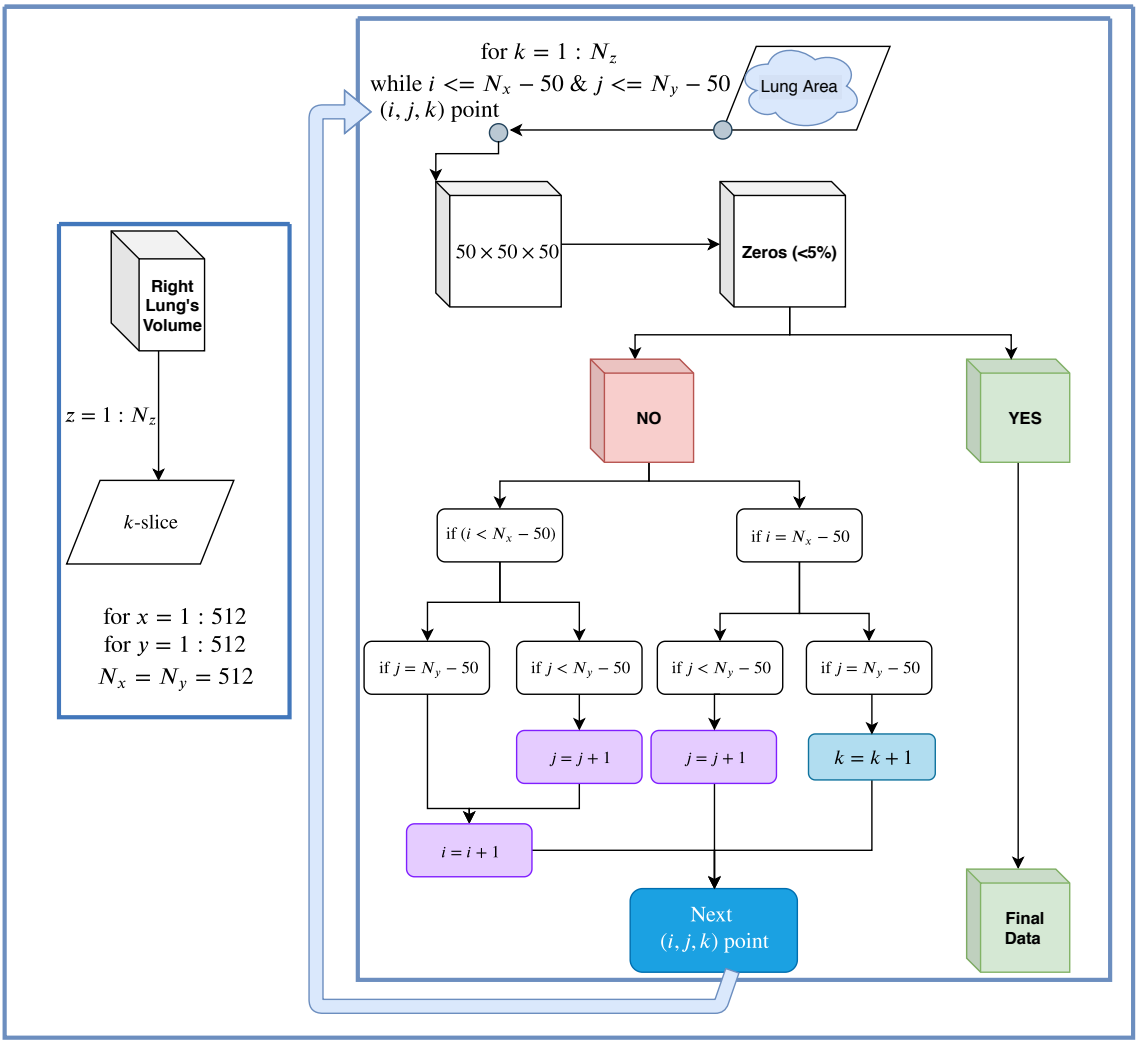


**Figure 3.10:** Schematic representation of CT scans ROI's selection for each subject.

# 4 Methods

This chapter presents the developed entropy algorithms based on fuzzy entropy during the master thesis project. These algorithms allowed the evaluation of entropy and complexity of the tested data. Mathematical expressions of sample entropy are also shown since it was used to compare with fuzzy entropy for one-dimensional signals on validation tests regarding sensitivity to parameters, multiscale analysis on noise signals, and length dependence of a signal to have defined entropy values for multiple scale factors.

## 4.1 One dimensional algorithms

This section is fully dedicated to one dimensional entropy algorithms namely sample entropy and fuzzy entropy, including multiscale versions.

### 4.1.1 Sample entropy and its multiscale version

#### 4.1.1.1 Sample entropy ($\mathbf{SampEn}_{1D}$)

Sample entropy ($\mathrm{SampEn}_{1D}$) [35] was proposed as an improvement from previous entropy measures, namely, approximate entropy [36], $\mathrm{ApEn}_{1D}$. The main focus was to obtain an unbiased entropy measure and remove the inconsistency usually associated to approximate measures [35].

$\mathrm{SampEn}_{1D}$ [35] is a method able to determine the existence of matching templates within the signal, excluding self-matches and reducing bias and inconsistency from previous measures [35, 37]. Furthermore, this entropy algorithm does not perform template-wise iterations and presents a reduced computational cost (compared to other measures) [35, 37].

Herein, having in mind the main characteristics, the mathematical expressions of sample entropy [35] are described.

Consider a signal, $u(i)$, of length $N$. A template, $x_m(i)$, is defined for $m$ points as it follows in equation (4.1) [35, 37]:

$$x_m(i) \;=\; u(i+k) \tag{4.1}$$

with $0 \leq k \leq m-1$, and $\;1 \leq i \leq N-m+1$.

The templates should be defined according to the length of the signal, $N$, i.e., if the templates have $m$-points (the embedding dimension of templates) then, the position $i$ must be $1 \leq i \leq N-m+1$ points, avoiding missing data. Moreover, templates of $[m+1]$-points, $x_{m+1}(i)$, are also considered with a similar definition to $x_m(i)$ but with $i$ not being higher than $N-m$ [35, 37].

Figure 4.1 represents how $m$-points templates are defined according to equation (4.1) and, also, how they are compared.

At the end, there will be $N-m+1$ $m$-points vectors as templates. The distance, $d$, between two vectors, $x_m(i)$ and $x_m(j)$ with $i \neq j$, is defined as the maximum absolute difference between the two (see equation (4.2)) [35, 37].

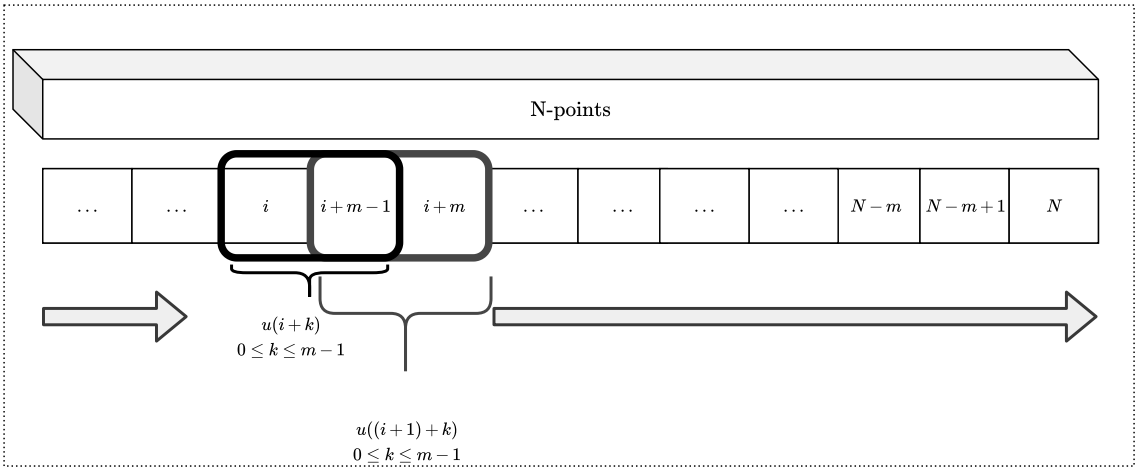


**Figure 4.1:** Definition of a $m$-points template $x_m(i)$ (black box) for a signal of $N$ points to be compared with a succeeding template (gray box), $x_m(i+1)$, considering $m = 2$ [35, 37].

$$d[x_m(i), x_m(j)] = \max(|x_m(i) - x_m(j)|) \tag{4.2}$$

The tolerance, $r$, is a threshold defined to determine when two template vectors are similar or not. Usually, $r$ is established as a percentage value of the signal's standard deviation [35]. According to that, the next step is to verify if the distance is within the tolerance, i.e, verifying the condition $d[x_m(i), x_m(j)] \leq r$ [35, 37] as a two state classifier (see equation (4.3)) [46].

$B_i(r)$ represents the number of templates' matches for $m$ points. Therefore, when $d[x_m(i), x_m(j)] \leq r$ is verified to true, then the templates are said to be similar, and one unity is added to $B_i(r)$ [35, 37].

$$\theta(i,j) = \begin{cases} 0 & \text{if } d[x_m(i), x_m(j)] > r \text{ (templates not similar)} \\ 1 & \text{if } d[x_m(i), x_m(j)] \leq r \text{ (similar templates)} \end{cases} \tag{4.3}$$

Similarly to $B_i(r)$, $A_i(r)$ corresponds to the number of vectors that matched each other for $m + 1$ points, considering the same definition of distance and $r$ value.

Consider $B_i^m(r)$ the probability of any $x_m(i)$ template being within $r$ of $x_m(j)$ (see equation (4.4)). In addition, for $m + 1$ points, $A_i^m(r)$ is considered as the probability of any $x_{m+1}(i)$ template being within $r$ of $x_{m+1}(j)$ (see equation (4.5)) [35].

$$B_i^m(r) = (N - m + 1)^{-1} \sum_{i=1}^{N-m} B_i(r) \tag{4.4}$$

$$A_i^m(r) = (N - m + 1)^{-1} \sum_{i=1}^{N-m} A_i(r) \tag{4.5}$$

Then, $B^m(r)$ can be described as the probability of matching two templates with $m$ points and $A^m(r)$ the probability of matching two templates, for $m + 1$ points [35] (see equations (4.6) and (4.7)).

$$B^m(r) = (N-m)^{-1} \sum_{i=1}^{N-m} B_i^m(r) \tag{4.6}$$

$$A^m(r) = (N-m)^{-1} \sum_{i=1}^{N-m} A_i^m(r) \tag{4.7}$$

Sample entropy [35], $SampEn(m, r, N)$ , can now be defined by equation (4.8):

$$SampEn(m, r, u) = -\ln \frac{A^m(r)}{B^m(r)} \tag{4.8}$$

for $m$ points as the embedding dimension, an established tolerance value $r$ as a percentage of the signal's SD.

#### 4.1.1.2 Multiscale sample entropy ($\mathbf{MSE}_{1D}$)

Costa *et al.* [39, 43] suggested a multiple scale entropy analysis to obtain additional and important information compared to the classical method that only considers a single scale.

This approach involves applying a *coarse-graining* procedure that down-samples the original signal $x$ of $N$ points into several smaller signals, $y^\tau$, according to the scale factor, $\tau$. The coarse-graining procedure can be defined as it follows in (4.9) [39, 43]:

$$y_j{}^{(\tau)} = \frac{1}{\tau} \sum_{i=(j-1)\tau+1}^{j\tau} x_i,\ 1 \leq j \leq \frac{N}{\tau} \tag{4.9}$$

Figure 4.2 shows an example of a coarse-grained series for $\tau = 2$ and $\tau = 3$ for a signal with $N$-points.

For $\mathrm{MSE}_{1D}$ [39, 43], each coarse-grained series of length $N/\tau$ leads to an entropy value given by $\mathrm{SampEn}_{1D}$ [35]. Finally, these entropy values are usually represented as a function of the scale factors. A scheme of how the multiscale analysis works is shown in figure 4.3.

This type of multiscale analysis can be very useful and does not depend on the entropy measure. The entropy can be assessed by other entropy measures like fuzzy entropy as it will be explained hereafter.

### 4.1.2 Fuzzy entropy and its multiscale version

#### 4.1.2.1 Fuzzy entropy ($\mathbf{FuzEn}_{1D}$)

Both $\mathrm{ApEn}_{1D}$ [36] and $\mathrm{SampEn}_{1D}$ [35] algorithms use the *Heaviside* function, classifying the distance in two states (see the section 4.1.1.1). One of the fuzzy entropy algorithm's great advantages is the use of a continuous function [45, 46].

According to Chen *et al.* [46], when considering the *Heaviside* function the points in question are treated equally when inside the considered boundary established by the tolerance value ($d[x_m(i), x_m(j)] \leq r$). The parameter $r$ will strongly influence the Heaviside function contribution [46].

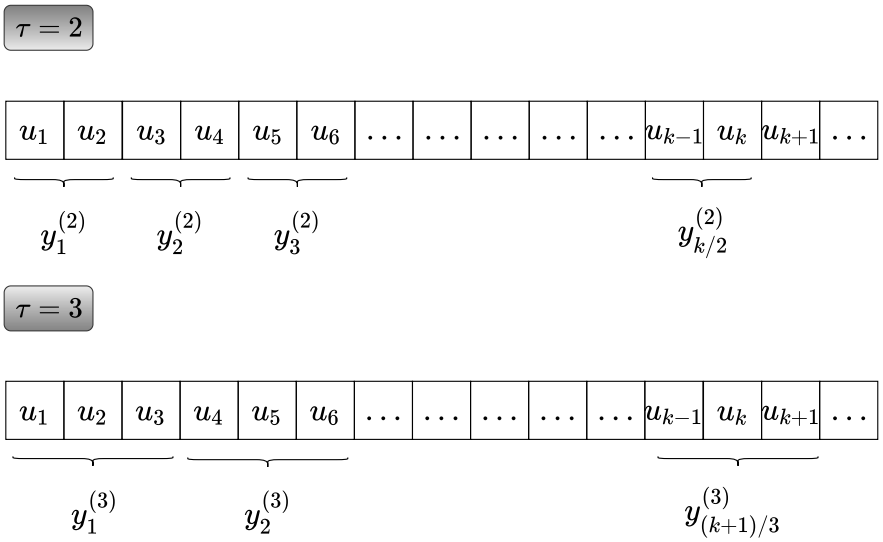


**Figure 4.2:** Representation of the coarse-graining procedure, considering the scale factors $\tau = 2$, and $\tau = 3$. Adapted from [64].

Fuzzy entropy (FuzzyEn$_{1D}$ [1]) [45, 46] uses the concept of Zadeh [68].

Based on the concept of Chen *et al.* [45, 46], an alternative definition of a fuzzy entropy measure, FuzEn$_{1D}$ is proposed.

Fuzzy entropy has the ability to measure the similarity degree between two template vectors. The fuzzy function, $\mu$, is responsible to measure that similarity and is represented in equation (4.10):

$$\mu \;=\; \exp(-(d_{ij}/r)^n) \tag{4.10}$$

being $d_{ij}$ the distance of two templates $i$ and $j$, i.e., $x_m(i)$ and $x_m(ij)$, $n$ is the exponential boundary gradient or fuzzy power and $r$ the tolerance value. The chosen fuzzy function, $\mu$, must be continuous (avoiding abrupt changes in similarities) and convex (the self-similarity is maximum), and in this case is an exponential function [46].

This function was also chosen by Chen *et al.* [45, 46] owing to the fact that it is well understood and shows a good performance as "fuzzy membership function".

Henceforth, *fuzzy entropy* is described, including the difference between FuzzyEn$_{1D}$ [45, 46] and FuzEn$_{1D}$.

Considering a time series $u(i)$ of length N ($1 \leqslant i \leqslant N$), for an embedding dimension $m$, the templates $x^m(i)$ and $x^{m+1}(i)$ are defined by equations (4.11) and (4.12) [45, 46]. Note that the first expression is equivalent to equation 4.1.

$$x_i^m = \{u(i), u(i+1), ..., u(i+m-1)\} \tag{4.11}$$

[1] FuzzyEn$_{1D}$ is the notation adopted for Chen *et al.* [45, 46] definition and FuzEn$_{1D}$is used for the proposed algorithm in this project.

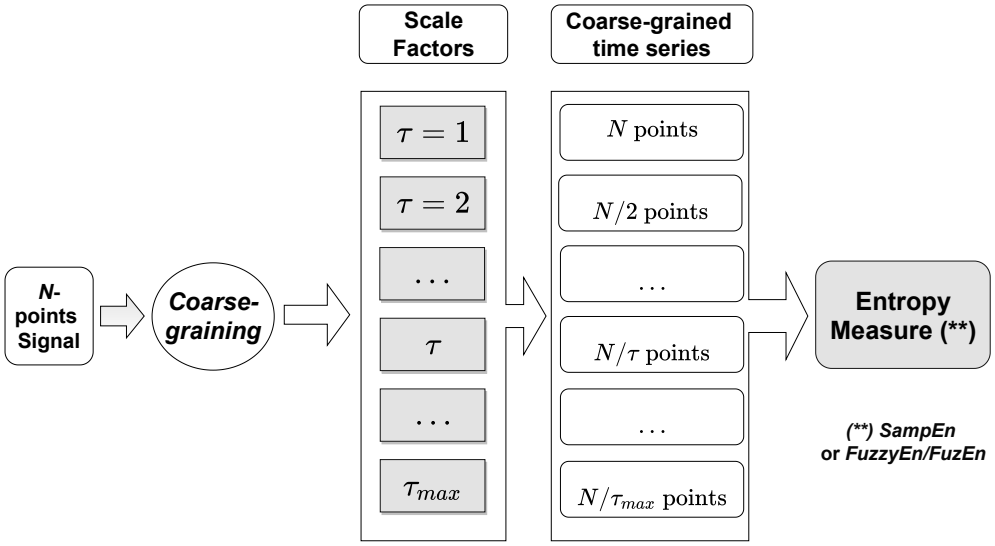


**Figure 4.3:** Representation of the basic steps through multiscale entropy measure algorithms.

$$x_i^{m+1} = \{u(i), u(i+1), ..., u(i+m)\} \tag{4.12}$$

The original FuzzyEn$_{1D}$ [45, 46] algorithm considered the removal of a baseline vector (see equation 4.13), i.e., a local mean from the data represented by equation 4.14.

$$u_0(i) = \frac{1}{m} \sum_{k=0}^{m-1} u(i+k) \tag{4.13}$$

$$x_i^m = \{u(i), u(i+1), ..., u(i+m-1)\} - u_0(i) \tag{4.14}$$

By removing the baseline vector the algorithm only considers local characteristics and it is relevant to consider both local and global characteristics [44, 58].

Liu *et al.* [44] defined, besides the local entropy (equivalent to the fuzzy entropy of Chen *et al.* [45, 46]), a global entropy. The global entropy considers templates similar to the ones represented by equation (4.14) but, instead of removing the signal's local mean, the authors removed the global mean. The final entropy value is the sum of the local and global entropy values [44].

On the other hand, Hilal *et al.* [58] introduced another approach for fuzzy entropy. The templates were defined similar to the definition represented in equation (4.11) however, applied to bidimensional data. The authors did not remove any type of mean values in order to consider both local and global characteristics [58].

SampEn$_{1D}$ [35] and ApEn$_{1D}$ [36] also included the global and local characteristics of the signal in question. Therefore, figure 4.1 can represent the template's definition

for $\text{SampEn}_{1D}$, and also for $\text{FuzEn}_{1D}$'s templates. The mathematical definition is shown in equation (4.11). Consequently, the only difference between $\text{FuzzyEn}_{1D}$ [45, 46] and $\text{FuzEn}_{1D}$ is simply having the local mean removal or not.

Once we define the templates, the similarity degree is also defined, in equation (4.15), based on the template's distance, i.e., maximum difference of the templates, $d_{ij} = \max(\left|x_i^m - x_j^m\right|)$ with $i \neq j$ [45, 46].

$$D_{ij}^m = \mu(d_{ij}^m, r) = \exp(-(d_{ij}/r)^n) \tag{4.15}$$

Then, the similarity degree average is done for both $m$ points, equation 4.16, and $m+1$ points, equation 4.17, considering $i \neq j$ [45, 46]:

$$\phi_i^m(n,r) = \frac{1}{N-m-1} \sum_{i=1,j=1}^{N-m} D_{ij}^m \tag{4.16}$$

$$\phi_i^{m+1}(n,r) = \frac{1}{N-m-1} \sum_{j=1}^{N-m} D_{ij}^{m+1} \tag{4.17}$$

Later on, the $\Phi^m(n,r)$ for $m$ points and $\Phi^{m+1}(n,r)$ for $m+1$ points are defined by equations 4.18 and 4.19, respectively, in order to calculate the entropy.

$$\Phi^m(n,r) = \frac{1}{N-m} \sum_{i=1}^{N-m} \phi_i^m(n,r) \tag{4.18}$$

$$\Phi^{m+1}(n,r) = \frac{1}{N-m} \sum_{i=1}^{N-m} \phi_i^{m+1}(n,r) \tag{4.19}$$

At last, $\text{FuzEn}_{1D}$ can be defined as the natural logarithm of the $\Phi^m(n,r)$ and $\Phi^{m+1}(n,r)$ ratio as represented by equation 4.20 [45, 46].

$$FuzEn_{1D}(m,n,r,u) \;=\; \ln \frac{\Phi^m(n,r)}{\Phi^{m+1}(n,r)} \tag{4.20}$$

In figure 4.4, the main characteristics of the two entropy algorithms described in this section are summarized. Regarding fuzzy entropy, the main advantages over sample entropy are the absence of undefined values, consistency, flexible parameter selection, and similarity degree measure [45, 46].

#### 4.1.2.2 Multiscale fuzzy entropy ($\text{MFE}_{1D}$)

The multiscale coarse-graining procedure is the same as the one mentioned in section 4.1.1.2 and defined by equation (4.9). The coarse-grained series are obtained with size of $\frac{N}{\tau}$ for an original signal of length $N$. These down-sampled versions of the original signal are constituted by averaged values.

According to the schematic of figure 4.3, after applying the coarse-graining procedure of equation 4.9, the entropy of each coarse-grained signal is determined by using an entropy measure, in this case $\text{FuzEn}_{1D}$. At the end, the only difference between $\text{MSE}_{1D}$ and $\text{MFE}_{1D}$ is the entropy measure chosen.

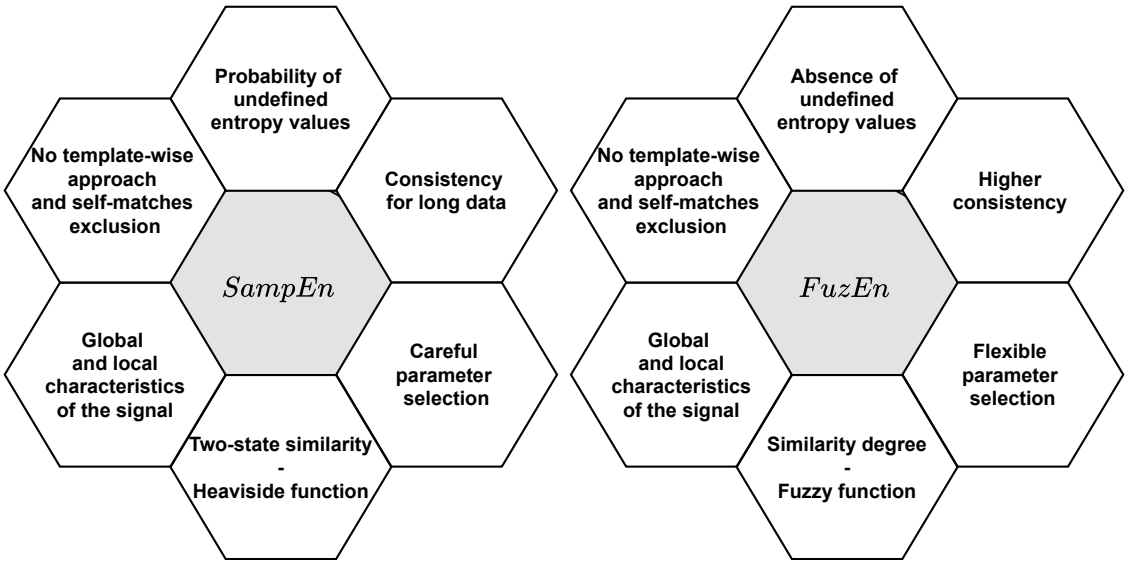


**(a)** $\text{SampEn}_{1D}$ [35]. **(b)** $\text{FuzEn}_{1D}$.

**Figure 4.4:** Sample entropy, $\text{SampEn}_{1D}$ [35], and fuzzy entropy, $\text{FuzEn}_{1D}$, main characteristics.

Through the coarse-graining technique developed by Costa *et al.* [39, 43], multiscale time series analysis allow us to have efficient and goal-motivated tests on signals:

- Determine the difference between a patient's $\text{MFE}_{1D}$ curve from an healthy subject one. Hence, identifying the disease's curve behavior.
- Assessing the pathology's stage through a complexity study. For example, the biologic aging process is being associated with loss of complexity on some signals, resulting in a decrease of entropy.

## 4.2 Bidimensional algorithms

This project involves the development of a new colored-based bidimensional entropy measure. First, the already existing gray-scaled version $\text{FuzEn}_{2D}$ [58, 73] is approached, and posteriorly, $\text{FuzEn}_{C2D}$ [75] is defined.

### 4.2.1 Bidimensional fuzzy entropy

#### 4.2.1.1 Bidimensional fuzzy entropy ($\text{FuzEn}_{2D}$)

Fuzzy Entropy can also be used to determine the irregularity of an image. By taking advantage of fuzzy entropy's characteristics, the bidimensional version will also show consistency, a more flexible selection of parameters, and others features (please see figure 4.4 (b)) [45, 46].

In section 4.1.2.1, it is referred that the chosen fuzzy function is able to measure the similarity degree trough an exponential function, $\exp(-(d_{ij}/r)^n))$, with $d_{ij}$ being

the distance between two templates $i$ and $j$, $r$ is the tolerance, and $n$ is the fuzzy power [46].

Consider an image $\mathbf{U}(i,j)$ for $1 \leqslant i \leqslant H$ and $1 \leqslant j \leqslant W$, with $H$ being the height and $W$ the width of $\mathbf{U}$ [58, 73].

Since bidimensional data is being considered, the templates will no longer be vectors. The templates are now defined as squared-windows. A template of $[m] \times [m]$ pixels, $X_{i,j}^{m}$, is defined by equation (4.21). For $[m+1] \times [m+1]$ pixels, the template $X_{i,j}^{m+1}$ is defined by equation (4.22). The total number of squared-windows will be $N_m = (W-m)(H-m)$, for $m$ and $m+1$ points [58, 73].

Figure 4.5 shows an example of a comparison between two templates, $X_{i,j}^{m}$ and $X_{a,b}^{m}$, considering an embedding dimension of $m = 2$. Moreover, it also shows a comparison between $X_{i,j}^{m+1}$ and $X_{a,b}^{m+1}$, for $m+1$-points, i.e., $m = 3$.

As mentioned in section 4.1.2.1, original fuzzy entropy definition included a baseline removal (local mean extraction). However, due to literature recommendations [44, 58, 73], in this bidimensional definition of fuzzy entropy, it was decided to account for local and global characteristics, as it has been done for the unidimensional definition.

$$X_{i,j}^{m} = \begin{bmatrix} \mathrm{U}_{i,j} & \cdots & \mathrm{U}_{i,j+m-1} \\ \mathrm{U}_{i+1,j} & \cdots & \mathrm{U}_{i+1,j+m-1} \\ \cdots & \cdots & \cdots \\ \mathrm{U}_{i+m-1,j} & \cdots & \mathrm{U}_{i+m-1,j+m-1} \end{bmatrix} \tag{4.21}$$

$$X_{i,j}^{m+1} = \begin{bmatrix} \mathrm{U}_{i,j} & \cdots & \mathrm{U}_{i,j+m} \\ \mathrm{U}_{i+1,j} & \cdots & \mathrm{U}_{i+1,j+m} \\ \cdots & \cdots & \cdots \\ \mathrm{U}_{i+m,j} & \cdots & \mathrm{U}_{i+m,j+m} \end{bmatrix} \tag{4.22}$$

Each $X_{i,j}^{m}$ squared window can be compared with the succeeding windows, $X_{a,b}^{m}$, excluding previous template comparisons (absence of template-wise approach), and self-matches ($(i,j) \neq (a,b)$). The same happens for $[m+1] \times [m+1]$ pixels [58, 73].

The similarity degree for $[m] \times [m]$ pixels is defined in equation (4.23) [58, 73] and depends on the distance between templates, $d_{ij,ab}^{m} = d[X_{i,j}^{m}, X_{a,b}^{m}]$, and on the tolerance value, $r$. In addition, it also depends on the fuzzy function, $\mu$, that should be continuous (avoid abrupt similarity changes) and convex (self-similarity is maximum) [46].

The value $r$ is commonly established as a percentage of the signal's SD [35] and represents the threshold level [58].

$$D_{ij,ab}^{m} = \mu(d_{ij,ab}^{m}, n, r) = \exp(-(d_{ij,ab}^{m})^{n}/r) \tag{4.23}$$

with $d_{ij,ab}^{m}$ being distance between the templates $X_{i,j}^{m}$ and $X_{a,b}^{m}$ (for $i \neq a$ and $j \neq b$), i.e., the maximum difference of the templates, $d_{ij,ab}^{m} = d[X_{i,j}^{m}, X_{a,b}^{m}] = max(|u(i+s, j+t) - u(a+s, b+t)|)$ with $(i,j) \neq (a,b)$ and $s,t \in (0, m-1)$. According to this, the exponential function boundary will be determined by both the tolerance and fuzzy power [58, 73].

Then, the similarity degree is averaged, for $(i,j) \neq (a,b)$ [58, 73]:

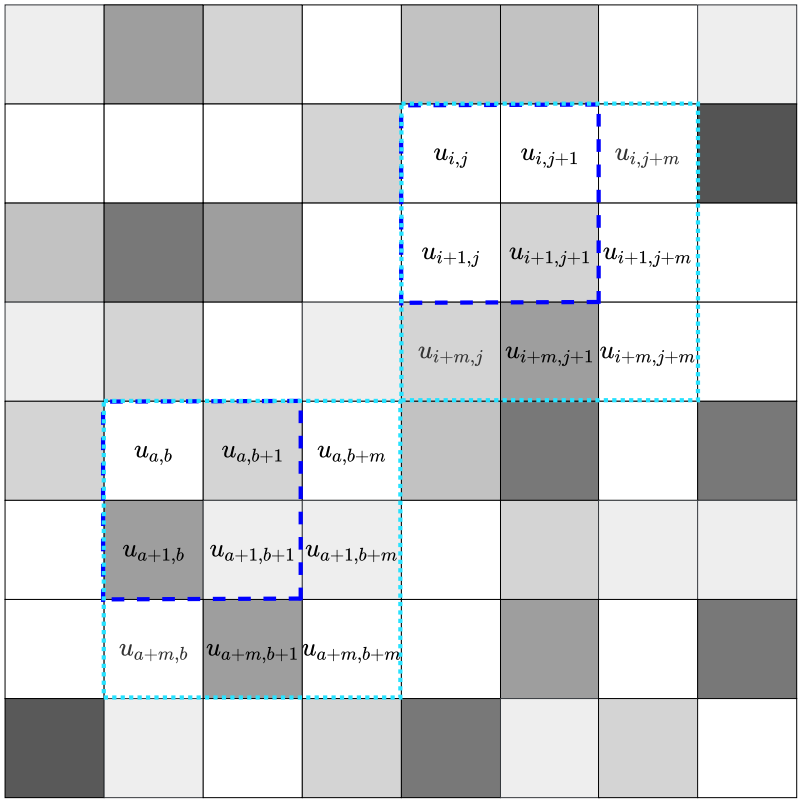


**Figure 4.5:** Scheme of an image **U**, representing an example of comparison between the $[m] \times [m]$ squared templates $X_{i,j}^{m}$ and $X_{a,b}^{m}$ (dark blue dashed line) and the $[m+1] \times [m+1]$ squared templates $X_{i,j}^{m+1}$ and $X_{a,b}^{m+1}$ (light blue dashed line), in this case considering an embedding dimension of $m = 2$. Adapted from [52].

$$\phi_{i,j}^{m}(n,r) = \frac{1}{N_m - 1} \sum_{a=1,b=1}^{a=H-m,b=W-m} D_{ij,ab}^{m} \tag{4.24}$$

Similarly, for $m+1$ points, the average similarity degree is:

$$\phi_{i,j}^{m+1}(n,r) = \frac{1}{N_m - 1} \sum_{a=1,b=1}^{a=H-m,b=W-m} D_{ij,ab}^{m+1} \tag{4.25}$$

with $(i,j) \neq (a,b)$ to exclude self-matches.

Afterwards, the $\Phi$ for $[m] \times [m]$ pixels and $[m] \times [m]$ pixels is defined in order to calculate the entropy, shown in equations (4.26) and (4.27) [58, 73].

$$\Phi_{i,j}^{m}(n,r) = \frac{1}{N_m} \sum_{i=1,j=1}^{i=H-m,j=W-m} \phi_{i,j}^{m}(n,r) \tag{4.26}$$

$$\Phi_{i,j}^{m+1}(n,r) = \frac{1}{N_m} \sum_{i=1,j=1}^{i=H-m,j=W-m} \phi_{i,j}^{m+1}(n,r) \tag{4.27}$$

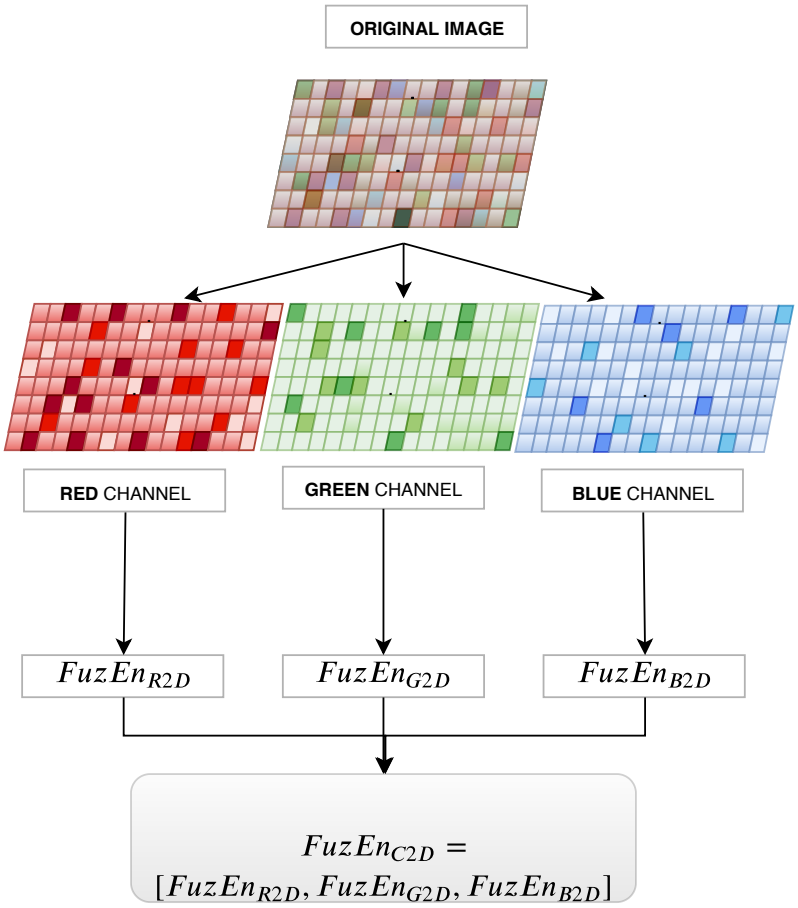


**Figure 4.6:** $\text{FuzEn}_{C2D}$ analysis representation showing the color division of the original colored image.

At last, $\text{FuzzyEn}_{1D}$ can be defined as the natural logarithm of the $\Phi^m_{i,j}(n,r)$ and $\Phi^{m+1}_{i,j}(n,r)$ ratio (equation (4.28)) [58].

$$FuzEn_{2D}(m,n,r,u) = \ln \frac{\Phi^m_{i,j}(n,r)}{\Phi^{m+1}_{i,j}(n,r)} \tag{4.28}$$

#### 4.2.1.2 Bidimensional colored fuzzy entropy ($\text{FuzEn}_{C2D}$)

Since the goal was to analyze the colored versions of dermoscopic images, the previous algorithm suffered some modifications and resulted in $\text{FuzEn}_{C2D}$ definition. Colored images have 3 color channels: red (R), green (G) and blue (B). Each channel is analyzed separately hence, the difference between $\text{FuzEn}_{C2D}$ and Santos *et al.* [74] entropy definition (see figure 4.6).

Consider an image $\mathbf{U}$ decomposed in its 3 corresponding RGB (Red, R, Green, G, and Blue, B) channels, $\mathbf{U_R}$, $\mathbf{U_G}$, and $\mathbf{U_B}$, respectively. Once more, the templates will be squared-windows. For each channel, considering $m$ as the template's embedding dimension, there will be $N_m = (H-m)(W-m)$ squared windows. The templates, $X^m_{i,j,K}$, are defined as in equation (4.29), considering the channels $K = R, G, B$. Similarly, the definition for $[m+1] \times [m+1]$ pixels is equivalent [75].

$$X^m_{i,j,K} = \begin{bmatrix} \mathrm{U}_{i,j,K} & \cdots & \mathrm{U}_{i,j+m-1,K} \\ \mathrm{U}_{i+1,j,K} & \cdots & \mathrm{U}_{i+1,j+m-1,K} \\ \cdots & \cdots & \cdots \\ \mathrm{U}_{i+m-1,j,K} & \cdots & \mathrm{U}_{i+m-1,j+m-1,K} \end{bmatrix} \tag{4.29}$$

for $1 \leq i \leq H - m$ and $1 \leq j \leq W - m$, $H$ being the image's height, and $W$ its width [75].

Afterwards, the similarity degree is calculated as demonstrated previously, shown in equation (4.30). The distance, $d^m_{ij,ab,K}$, for a $K$ channel and a squared $[m] \times [m]$ template is defined as the maximum difference of the templates: $d^m_{ij,ab,K} = d[X^m_{i,j,K}, X^m_{a,b,K}] = max(|\mathrm{U}_K(i+s, j+t) - \mathrm{U}_K(a+s, b+t)|)$, with $(i,j) \neq (a,b)$, and $s, t \in (0, m-1)$ [75].

$$D^m_{ij,ab,K} = \mu(d^m_{ij,ab,K}, n, r) = \exp(-(d^m_{ij,ab,K})^n / r) \tag{4.30}$$

with $d^m_{ij,ab,K}$ being the distance, $n$ is the fuzzy power, and finally, $r$ is the tolerance value [75].

The similarity degree is then averaged [75]:

$$\phi^m_{i,j,K}(n,r) = \frac{1}{N_m - 1} \sum_{a=1,b=1}^{a=H-m,b=W-m} D^m_{ij,ab,K} \tag{4.31}$$

with $(i,j) \neq (a,b)$. Similarly, for $m+1$ points, the average similarity degree is:

$$\phi^{m+1}_{i,j,K}(n,r) = \frac{1}{N_m - 1} \sum_{a=1,b=1}^{a=H-m,b=W-m} D^{m+1}_{ij,ab,K} \tag{4.32}$$

As a result, it is obtained [75]:

$$\Phi^m_{i,j,K}(n,r) = \frac{1}{N_m} \sum_{i=1,j=1}^{i=H-m,j=W-m} \phi^m_{i,j,K}(n,r) \tag{4.33}$$

$$\Phi^{m+1}_{i,j,K}(n,r) = \frac{1}{N_m} \sum_{i=1,j=1}^{i=H-m,j=W-m} \phi^{m+1}_{i,j,K}(n,r) \tag{4.34}$$

The colored bidimensional fuzzy entropy can now be defined for each channel like in equations (4.35), (4.36), and (4.37) [75].

$$FuzEn_{R2D}(m,n,r,u_R) = \ln \frac{\Phi^m_{i,j,R}(n,r)}{\Phi^{m+1}_{i,j,R}(n,r)} \tag{4.35}$$

$$FuzEn_{R2D}(m,n,r,u_G) = \ln \frac{\Phi^m_{i,j,G}(n,r)}{\Phi^{m+1}_{i,j,G}(n,r)} \tag{4.36}$$

$$FuzEn_{R2D}(m,n,r,u_B) = \ln \frac{\Phi^m_{i,j,B}(n,r)}{\Phi^{m+1}_{i,j,B}(n,r)} \tag{4.37}$$

The final entropy is presented as having 3 values, one for each RGB channel, as represented in equation (4.38) [75].

$$FuzEn_{C2D}(m, n, r, u) = [FuzEn_{R2D}, FuzEn_{G2D}, FuzEn_{B2D}]; \tag{4.38}$$

In a biomedical point of view, this technique can be used to identify different structures on biomedical images, having the advantage of no longer discarding colors.The main goal is to reveal new information. This can be used to identify and quantify different skin and microcirculatory conditions.

## 4.3 Tridimensional algorithm

The following sections are dedicated to a tridimensional version of $\text{FuzEn}_{1D}$ and its multiscale version, having in mind 3D applications.

### 4.3.1 Tridimensional fuzzy entropy and multiscale version

First, it is approached the fuzzy entropy 3D, $\text{FuzEn}_{3D}$, definition and afterwards, the multiscale version.

#### 4.3.1.1 Tridimensional fuzzy entropy ($\text{FuzEn}_{3D}$)

$\text{FuzEn}_{3D}$ is an adaption of the proposed original $\text{FuzEn}_{1D}$ and therefore, the approach to obtain the entropy is similar but with a tri-dimensional extension. Consider a volume $\boldsymbol{U}(i, j, k)$ of dimensions $W \times L \times H$ (W-width, L-length, H-height), for $1 \leq i \leq W$, $1 \leq j \leq L$, and $1 \leq k \leq H$.

Firstly, the cuboid templates are defined, extending the squared-windows into cubes. The cuboid template is composed by a group of voxels from the volume $\boldsymbol{U}$. A tri-dimensional template, $X^m_{i,j,k}$, with origin at a point $(i, j, k)$, can be defined by equation (4.39), with an edge of $m$ voxels.

The parameter $m$ is the embedding dimension of the template. Since the template is a cube, the dimensions of it are $[m \times m \times m]$ voxels.

Similarly, we define $X^{m+1}_{i,j,k}$, a tri-dimensional template of $[m+1] \times [m+1] \times [m+1]$ voxels. In the end, it is obtained a total number of cuboid templates $N_m = (W - m)(H - m)(L - m)$, that can be generated for $m$ and $m + 1$ size.

$$X^m_{i,j,k} = \begin{bmatrix} U_{i,j,k} & \cdots & U_{i,j+m-1,k} \\ U_{i+1,j,k} & \cdots & U_{i+1,j+m-1,k} \\ \cdots & \cdots & \cdots \\ U_{i+m-1,j,k} & \cdots & U_{i+m-1,j+m-1,k} \end{bmatrix} \begin{bmatrix} U_{i,j,k+m-1} & \cdots & U_{i,j+m-1,k+m-1} \\ U_{i+1,j,k+m-1} & \cdots & U_{i+1,j+m-1,k+m-1} \\ \cdots & \cdots & \cdots \\ U_{i+m-1,j,k+m-1} & \cdots & U_{i+m-1,j+m-1,k+m-1} \end{bmatrix} \tag{4.39}$$

A template $X^m_{i,j,k}$ can be compared with their neighbors, $X^m_{a,b,c}$, for $1 \leq a \leq W-m$, $1 \leq b \leq L-m$ and $1 \leq c \leq H-m$, excluding previous template comparisons (absence of template-wise approach) and self-matches ($(i,j,k) \neq (a,b,c)$) (see an example for $m = 3$ in figure 4.7).

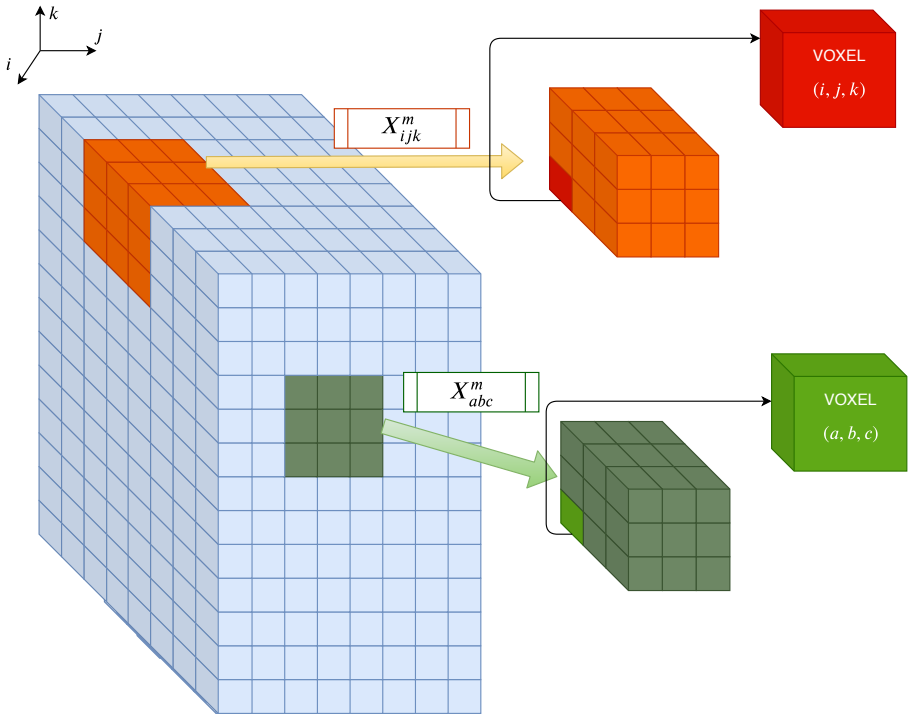


**Figure 4.7:** Representation of how two templates to be compared with each other, $X^m_{i,j,k}$ and $X^m_{a,b,c}$, are constituted from the voxels $(i,j,k)$ and $(a,b,c)$, respectively, considering $m = 3$.

Afterwards, the distance between two templates, $d^m_{ijk,abc}$, is obtained and defined as the maximum absolute difference of the templates $X^m_{i,j,k}$ and $X^m_{a,b,c}$ (see equation (4.40)).

$$d^m_{ijk,abc} = d[X^m_{i,j,k}, X^m_{a,b,c}] = \max(|U(i+s,j+t,k+q) - U(a+s,b+t,c+q)|) \quad (4.40)$$

for $(i,j,k) \neq (a,b,c)$ and $s,t,q \in (0, m-1)$.

After that, the similarity degree is defined for a $[m \times m \times m]$ sized cube, $D^m_{ijk,abc}$, considering the exponential fuzzy function, $\mu(d^m_{ijk,abc}, n, r)$ (continuous and convex [46]), in equation 4.41. The similarity degree depends on the fuzzy power, $n$, and in the tolerance value, $r$, a threshold level defined by a percentage of the data's SD.

$$D^m_{ijk,abc} = \mu(d^m_{ijk,abc}, n, r) = \exp(-(d^m_{ijk,abc})^n / r) \quad (4.41)$$

with for $(i,j,k) \neq (a,b,c)$.

Following that, the similarity degree average is done:

$$\phi^m_{i,j,k}(n,r) = \frac{1}{N_m - 1} \sum_{a=1,b=1,c=1}^{a=W-m,b=L-m,c=H-m} D^m_{ijk,abc} \quad (4.42)$$

Similarly, for $[m+1] \times [m+1] \times [m+1]$ sized template, the average similarity degree is:

$$\phi_{i,j,k}^{m+1}(n,r) = \frac{1}{N_m - 1} \sum_{a=1,b=1,c=1}^{a=W-m,b=L-m,c=H-m} D_{ijk,abc}^{m+1} \tag{4.43}$$

Afterwards, the $\Phi$ for $m$ and $m+1$ size are defined in equations (4.44) and (4.45), for $(i,j,k) \neq (a,b,c)$.

$$\Phi_{i,j,k}^{m}(n,r) = \frac{1}{N_m} \sum_{i=1,j=1,k=1}^{i=W-m,j=L-m,k=H-m} \phi_{i,j,k}^{m}(n,r) \tag{4.44}$$

$$\Phi_{i,j,k}^{m+1}(n,r) = \frac{1}{N_m} \sum_{i=1,j=1,k=1}^{i=W-m,j=L-m,k=H-m} \phi_{i,j,k}^{m+1}(n,r) \tag{4.45}$$

Finally, the $\text{FuzEn}_{3D}$ can be defined as the natural logarithm ratio between $\Phi_{i,j,k}^{m}(n,r)$ and $\Phi_{i,j,k}^{m+1}(n,r)$, represented in equation (4.46).

$$FuzEn_{3D}(m,n,r,u) \;=\; \ln \frac{\Phi_{i,j,k}^{m}(n,r)}{\Phi_{i,j,k}^{m+1}(n,r)} \tag{4.46}$$

#### 4.3.1.2 Multiscale fuzzy entropy 3D ($\text{MFE}_{3D}$)

The first step of tridimensional multiscale analysis involves applying the coarse-graining procedure, similar to the original multiscale definition (see equation (4.47)).

From the original volume, U, $\tau$ coarse-grained volumes are obtained, with $\tau$ being the scale factor. Each coarse-grained volume obtained, ${Y_{i,j,k}}^{(\tau)}$, has a size of $[\frac{W}{\tau} \times \frac{L}{\tau} \times \frac{H}{\tau}]$ and can be considered a down-sampled version of the original one. This ${Y_{i,j,k}}^{(\tau)}$ volume is constituted by averaged-values.

$${Y_{i,j,k}}^{(\tau)} = \frac{1}{\tau^3} \sum_{\substack{l=(i-1)\tau+1 \\ m=(j-1)\tau+1 \\ n=(k-1)\tau+1}}^{\substack{k\tau \\ j\tau \\ i\tau}} U_{l,m,n} \tag{4.47}$$

for $1 \leq i \leq \frac{W}{\tau}$, $1 \leq j \leq \frac{L}{\tau}$ and $1 \leq k \leq \frac{H}{\tau}$.

Following that, $\text{FuzEn}_{3D}$ is applied as the entropy measure chosen to determine the irregularity of the volume, on each coarse-grained volume obtained.

Figure 4.8 represents how the procedure in equation (4.47) works. It shows an example how the volume's first voxels are averaged for a $\tau = 2$. As represented, $Y_{1,1,1}^{(\tau)}$ and $Y_{1,2,1}^{(\tau)}$ will be the first two elements of the coarse-grained volume for $\tau = 2$, which has $\frac{W}{2} \times \frac{L}{2} \times \frac{H}{2}$ voxels.

Finally, each $\tau$-volume has an associated fuzzy entropy values and therefore, obtaining a curve of entropic values as function of $\tau$. Every step can be easily compared with the unidimensional version since this definition is an extension of the original one.

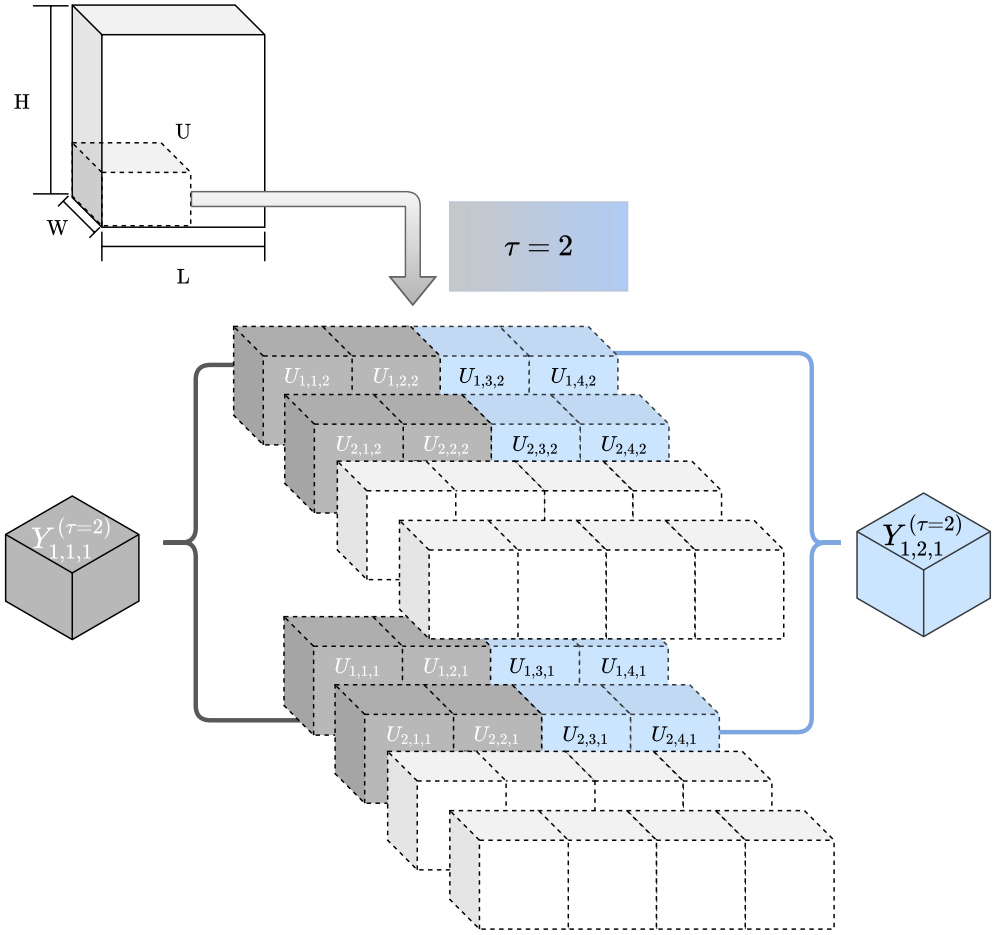


**Figure 4.8:** Representation of the multiscale procedure for the first voxels of a certain volume $U$, considering $\tau = 2$.

Since the analysis on volumetric data depends on this multiscale technique, the goals are similar to the ones mentioned in section 4.1.2.2. Firstly, it must be possible to differentiate a patient from a healthy subject using the $\text{MFE}_{3D}$ curves. Moreover, establishing the entropy behavior of the disease according to stage progression is of utmost interest.

# 5 Results and discussion

This chapter includes the tests performed in order to validate the algorithms for uni-, and multidimensional data. These validation tests are based on tests done previously in literature, and their results are discussed according to that. In addition, it also includes the results regarding the biomedical applications of $\text{FuzEn}_{1D}$, $\text{FuzEn}_{2D}$, and $\text{FuzEn}_{3D}$.

## 5.1 Unidimensional fuzzy entropy - $\text{FuzEn}_{1D}$

First, the several validation tests performed on $\text{FuzEn}_{1D}$ are approached. Earlier on, it was mentioned that the parameters fuzzy entropy depends on, namely: the fuzzy power, $n$, the tolerance, $r$, and the embedding dimension of the templates, $m$. According to that, it will be shown several tests demonstrating $\text{FuzEn}_{1D}$ behavior, including a multiscale analysis of noise signals. Afterwards, the biomedical application, signals of snoring events, is presented and discussed:.

### 5.1.1 Tolerance and fuzzy power variation

Thanks to Zadeh's [68] notion of fuzzy sets, Chen *et al.* [45, 46] proposed to measure the degree of a certain pattern belonging to a class. In theory, when the similarity degree, $D_{ij}$, is close to one, the membership for that class is high [45].

In figure 5.1, to introduce the first two parameters, the behavior of the fuzzy exponential function, $\mu = \exp(-d^n/r)$, is shown. One can observe the parameters influence on the similarity degree [1], $\mu$.

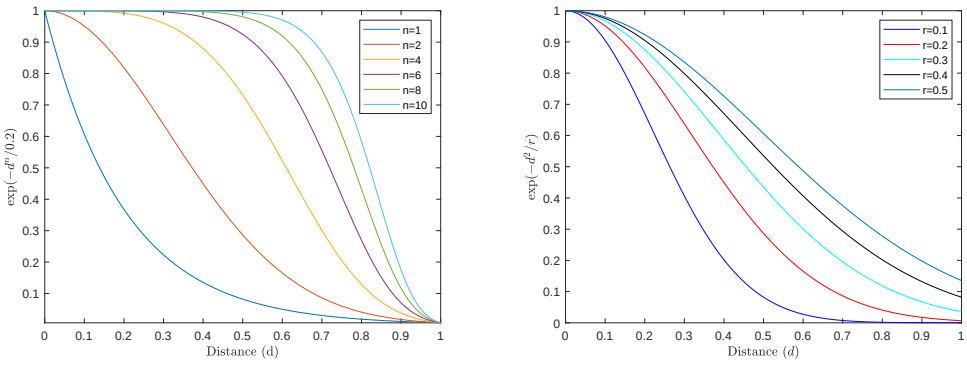


**(a)** $n$ variation, for $r = 0.2$. **(b)** $r$ variation, for $n = 2$.

**Figure 5.1:** Similarity values as function of the distance, $d$, varying the exponential boundary gradients (a) and tolerance values (b).

Based on the mentioned family of exponential functions, it is possible to obtain continuous values of the similarity degree (see figure 5.1). In figure 5.2, the Heaviside

[1] Since it is used the same exponential function for all three fuzzy entropy versions, $\text{FuzEn}_{1D}$, $\text{FuzEn}_{C2D}$, and $\text{FuzEn}_{3D}$, the influence of $r$ and $n$ is the same regarding the fuzzy function.

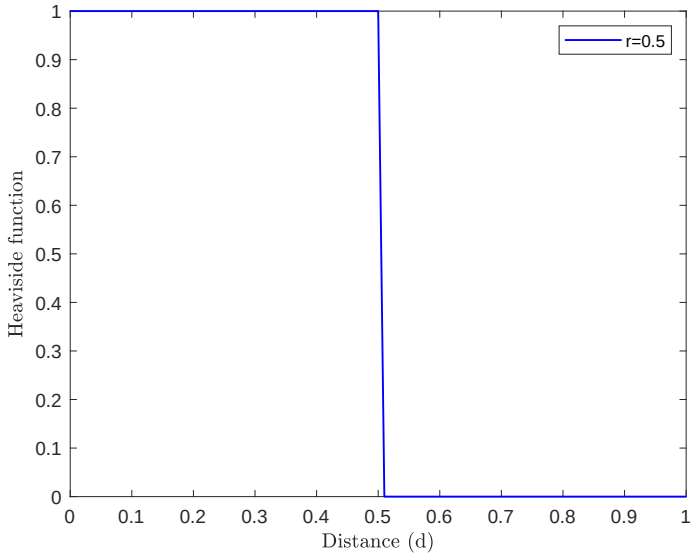


**Figure 5.2:** Heaviside function for a tolerance value of $r = 0.5$.

function clearly shows an abrupt similarity change due to the only two possible states. However, the exponential provides smoother changes in similarity and allows to define self-similarity condition as the maximum [45].

Nevertheless, by fixing the tolerance to $r = 0.2$, in figure 5.1 (a), and by fixing the fuzzy power to $n = 2$, in figure 5.1 (b), we observe as the $n$-value and the $r$-value increase, the similarity degree is less smooth. This means a more flexible parameter selection [45, 46] is possible with fuzzy function than with the Heaviside function, as expected. Regardless, choosing the parameters accordingly is still an important task.

According to Chen *et al.* [45, 46], the $n$-value must be a small integer value. When $n$ is lower than 1, distant templates are weighted instead of close ones. On the other hand, for large $n$-values information can be loss [45].

Hence, having in mind the previous considerations and cased on previous works [44–46, 57, 64], the parameter $n$ was established with the value $n = 2$. In figure 5.1 (a), it can be verified that for $n = 2$ (orange) the similarity degree has a smoother variation compared with higher $n$-values.

### 5.1.2 Tolerance and embedding dimension sensitivity

The tolerance value must be a constant value multiplied by standard deviation value of the data. According to this, the following test was performed on white noise signals with the goal of revealing the sensitivity to changes in tolerance, considering the variation of $0.06 \times SD_{data} \leq r \leq 0.48 \times SD_{data}$ with a step of 0.06 (see figure 5.3). In this test, the type of signal chosen is not relevant since the goal is evaluating the $\text{FuzEn}_{1D}$ behavior towards the change of $r$-values rather the entropy values.

For each tolerance value, in figure 5.3, the entropy was calculated on 10 white noise signals (see section 3.1.2.1) and the mean entropy value is displayed for each tolerance. Besides the change of tolerance values, the change of embedding dimension,

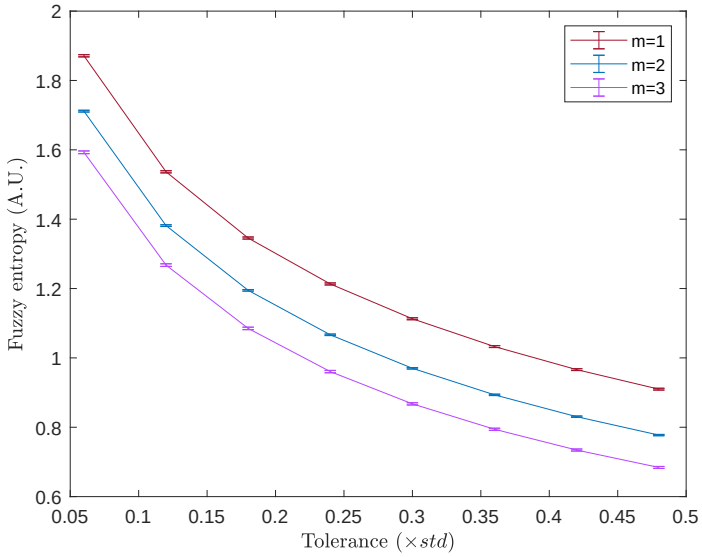


**Figure 5.3:** $\text{FuzEn}_{1D}$ sensitivity to change of tolerance, $r$, for $k \times SD_{data}$ with $0.06 \leq k \leq 0.48$ (step of 0.06), and different embedding dimension values, $1 \leq m \leq 3$, using white noise signals.

$m$, is also analysed to show behavior of the algorithm upon different parameters.

Comparing the 3 curves for $m = 1$ (red), $m = 2$ (blue) and $m = 3$ (purple), in figure 5.3, the behavior is very similar between each other, with the entropy dropping along with the increase of $r$ value. For a large tolerance value, the boundary becomes broad [45, 46], therefore, more patterns will have the same similarity degree value, and an information loss can be verified. This could explain this decrease.

#### 5.1.2.1 Fuzzy entropy *VS* sample entropy

In figure 5.4, we observe that fuzzy entropy is less sensitive to tolerance variation than sample entropy, as expected due to previous works [45, 46]. For this comparison, the entropy with $\text{SampEn}_{1D}$ [35] and $\text{FuzEn}_{1D}$ have been determined in the same ten white noise signals for 8 tolerance levels.

In figure 5.4, it can be verified how fuzzy entropy does not decrease so fast with the change of tolerance values as sample entropy does. Also, for smaller $r$-values, sample entropy is higher due to more strict matching criteria.

Even though $\text{FuzEn}_{1D}$ does not have so strict boundaries, an entropy rise for smaller $r$-values can be observed as well. However, these values are smaller compared to the ones obtained by $\text{SampEn}_{1D}$. These observations are in line with previous works [35, 44–46].

For $\text{FuzEn}_{1D}$, a change of 54.6% is verified between the entropy for the first $r$-value and the last, outstanding the 60.9% of $\text{SampEn}_{1D}$.

Regardless the smoother variation of $\text{FuzEn}_{1D}$, the goal is to define a fixed value multiplied by data's SD, as said before. Fixing this value for all tests, allows us to compare the results without having to consider possible fluctuations due to different tolerance values.

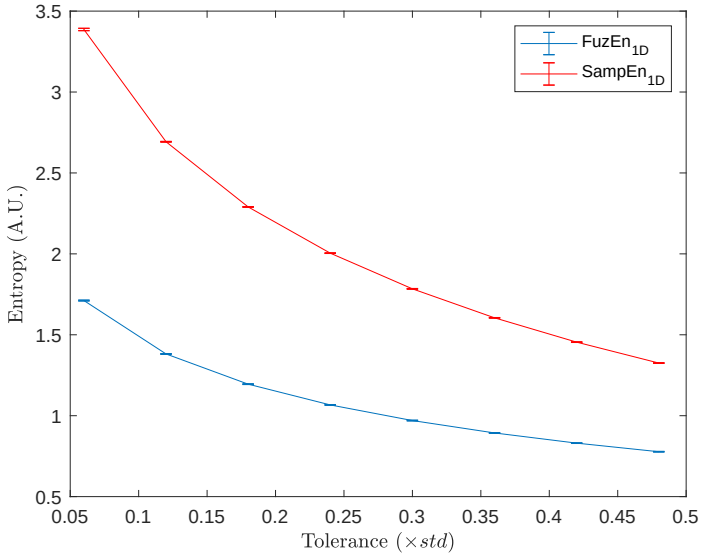


**Figure 5.4:** Sample (red) and fuzzy (blue) entropy sensitivity to change of tolerance, $r$, with $m = 2$, using white noise signals.

Since it is convenient to choose the entropy value between $0.10 \times SD_{data}$ and $0.25 \times SD_{data}$ [64], in the following validation tests and for the biomedical data as well, the chosen tolerance value was $r = 0.20 \times SD_{data}$.

### 5.1.3 $\text{MIX}_{1D}(p)$ processes and the embedding dimension behavior

As it can observed in figure 5.5, accordingly with the MIX($p$) processes definition, an increase on entropy with an increase of $p$-value (parametric probability) [36, 52] can also be verified. Moreover, a well-behaved curves for all $m$-values is observed.

In order to avoid a single-point comparison (when considering a template size of $m = 1$), the choice is towards the value $m = 2$. Choosing an higher value like $m = 3$, implies increasing the computational cost. Furthermore, the entropy value discrimination is similar for both $m$-values, according to figure 5.5.

Commonly, the $m$ parameter is set to $m = 2$ [35, 36, 39, 43, 45, 46, 57, 60, 64]. This allows us to have a results precise enough and with more information than just using $m = 1$ [57]. The table 5.1 shows parameters values chosen for the further validation tests and upcoming biomedical application.

**Table 5.1:** Parameters values chosen for upcoming tests of $\text{FuzEn}_{1D}$.

| ***Parameters*** | ***Chosen Values*** |
|---|---|
| $n$ | 2 |
| $m$ | 2 |
| $r$ | $0.2 \times SD_{data}$ |

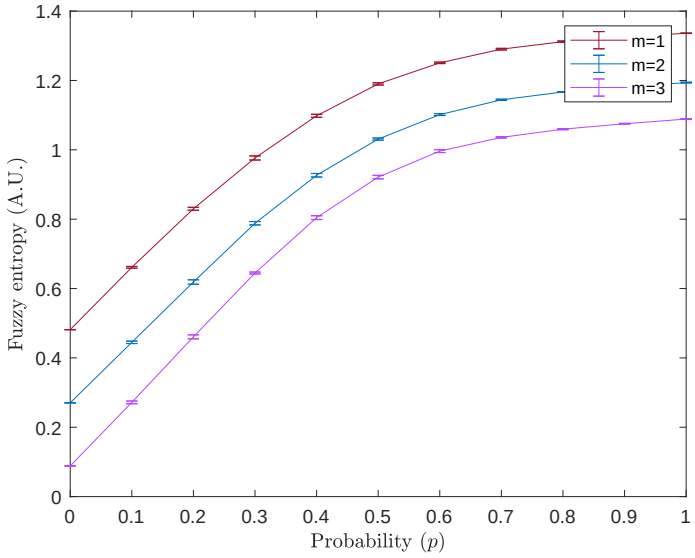


**Figure 5.5:** Fuzzy entropy of $\text{MIX}_{1D}(p)$ processes-based signals.

#### 5.1.3.1 Shuffling data

The following test, presented in figure 5.6, takes into consideration that shuffling data increases the irregularity due to random data reorganization [73]. For that reason, we have two curves: one for the signals based on $\text{MIX}_{1D}(p)$ processes definition (red curve) and one for the shuffled versions of them (blue curve).

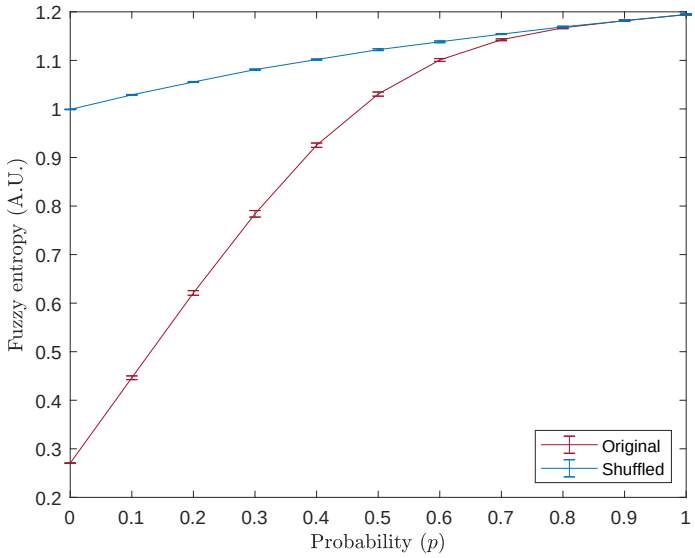


**Figure 5.6:** Fuzzy entropy of $\text{MIX}_{1D}(p)$ processes-based signals and their shuffled versions.

For both cases, due to the $\text{MIX}_{1D}(p)$ processes definition, is expected an increase on entropy values for an increase of $p$-value. However, for the shuffled signals is

expected an even higher entropy rise than the corresponding original signals. Even though this is verified, for $p \geq 0.7$ the values between original and shuffled data become closer which can be explained by the fact that for these probabilities values, $\text{MIX}_{1D}(p)$ processes-based signals are dominated by random processes. Therefore, the shuffling does not affect as much as it does for lower $p$ values. It can be established that $\text{FuzEn}_{1D}$ is able to determine irregularity and can distinguish a more irregular signal from a less irregular one.

#### 5.1.3.2 No baseline removal *VS* Baseline removal

As mentioned before, the baseline removal has not been done to account both local and global characteristics. Hence, the figure 5.7 shows the two curves for both algorithm versions: fuzzy entropy with baseline removal (blue curve) and without baseline removal (red curve). Both algorithms used the same $\text{MIX}_{1D}(p)$ processes-based signals to determine entropy as function of the probability. When opting to consider both local and global characteristics, it can be observed that the curve has a steeper slope. In addition, a better discrimination is verified with the $p$-value increase without baseline removal.

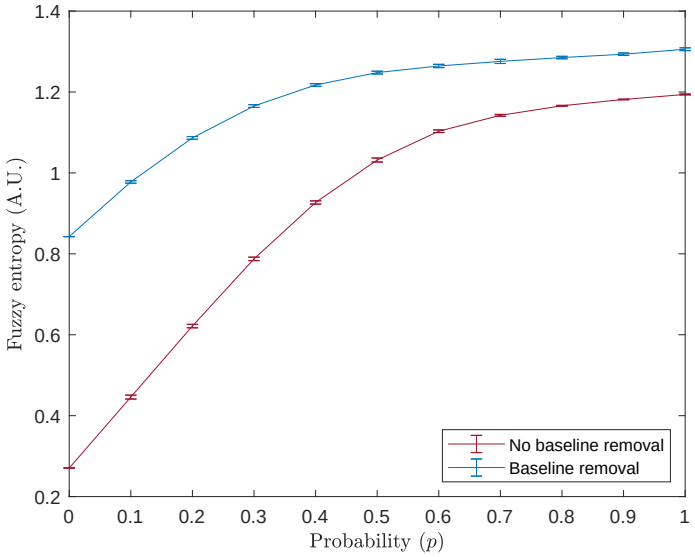


**Figure 5.7:** Fuzzy entropy with (blue curve) and without baseline removal (red curve) of $\text{MIX}_{1D}(p)$ processes-based signals.

### 5.1.4 Multiscale analysis on noise signals

The upcoming analysis is based on evaluating the different behavior of colored noise signals (white, pink, blue and brown noise) that present a power spectral density (PSD) dependence of $1/|f|^{\beta}$ with $\beta = 0$, $\beta = -1$, $\beta = +1$ and $\beta = -2$, respectively.

Costa *et al.* [39, 43] analysis approached the complexity of simulated white and pink noise.

It is reported that for $\tau = 1$, i.e., considering the original signal (without down-sampling) the entropy is higher for white noise. Despite that, pink noise remains constant for all scale factors and white noise suffers a monotonic decrease for $\tau \geq 5$ [39, 43]. In fact, in figure 5.8, it is shown that the $\text{MFE}_{1D}$ behavior is also very similar to the results shown by Azami *et al.* [60].

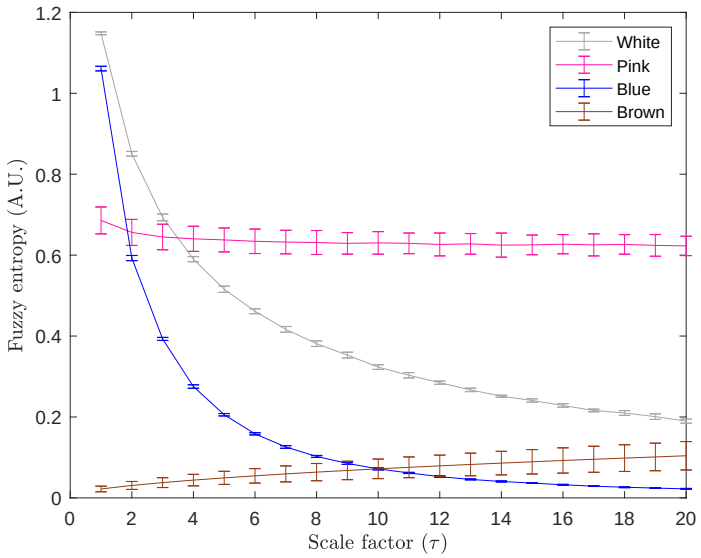


**Figure 5.8:** $\text{MFE}_{1D}$ behavior for white noise (gray), for pink noise (pink), blue noise (blue) and brown noise (brown) for $\tau_{max} = 20$.

Besides, it is verified that white noise has in fact higher entropy than pink noise for the first scale factor as reported by Costa *et al.* [39, 43].

Pink noise is constituted by complex structures throughout scale factors, leading to a constant multiscale profile (pink curve in figure 5.8) [39, 43]. Accordingly to Costa *et al.* [39], both entropy curves of white noise and pink noise should cross around $\tau = 4$, which can be observed in figures 5.8 and 5.9.

Another characteristic reported is that typically, the SD is higher for pink noise due to non-stationarity [39]. The table 5.2 shows the entropy's SD mean value of the studied signals.

**Table 5.2:** Mean value of the entropy's standard deviation for colored noises (white, pink, blue and brown) of all scale factors.

| Noise | Mean $\text{SD}_{Noise}$ of all scale factors |
|---|---|
| White | 0.0056 |
| Pink | 0.0280 |
| Blue | 0.0024 |
| Brown | 0.0235 |

As a result, when considering a multiscale analysis, there are two main guidelines to characterize signals' complexity [39]:

1. If a certain signal presents higher entropy for the majority of $\tau$'s compared to a second signal (example: pink noise over white noise) then, the first one is more complex;

2. A monotonic decreases indicates that the signals' information is only in the smallest scales.

Moreover, as shown in figure 5.8, other colored noises like blue noise and brown noise have been studied, extending the analysis on noise signals of Costa *et al.* [39, 43]. Taking into consideration the previous guidelines, the noise signals can be compared in terms of complexity.

Based on the first guideline, pink noise is more complex than blue, white noise and brown noise. In addition, blue noise curve is very similar to white noise, only containing the main information in the smallest scales (existence of a monotonic decrease - guideline 2) and brown noise has new information revealed in all scales. Therefore, one can conclude that brown noise can be considered as more complex than blue noise. Consequently, the decreasing order of noises' complexity is *pink*>*white*>*brown*>*blue*. Nonetheless, this order can be discussed since the behavior of brown noise is more similar to pink noise, showing the absence of a monotonic decrease. So, one could justify that the order of complexity is as in matter of a fact *pink*>*brown*>*white*>*blue* or even *brown*>*pink*>*white*>*blue* since the brown noise curve seems to be rising in stead of staying constant.

The monotonic decreases verified in white and blue noise are explained by the averaging process associated to the coarse-graining procedure. In each window of the procedure, the values are averaged and tend to become closer to a constant value and the signals gets "smoothed out". On the other hand, signals like pink noise do not show this behavior due to fluctuations of the signal, with new information being revealed in each scale factor [39].

#### 5.1.4.1 $MFE_{1D}$ behavior *VS* $MSE_{1D}$ behavior

Furthermore, $MFE_{1D}$ can be compared with $MSE_{1D}$ in figure 5.9. It can be observed that the curves behavior is similar. Even though the entropy values are not the same, an entropy measure is evaluated according to its differentiation ability, sensitivity to change in parameters, ability to quantify, among other characteristics rather the exact given values. According to this, one can conclude that $FuzEn_{1D}$ as an entropy measure overcomes $SampEn_{1D}$, as stated by previous works [44–46, 60, 64]. In figure 5.9, it can be observed how $FuzEn_{1D}$ is more accurate, since the SD values are clearly larger for $SampEn_{1D}$, being more visible for pink noise. Nevertheless, due to the nature of pink noise for both entropy measures the SD is higher than for white noise.

#### 5.1.4.2 $MFE_{1D}$ length dependence *VS* $MSE_{1D}$ dependence

An interesting feature of fuzzy entropy is that shows less dependence on the data's length when compared to $SampEn_{1D}$, revealing more consistency [45, 46]. $FuzEn_{1D}$ is able to obtain defined values of entropy even when is not possible for sample entropy.

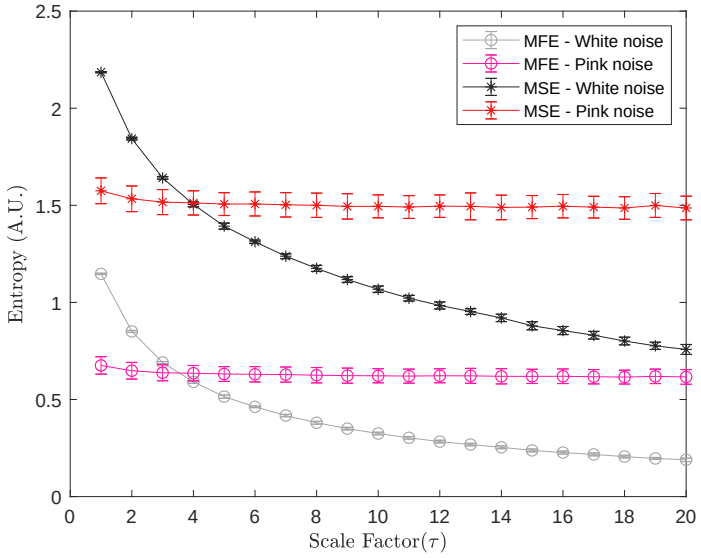


**Figure 5.9:** $MFE_{1D}$ and $MSE_{1D}$ behavior for white and pink noise signals of $N = 30000$ points with $\tau_{max} = 20$.

If a very short signal of $N = 100$ points is considered, as shown in figure 5.10, $FuzEn_{1D}$ is able to define the entropy value for 20 scale factors but, $SampEn_{1D}$ can only determine entropy for 2 scale factors. This reveals the lack of consistency of $SampEn_{1D}$ compared to $FuzEn_{1D}$.

Nonetheless, when considering data as small as the pink signals tested ($N = 100$ points) it should not be taken into account that many scale factors. For $\tau_{max} = 20$, for a pink signal of $N = 100$ points, the smallest coarse-grained time series will have 5 points. Consequently, the smallest coarse-grained time series will have more inconsistent results and with high SD values, shown in figure 5.10, for $\tau > 7$. This indicates that $FuzEn_{1D}$ is superior to $SampEn_{1D}$ but, for a short signal the maximum scale factor must be lower.

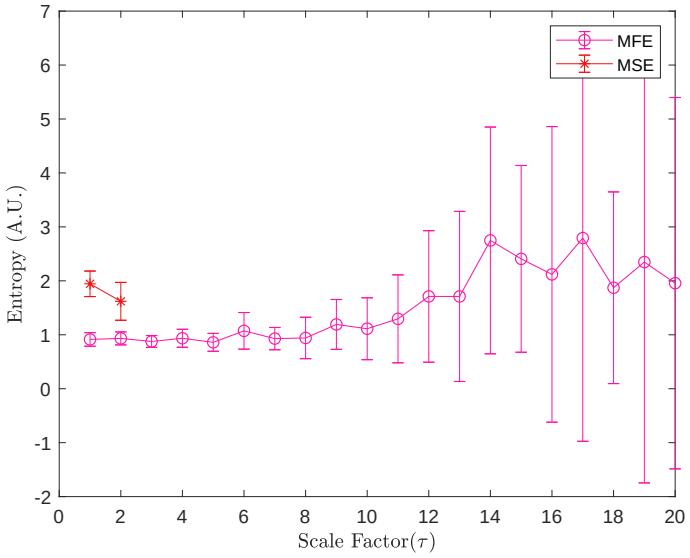


**Figure 5.10:** $MFE_{1D}$ and $MSE_{1D}$ behavior of white and pink noise signals with a length of $N = 100$ points and $\tau_{max} = 20$.

### 5.1.5 Biomedical application: signals of snoring events

This section is dedicated to $FuzEn_{1D}$ biomedical application. The parameters herein used are shown in table 5.1.

As mentioned before, for each subject, 50 snores have been selected (from data collected previously [62]) and through multiscale analysis entropy values have been obtained for $\tau_{max} = 40$. Then, for each subject, the mean $MFE_{1D}$ curve of the previous 50 curves corresponding to each snore was obtained.

For example, Costa *et al.* [39, 43] proposed a maximum scale factor of $\tau_{max} = 20$ for a time series of $N = 3 \times 10^4$ points. So, the smallest coarse-grained series has $N_{\tau_{max}} = N/\tau_{max} = 1500$ points. Knowing that each signal had $N = 6.5 \times 10^4$ points, the smallest coarse-grained signal will have $N_{\tau_{max}} = N/\tau_{max} = 3250$ points. Moreover, since a fuzzy entropy measure is being used, which was verified to have a more consistent behavior, one can say that consistent behavior is still verified for this amount of points.

In figure 5.11, for each group is represented a curve corresponding to the mean values of $MFE_{1D}$ subjects' curves belonging to that group.

It can be observed, in figure 5.11 (a), that the severe group (in dark blue) shows an higher entropy rise with the scale factor compared to the remaining groups. Furthermore, for $\tau \geq 20$ it is verified that the entropy profile stabilizes.

Moreover, it can be concluded according to Costa *et al.* [39, 43] analysis, that the severe and medium groups are the most complex ones. In addition, the control group is clearly the least complex one, showing the lower entropy values. However, differentiating the light SAHS stage's complexity from the simple snoring group is more difficult. Figure 5.11 (b) reveals that the profiles of these two groups cross each other twice and are easier to distinguish for higher scale factors.

Since the light SAHS group shows lower entropy values than the snoring group

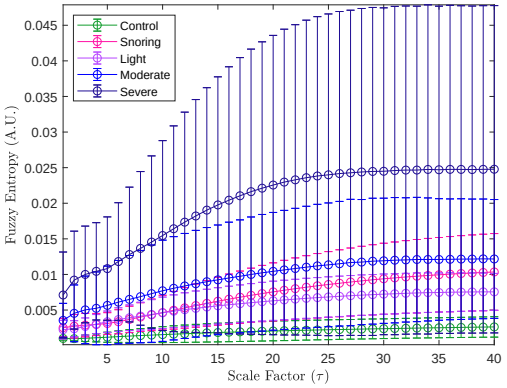


**(a)** 3 groups' stages of SAHS disease stages (light, moderate and severe), snoring group and control group.

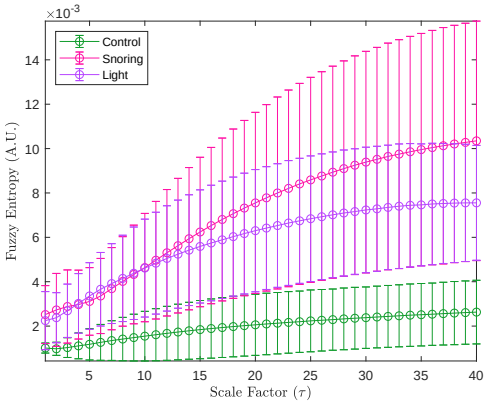


**(b)** Control group, snoring group and light stage of SAHS.

**Figure 5.11:** Mean $MFE_{1D}$ values for the control group, simple snoring group and light, moderate and severe stages of SAHS.

for a higher number of $\tau$, this leads to the conclusion that simple snoring group has, in fact, more complex structures behind the signal. This interesting feature might have the need to be explored in the future, since it is expected that, similarly to other stages, the simple snoring group would be less complex than the light SAHS group. If this was verified, the order of complexity would depend directly on the stage progression.

One rather important aspect, visible in figure 5.11, is the huge SD values of these $MFE_{3D}$ curves. As a matter of fact, these errors does not allow us to take extensive conclusions. So, within each group, a high variability of entropy values is existing. This might indicate the need of including more than 50 snores for each subject and more subjects as well to increase the amount of data in the study. Additionally, this could explain why we observe that simple snoring individuals, when considering the mean, are more complex than subjects suffering light SAHS. This situation must be confirmed with a more extensive analysis that leads to a smaller SD.

Nevertheless, this study leads to the conclusion that an entropy study for these signals can be promising in differentiating the several groups. For example, Qian *et al.* [1] indicates that an analysis based on snoring acoustics can reveal a better method to distinguish snoring subjects from OSAHS suffering ones. Furthermore, if considering that some moderate to severe cases can be missed according to Young *et al.* [4], the entropy analysis could allow in the future a simple and first conclusion to assist in diagnosis.

## 5.2 Bidimensional colored fuzzy entropy - $FuzEn_{C2D}$

Based on previous considerations, for further bidimensional and tridimensional analysis it can be taken into account the following considerations:

1. In opposition to Heaviside function, smoother changes are obtained in simi-

larity through the fuzzy function [45];

2. The fuzzy power, $n$, must be a small integer value and, based on literature regarding bidimensional measures [58, 73], $n = 2$ is esyablished;

3. The tolerance must be a constant value multiplied by the data standard deviation.

According to this, first, validation of $\text{FuzEn}_{C2D}$ is discussed, and finally, the two biomedical applications: the cutaneous microcirculatory study and the melanoma study.

### 5.2.1 Tolerance and embedding dimension sensitivity

Herein, an algorithm to determine the entropy on colored images is proposed. Therefore, validation is necessary. Similarly to the unidimensional version, the sensitivity of $\text{FuzEn}_{C2D}$ has been tested upon change of tolerance values between 0.06 and 0.48 (step of 0.06) times the color channel SD. Additionally, it has also been considered different embedding dimensions ($1 \leq m \leq 3$) and analyzed the algorithm behavior upon its change. Since $\text{FuzEn}_{C2D}$ considers three different values regarding the color channels, each RGB channel's entropy values can be displayed: $\text{FuzEn}_{R2D}$, $\text{FuzEn}_{G2D}$, and $\text{FuzEn}_{B2D}$ in figures 5.12, 5.13, and 5.14, respectively.

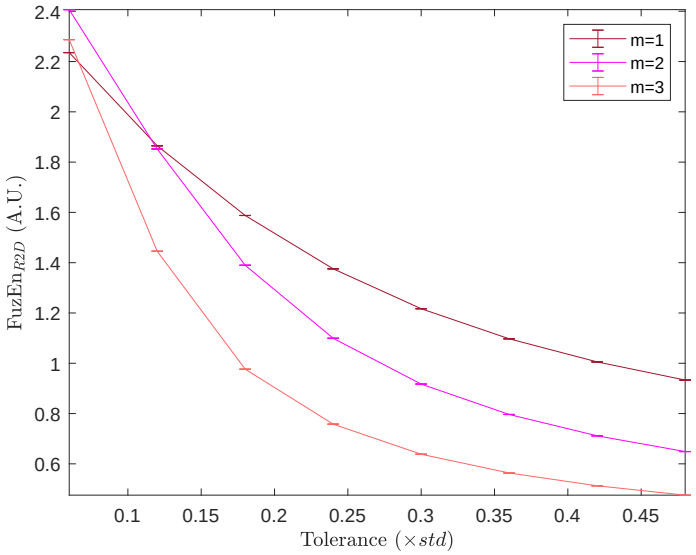


**Figure 5.12:** Tolerance sensitivity of $\text{FuzEn}_{R2D}$, considering different embedding dimensions, $1 \leq m \leq 3$, for the red channel, $\mathbf{U}_R$, of the image represented in figure 3.2 (a).

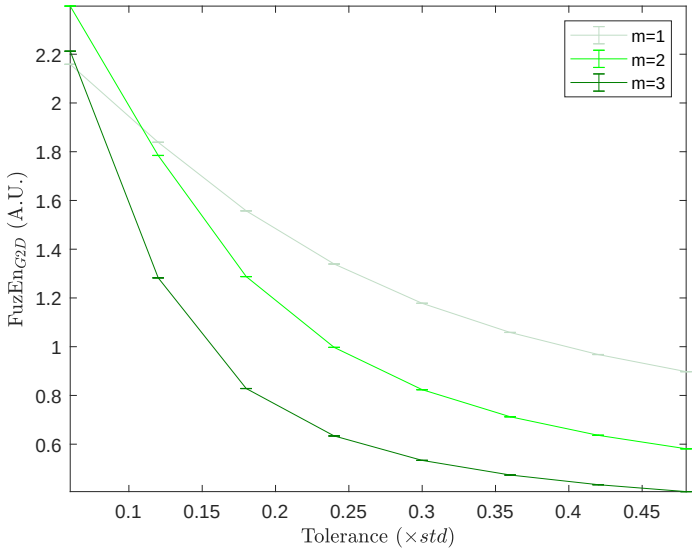


**Figure 5.13:** Tolerance sensitivity of FuzEn$_{G2D}$, considering different embedding dimensions, $1 \leq m \leq 3$, for the green channel, $\mathbf{U}_G$, of the image represented in figure 3.2 (a).

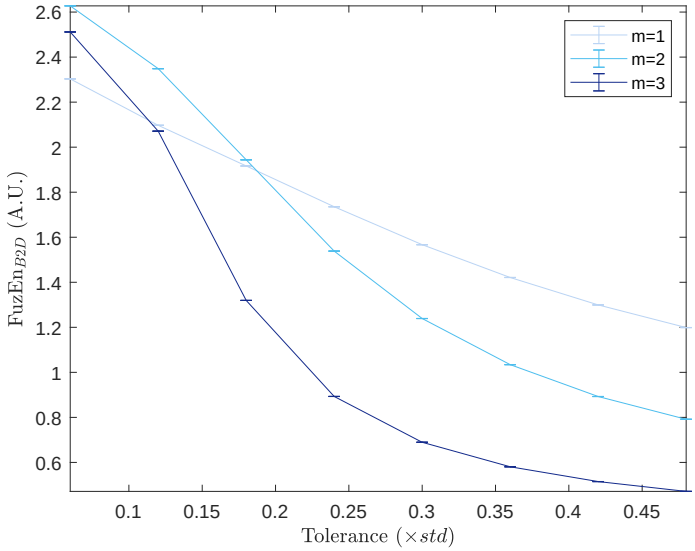


**Figure 5.14:** Tolerance sensitivity of FuzEn$_{B2D}$, considering different embedding dimensions, $1 \leq m \leq 3$, for the blue channel, $\mathbf{U}_B$, of the image represented in figure 3.2 (a).

FuzEn$_{C2D}$ shows low sensitivity upon change of $m$ and $r$ value, proving the reliability of this algorithm for different initial parameters [75]. Obviously, since each channel is characterized by different values, for a specific tolerance value, the entropy is not the same for all channels. Nevertheless, every channel shows a decreasing entropy behavior with $r$-value increase. In addition, for $m = 2$ and $m = 3$, a slower decrease rate of entropy values is observed for $r \geq 0.2$.

A fixed value of tolerance must be defined in order to avoid possible result fluctuations. Considering the interval of tolerance values given by Zheng *et al.* [64], $[0.10, 0.25] \times SD^K_{data}$, once more $r = 0.2 \times SD^K_{data}$, with $K = R, G, B$ [75] has been chosen.

### 5.2.2 MIX$_{2D}(p)$ processes and the embedding dimension behavior

Furthermore, in figure 5.15, the entropy behavior can be observed upon change of the $m$ parameter. Besides, it can also be verified the FuzEn$_{C2D}$'s ability to distinguish different irregularity levels since the entropy increases with the $p$-value increase. For this analysis, MIX$_{2D}(p)$ processes-based images have been used with a checkerboard background. It has been chosen to show only the red channel of these images since the results are similar for all the channels. This was expected due to the nature of these images. The entropy value of the background is zero and the values of pixels regarding MIX$_{2D}(p)$ processes are the same for the three channels.

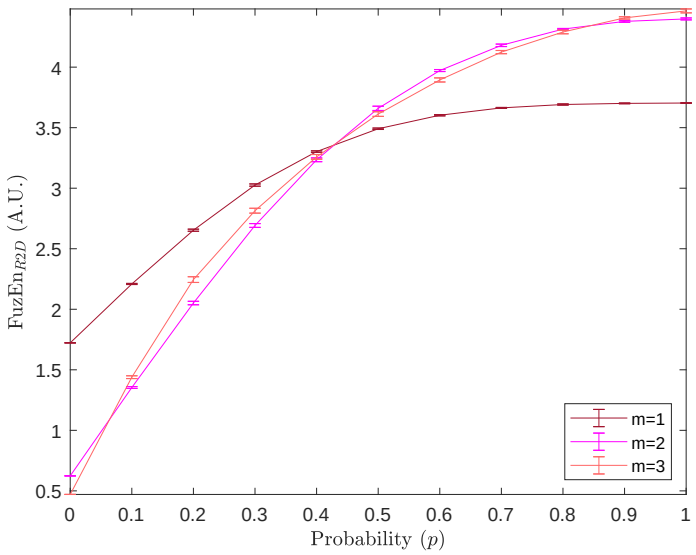


**Figure 5.15:** FuzEn$_{R2D}$ for the red component of MIX$_{2D}$ $(p)$ processes-based images with a checkerboard background.

Apart from differentiating added randomness levels, figure 5.15 reveals FuzEn$_{C2D}$ relatively low sensitivity of $m$-values variation. For the three channels, is visible that the values $m = 2$ and $m = 3$ reveal a closer entropy behavior between each other. Moreover, the increase of entropy is better discriminated.

According with previous considerations on the $m$-value, computational cost and literature [52, 55, 58, 73], for further tests the embedding dimension was established to $m = 2$ [75].

In table 5.3, the established parameters for further validation tests and biomedical applications are shown.

#### 5.2.2.1 Shuffling data

Shuffling data means to rearrange the data's components randomly [73]. Since this rearrangement increases irregularity [73], an increase on the entropy value can be expected for the shuffled data when compared to the original data. Therefore, similarly to the one-dimensional analysis, in figure 5.16, it can be observed the entropy values of the red channel of $\text{MIX}_{2D}(p)$ processes-based images (with a checker board background) and the their shuffled versions, for several $p$-values ($0 \leq p \leq 1$). In figure 5.16 can be observed that shuffling in fact increases the entropy of the channel of an image.

As explained before, the three channels are similar between each other for the $\text{MIX}_{2D}(p)$-based images. This can be explained by the fact the background does not interfere with the entropy values (since its value is zero) and that the entropy from $\text{MIX}_{2D}(p)$ processes is same for the 3 channels. Regarding the shuffled versions of each channel, obviously, due to the random process of rearranging the pixels the shuffled versions of each channel will be different between each other. Nonetheless, the figures are very similar so, it was chosen to only to arbitrarily show the red channel in this document.

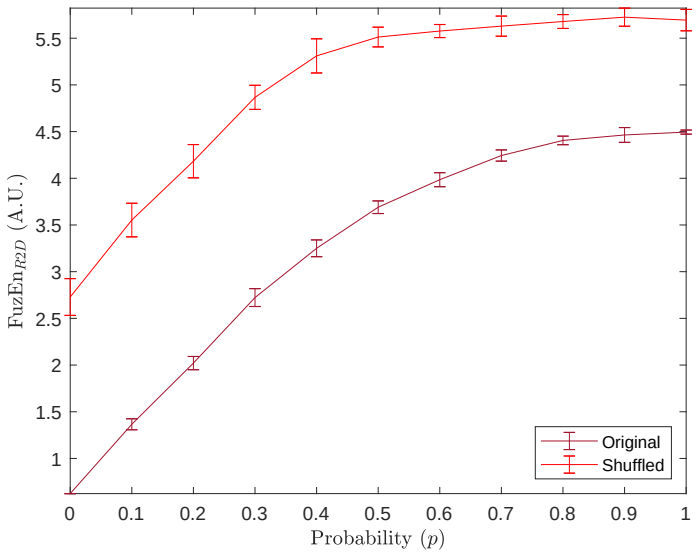


**Figure 5.16:** $\text{FuzEn}_{R2D}$ for the red component of $\text{MIX}_{2D}$ $(p)$ processes-based images with a checkerboard background and their shuffled versions, for $0.0 \leq p \leq 1.0$ (step of 0.1).

**Table 5.3:** Parameters values chosen for upcoming tests of $\text{FuzEn}_{C2D}$.

| ***Parameters*** | ***Chosen Values*** |
|---|---|
| $n$ | 2 |
| $m$ | 2 |
| $r$ | $0.2 \times SD^{K}_{data}$ |

### 5.2.3 Textural behavior of images from Colored Brodatz dataset

Upcoming, 6 textures from the CB database [76, 77] have been tested (see figure 3.2). The $\text{FuzEn}_{C2D}$ values obtained for the original images ($640 \times 640$ pixels), shown in table 5.4, have been compared with the mean value of 4 equal sub-images ($320 \times 320$ pixels each), shown in table 5.5.

The reliability of $\text{FuzEn}_{C2D}$ is proven due to the small SD values shown in table 5.5, with the values being inferior to 0.04 [75]. Moreover, comparing the two tables (5.4 and 5.5), it can be observed that the mean value obtained for each texture is very similar to the original one, with the value not differing more than around 2.52%. One can conclude that the algorithm has the ability to recognize these sub-images as having the same textural behavior [75].

**Table 5.4:** $\text{FuzEn}_{C2D}$ for CB textures represented in figures 3.2(b)-(g) of $640 \times 640$ pixels.

| Texture | $\textbf{FuzEn}_{R2D}$ | $\textbf{FuzEn}_{G2D}$ | $\textbf{FuzEn}_{B2D}$ |
|---|---|---|---|
| b) | 0.1972 | 0.2256 | 0.2461 |
| c) | 0.5554 | 0.7832 | 0.5262 |
| d) | 0.3400 | 0.6153 | 0.5235 |
| e) | 0.2605 | 0.3074 | 0.2438 |
| f) | 0.3520 | 0.3496 | 0.4152 |
| g) | 0.8255 | 0.7867 | 0.5643 |

**Table 5.5:** Mean and SD of $\text{FuzEn}_{C2D}$ for the 4 equal sub-images obtained through CB textures represented in figures 3.2(b)-(g) with $320 \times 320$ pixels each.

| Texture | $\textbf{FuzEn}_{R2D}$ | $\textbf{FuzEn}_{G2D}$ | $\textbf{FuzEn}_{B2D}$ |
|---|---|---|---|
| b) | $0.1934 \pm 0.0221$ | $0.2206 \pm 0.0289$ | $0.2399 \pm 0.0324$ |
| c) | $0.5558 \pm 0.0172$ | $0.7836 \pm 0.0252$ | $0.5265 \pm 0.0162$ |
| d) | $0.3399 \pm 0.0074$ | $0.6147 \pm 0.0125$ | $0.5231 \pm 0.0111$ |
| e) | $0.2601 \pm 0.0242$ | $0.3068 \pm 0.0297$ | $0.2434 \pm 0.0233$ |
| f) | $0.3548 \pm 0.0344$ | $0.3522 \pm 0.0337$ | $0.4189 \pm 0.0433$ |
| g) | $0.8244 \pm 0.0226$ | $0.7856 \pm 0.0206$ | $0.5638 \pm 0.0132$ |

### 5.2.4 Biomedical application: dermoscopic images

As biomedical applications for $\text{FuzEn}_{C2D}$ [75], it is shown the analysis of microcirculation and melanoma dermoscopic images. The parameters herein used are shown in table 5.3.

#### 5.2.4.1 Microcirculatory study

Upcoming, is the entropy evaluation of dermoscopic images to perform a cutaneous microcirculation study [75]. To prove that this measure is efficient and

a better choice than previous texture evaluators, the Haralick features upon these images are also shown to be compared with the $\text{FuzEn}_{C2D}$.

As mentioned, we started by calculating the considered texture descriptors, the Haralick features [40], which definitions are in table 3.2. Considering the RGB channels of an image, **U**, it is shown the average value of the nine subjects for each descriptor to compare with $\text{FuzEn}_{C2D}$ in tables 5.6 and 5.7, at rest and vasodilation presence, respectively. The symbol "-" represents an undefined value.

Moreover, the $p$-values have been obtained considering a statistical significance of $p \leq 0.05$ through the *Wilcoxon signed rank* test on these descriptors for each channel (table 5.8). The results reveal that the Haralick features are not able to identify statistical differences between the two microcirculatory states, having a minimum $p$-value of 0.0977 .

**Table 5.6:** Average values for each texture descriptor of the nine subjects when at rest.

| **Haralick Features** | $(\overline{\mathbf{U_R}} \pm \sigma) \times 10^{-01}$ | $(\overline{\mathbf{U_G}} \pm \sigma) \times 10^{-01}$ | $(\overline{\mathbf{U_B}} \pm \sigma) \times 10^{-01}$ |
|---|---|---|---|
| Variance | $1.85 \pm 1.43$ | $1.45 \pm 0.99$ | $2.62 \pm 1.06$ |
| Entropy | - | - | - |
| Uniformity | $6.66 \pm 2.39$ | $7.28 \pm 1.70$ | $4.67 \pm 1.90$ |
| Homogeneity | $9.08 \pm 0.71$ | $9.28 \pm 0.50$ | $8.70 \pm 0.54$ |
| 3rd order moment | $0.01 \pm 0.01$ | $0.01 \pm 0.01$ | $0.00 \pm 0.05$ |
| Inverse variance | - | - | - |

**Table 5.7:** Average values for each texture descriptor of the nine subjects when heat is applied and vasodilation is verified.

| **Haralick Features** | $(\overline{\mathbf{U_R}} \pm \sigma) \times 10^{-01}$ | $(\overline{\mathbf{U_G}} \pm \sigma) \times 10^{-01}$ | $(\overline{\mathbf{U_B}} \pm \sigma) \times 10^{-01}$ |
|---|---|---|---|
| *Variance* | $1.60 \pm 1.28$ | $1.94 \pm 1.12$ | $2.32 \pm 1.06$ |
| *Entropy* | - | - | - |
| *Uniformity* | $7.09 \pm 2.23$ | $5.98 \pm 2.26$ | $5.22 \pm 2.06$ |
| *Homogeneity* | $9.20 \pm 0.64$ | $9.03 \pm 0.56$ | $8.85 \pm 0.53$ |
| *3rd order moment* | $0.00 \pm 0.01$ | $0.01 \pm 0.03$ | $0.00 \pm 0.02$ |
| *Inverse variance* | - | - | - |

**Table 5.8:** $p$-values of the Wilcoxon signed rank test performed on the Haralick features extracted from the nine subjects' dermoscopic images considering the two microcirculatory states for the images' red ($\text{U}_R$), green ($\text{U}_G$) and blue ($\text{U}_B$) channels.

| **Haralick Features** | $\mathbf{U}_R$ | $\mathbf{U}_G$ | $\mathbf{U}_B$ |
|---|---|---|---|
| *Variance* | 0.8203 | 0.1289 | 0.4258 |
| *Entropy* | - | - | - |
| *Uniformity* | 0.8203 | 0.0977 | 0.4258 |
| *Homogeneity* | 0.8203 | 0.1289 | 0.4961 |
| *3rd order moment* | 0.9102 | 1.0000 | 0.7344 |
| *Inverse variance* | - | - | - |

**Table 5.9:** FuzEn$_{C2D}$ average values for the nine subjects of the dermoscopic images at rest and after heat applied (vasodilation).

| **FuzEn$_{C2D}$** | $(\overline{\mathbf{U_R}} \pm \sigma) \times 10^{-1}$ | $(\overline{\mathbf{U_G}} \pm \sigma) \times 10^{-1}$ | $(\overline{\mathbf{U_B}} \pm \sigma) \times 10^{-1}$ |
|---|---|---|---|
| *Rest* | $2.07 \pm 0.07$ | $2.05 \pm 0.07$ | $2.03 \pm 0.09$ |
| *Vasodilation* | $1.97 \pm 0.10$ | $1.95 \pm 0.12$ | $1.93 \pm 0.12$ |

Hereafter, the obtained values of FuzEn$_{C2D}$ for the dermoscopic images of the same nine subjects are shown. The table 5.9 shows fuzzy entropy average values obtained for the $U_R$, $U_G$, and $U_B$ image components, when the subject is at rest and when heat is applied on the skin, causing blood vessels to dilate. One can verify that when at rest, the entropy of these images tends to be higher than when vasodilation occurs.

Finally, the $p$-values were obtained through a *Wilcoxon signed rank* test for a statistical significance of $p \leq 0.05$. The microcirculatory states being tested can be differentiated through red and green channel, in which $FuzEn_{R2D}$ and $FuzEn_{G2D}$ $p$-values are lower than 0.05 (see table 5.10). Also, the $p$-value obtained for the blue channel is very close to the considered statistical significance level.

This analysis allowed to conclude that FuzEn$_{C2D}$ is a promising feature to evaluate this type of images, having the advantage of considering the colors of those images. This study can be improved by increasing the number of subjects being analyzing. In addition, a method to reproduce vasoconstriction could be included in the protocol to study an additional microcirculatory condition. This might be useful to extend the analysis on microcirculation.

**Table 5.10:** $p$-values obtained using a *Wilcoxon signed rank* test performed on the fuzzy entropy values for both conditions, rest and heat, of the 9 subjects dermoscopic colored images, considering the corresponding channels of the image.

| **FuzEn$_{C2D}$** | ***p*-value** |
|---|---|
| **FuzEn$_{R2D}$** | 0.0117 |
| **FuzEn$_{G2D}$** | 0.0391 |
| **FuzEn$_{B2D}$** | 0.0742 |

#### 5.2.4.2 Melanoma study

Herein, dermoscopic image dataset from [79, 80] are tested. This dataset is constituted by images clinically diagnosed as *common nevus* (80 images), *atypical nevus* (80 images), and *melanoma* (40 images).

FuzEn$_{C2D}$ has been used to evaluate the entropy associated with each group. The results from FuzEn$_{C2D}$ applied to this colored dermoscopic images are represented in figures 5.17 (a), 5.17 (b), and 5.17 (c), for the red ($\mathbf{U}_R$), green ($\mathbf{U}_G$) and blue ($\mathbf{U}_B$) channels, respectively.

In figure 5.17 (a), the entropy values of the red channel reveal that the highest median entropy value belongs to *common nevi* group (CNG), then, the second

highest one is for the *atypical nevi* group (ANG), and finally, the *melanoma* group (MG) presents the lowest median value. The same happens in figure 5.17 (b) and 5.17 (c).

Within the red channel, ANG is the group with more outliers (4). CNG represents the group with the highest number of outliers for green channel (9) and blue channel (4).

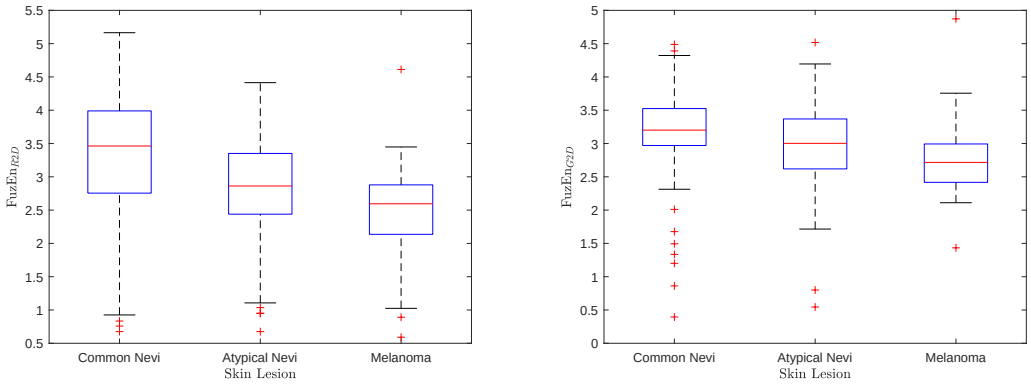


**(a)** $FuzEn_{R2D}$




**(b)** $FuzEn_{G2D}$

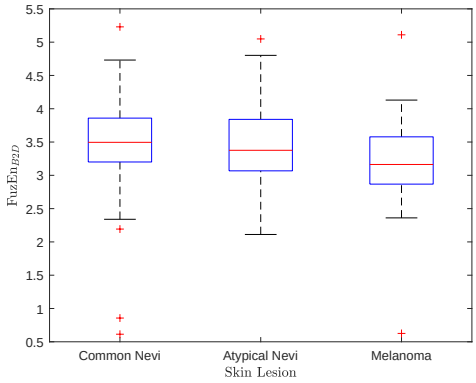


**(c)** $FuzEn_{B2D}$

**Figure 5.17:** Box plots with $FuzEn_{C2D}$ values of *common nevi*, *atypical nevi*, and *melanoma* skin lesions.

The following analysis was preceded by a normality test. In appendix B, it is shown the results obtained with *Shapiro-Wilk* test to assess if the sampled population of $\text{FuzEn}_{C2D}$ values, for each channel, of each group followed a normal distribution or not. As shown, even though the sample's size is large enough ($N > 15$) for a parametric test, not all data follows a normal distribution so, the *Kruskal-Wallis* non-parametric test has been performed to compare the three groups.

Table 5.11 reveal the $p$-values obtained with *Kruskal-Wallis* test to differentiate *common nevi*, *atypical nevi*, and *melanoma*, for a statistical significance of $p < 0.05$. The null hypothesis is that the dataset groups come from the same distribution, which is rejected for the three channels. Therefore, one can conclude that, independently of the channel, $\text{FuzEn}_{C2D}$ values of each group are not from the same distribution.

**Table 5.11:** *Kruskal-Wallis* test: mean rank for the different skin lesions for each RGB channel of the images being tested. $p$-values obtained for the three channels to test if within each channel the three groups (common nevi, atypical nevi, and melanoma) come from different distributions (for $p < 0.05$).

| $\mathbf{FuzEn_{C2D}}$ | **Mean Rank** | | ***p*-value** |
|---|---|---|---|
| $\mathbf{FuzEn}_{R2D}$ | *Common Nevi* | $123.2 \pm 6.5$ | 2.5E-06 |
| | *Atypical Nevi* | $94 \pm 6.5$ | |
| | *Melanoma* | $68.1 \pm 9.2$ | |
| $\mathbf{FuzEn}_{G2D}$ | *Common Nevi* | $116.6 \pm 6.5$ | 3.0E-04 |
| | *Atypical Nevi* | $99.1 \pm 6.5$ | |
| | *Melanoma* | $91.2 \pm 9.2$ | |
| $\mathbf{FuzEn}_{B2D}$ | *Common Nevi* | $110.5 \pm 6.5$ | 1.2E-02 |
| | *Atypical Nevi* | $102.2 \pm 6.5$ | |
| | *Melanoma* | $77.3 \pm 9.2$ | |

Moreover, it can be verified in table 5.12 that it is possible to differentiate the *common nevi* lesion from the *atypical* one through entropy of red channels with statistical significance of 5%. On the other hand, entropy of all three channels allows to differentiate *common nevi* from *melanoma* for $p < 0.05$. Finally, the entropy values of the green channel can differentiate *atypical nevi* from *melanoma* skin lesions, considering a statistical significance of 5%.

This leads to the conclusion that this discrimination of entropy values for each color channel allows us to differentiate one lesion from another. Having that said, it has been shown that, at least for one color channel, the entropy values are statistically different between two groups of skin lesions.

**Table 5.12:** *Kruskal-Wallis* $p$-values obtained for the three channels to test if the three groups (*common nevi*, *atypical nevi*, and *melanoma*) are statistically different (for $p < 0.05$) between each other.

| $\mathbf{FuzEn_{C2D}}$ | ***p*-value** | |
|---|---|---|
| $\mathbf{FuzEn_{R2D}}$ | CNG *vs.* ANG | 0.004 |
| | CNG *vs.* MG | 0.000 |
| | ANG *vs.* MG | 0.054 |
| $\mathbf{FuzEn_{G2D}}$ | CNG *vs.* ANG | 0.136 |
| | CNG *vs.* MG | 0.000 |
| | ANG *vs.* MG | 0.034 |
| $\mathbf{FuzEn_{B2D}}$ | CNG *vs.* ANG | 0.637 |
| | CNG *vs.* MG | 0.009 |
| | ANG *vs.* MG | 0.068 |

## 5.3 Tridimensional fuzzy entropy - FuzEn$_{3D}$

Further on, the FuzEn$_{3D}$ response to change in parameters and to different textural behaviors is shown. Moreover, a multiscale approach has been performed on volumes composed by different types of noise.

As mentioned previously, according to figure 5.1, the $n$-value must be a small integer value and the tolerance must be a constant multiplied by the data's SD, $r = k \times SD_{data}$.

The fuzzy power parameter was set to $n = 2$. Even though there is still no reference to tridimensional fuzzy entropy measures, this value was chosen according to other studies on fuzzy entropy [45, 46, 58, 60, 64, 73, 75].

Furthermore, considering the fuzzy function behavior upon $n$-values variation, shown previously in figure 5.1 (a), this value allows us to verify smooth changes in similarity between templates.

Finally, our analysis will include the study of a dataset composed by healthy subjects and individuals suffering IPF.

### 5.3.1 Tolerance and embedding dimension sensitivity

First, the sensitivity to parameters of FuzEn$_{3D}$ was tested. Figure 5.18 shows the FuzEn$_{3D}$ sensitivity to tolerance variation, considering $0.06 \times SD_{vol} \leq r \leq 0.48 \times SD_{vol}$ (step of 0.06). In addition, several values of embedding dimension, $m$, have also been considered to evaluate the behavior of the algorithm.

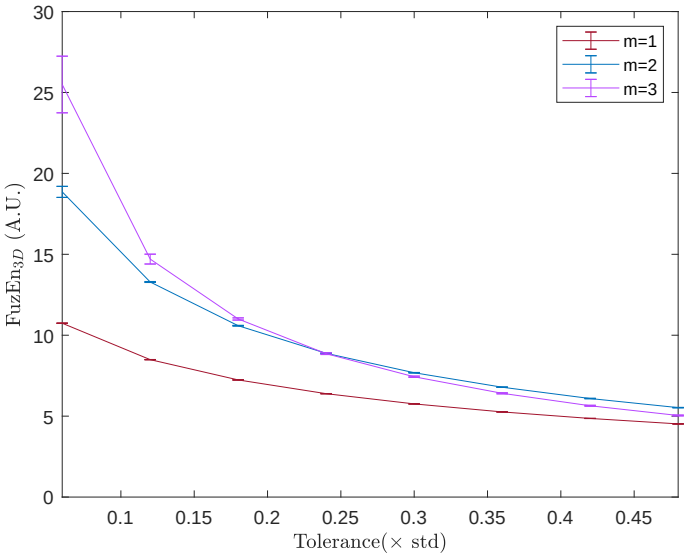


**Figure 5.18:** FuzEn$_{3D}$ sensitivity to change of tolerance, $r$, between the values $0.06 \times SD_{data}$ and $0.48 \times SD_{data}$, using white noise cubes for $m = 1$, $m = 2$ and $m = 3$.

A relatively low sensitivity to change of tolerance can be observed. Besides, the behavior of FuzEn$_{3D}$ for $m = 2$ and $m = 3$ is similar. Moreover, as observed before for uni-, and bi-dimensionless versions, it is verified the absence of undefined values.

For $r \geq 0.2 \times SD_{volume}$, the rate of entropy decrease is smaller. The algorithm's shows consistency, allowing to select with freedom the $r$ parameter [45, 46].

When choosing a larger $r$-value, the SD of entropy will be smaller. However, if this value is too large it might result in information lost [45].

Based on the tolerance interval of $[0.10, 0.25] \times SD_{data}$ defined by Zheng *et al.* [64], we have chosen $r = 0.2 \times SD_{data}$ for the remaining validation and biomedical tests. By fixing the tolerance value, we are able to compare the results easily.

### 5.3.2 $\text{MIX}_{3D}(p)$ processes and embedding dimension behavior

Regarding the choice of embedding dimension, in figure 5.19, the entropy of $\text{MIX}_{3D}(p)$ processes-based volumes are shown for different $m$-values. The $\text{FuzEn}_{3D}$'s ability to determine different irregularity levels can be verified. In addition, an increase of entropy with the increase of $p$ is observed. Besides that, as the $m$ increases the slope of the curve also increases. Therefore, for a higher $m$ is easier to observe that for a higher level of randomness (higher $p$-value) the volume has a higher level of irregularity.

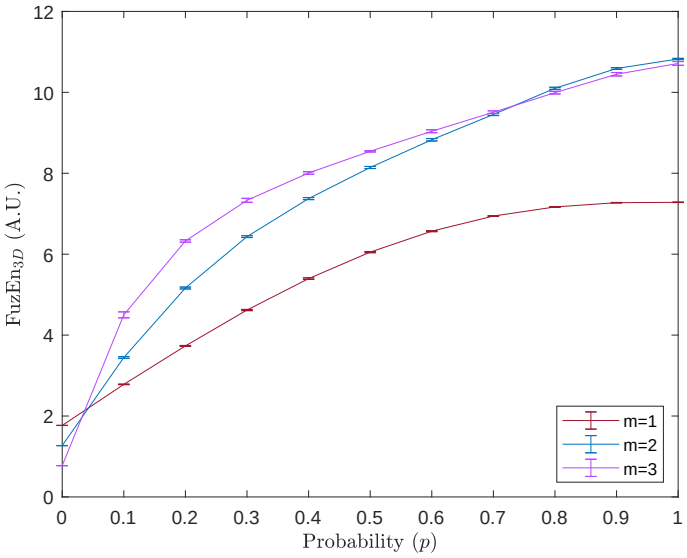


**Figure 5.19:** $\text{MIX}_{3D}$ $(p)$ processes volumes for $m = 1$, $m = 2$ and $m = 3$.

The embedding dimension parameter was established to $m = 3$ for the upcoming tests due to a higher consistency. The goal is to avoid voxel-by-voxel comparison but, still have a reasonable computational time. Moreover, for tridimensional entropy measures has been suggested to use an odd number so the template cube would have a central point [54, 71]. The table 5.13 contains the established parameters to be used in further tests.

#### 5.3.2.1 Shuffling data

Similarly to $\text{FuzEn}_{1D}$ and $\text{FuzEn}_{C2D}$, it was verified if, by shuffling the voxels, the entropy increases compared to the entropy of the original volume. In figure 5.20, for each $p$-value, $\text{FuzEn}_{3D}$ values are indeed higher for the shuffled versions, as expected. As mentioned previously, shuffling data increases the randomness level leading to higher irregularity levels therefore, the entropy values are expected to be higher.

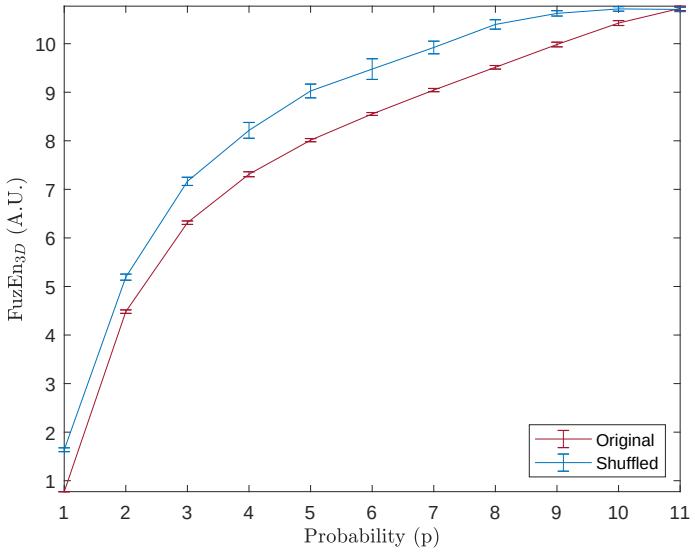


**Figure 5.20:** $\text{FuzEn}_{3D}$ of 10 cubes defined by $\text{MIX}_{3D}$ $(p)$ processes and their shuffled versions for $0.1 \leq p \leq 1.0$.

### 5.3.3 Pattern-based volumes analysis

A pattern analysis has also been done, guided by a similar analysis done by Moore and Marchant [54]. As mentioned in the chapter *Materials*, 6 cubes composed by different patterns have been tested. The table 5.14 shows $\text{FuzEn}_{3D}$ values for those pattern-based volumes.

Knowing that the first four volume are composed by regular patterns, the table 5.14 reveals $\text{FuzEn}_{3D}$ ability to identify that orderness. For example, cube 1 and 3, are extremely regular and the entropy value reveals that ($\text{FuzEn}_{3D} = 0$). In section 3.1.5, it is mentioned that cube 1 is composed by near-zero values and that cube 3 is a checkerboard-based pattern.

**Table 5.13:** Parameters values chosen for upcoming tests of $\text{FuzEn}_{3D}$.

| ***Parameters*** | ***Chosen Values*** |
|---|---|
| $n$ | 2 |
| $m$ | 3 |
| $r$ | $0.2 \times SD_{data}$ |

**Table 5.14:** $FuzEn_{3D}$ values for the six pattern volumes considered.

| Cubes | $FuzEn_{3D}$ |
|---|---|
| 1 | 0.0000 |
| 2 | 0.0443 |
| 3 | 0.0000 |
| 4 | 0.1404 |
| 5 | 10.1504 |
| 6 | 26.6905 |

In addition, cube 2, constituted in one-half by zeros and in the another half by ones, also shows a low entropy value, as expected. Finally, cube 4, showing diagonal stripes, and therefore, more irregular than cube 2, shows a higher entropy value but, still smaller than the more irregular volumes (cube 5 and 6).

Both cube 5 and 6, due to their irregular behavior (see figures 3.5 (e) and 3.5 (f)), are expected to show higher entropy values, which is in fact verified. Besides, this measure reveals that the last volume, cube 6, is the most irregular from the 6 volumes tested.

### 5.3.4 Multiscale analysis on noise signals

Furthermore, the characterization of colored noise in terms of complexity has been performed. This study on noise volumes was based on Costa *et al.*'s [39, 43] work and is similar to the study performed in section 5.1.4. The entropy values were obtained for 10 scale factors ($\tau_{max} = 10$) in a multiscale analysis for white, pink, blue, and brown noise.

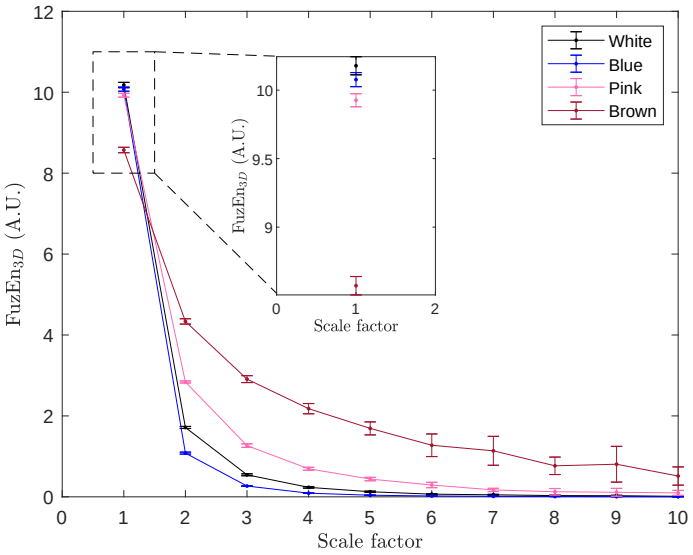


**Figure 5.21:** $MFE_{3D}$ values for white, pink, blue and brown noise, considering $\tau_{max} = 10$.

As it is shown in figure 5.21, the $MFE_{3D}$ curves have been obtained and white

noise reveals a higher entropy value for $\tau = 1$ than pink noise, as expected. Besides, pink noise after $\tau \geq 2$ does not decrease as much as white noise, and the two entropy curves cross each other. Therefore, one can conclude that pink noise is more complex than white noise, since the pink noise volume has higher entropy values for the majority of scale factors, according to Costa *et al.* [39] analysis.

Additionally, all the volumes show a monotonic decrease of the entropy, establishing therefore, that these volumes contain a higher amount of information in the smaller scales [39].

Concluding, for $\tau = 1$ the entropy is lower for noise with a $\beta \leq 0$. Although, blue noise has $\beta \geq 0$, the entropy value is lower than white noise which at first sight would indicate less complexity. However, these values are very similar. Nevertheless, when taking into account the multiscale analysis, considering the highest entropy values for majority of scale factors, the more complex noise (by decreasing order) are: brown, pink, white, and finally, blue noise.

### 5.3.5 Biomedical application: volumetric CT scans of patients suffering idiopathic pulmonary fibrosis

Finally, the last test involves establishing if there is a statistical difference between two different groups of individuals: healthy subjects and individuals suffering idiopathic pulmonary fibrosis. For each subject, a ROI of $50 \times 50 \times 50$ voxels has been established, with the first point being the most peripheral and basal point possible, considering the condition mentioned before in section 3.2.3.

An multiscale approach was applied, using a $\tau_{max} = 10$, and therefore, the smallest coarse-grained volume has $5 \times 5 \times 5$ voxels. Figure 5.22 show the $\text{MFE}_{3D}$ mean values for each scale factor for both groups: healthy group and IPF-suffering individuals.

In figure 5.22, it can be observed that the mean $\text{MFE}_{3D}$ values are higher for the patients group than for healthy people (except for $\tau = 10$). For $\tau \leq 4$, a decrease is verified on the entropy of both groups. Then, for $\tau = 5$ a small rise on entropy is experienced. Nevertheless, for the higher scale factors the entropy decreases once more for both groups. For $\tau = 10$, the behavior is reverted once more, and the entropy increases, having th healthy group the highest entropy value.

Considering the number of samples ($N > 15$), the normality of each group has been inferred, for each scale factor. Within each scale factor, the goal is to differentiate both groups. In appendix B.2, we show the $p$-values obtained through a *Shapiro-Wilk* test to verify if the datasets follow a normal distribution or not. According to that, for each scale factor, if at least one group is not normal then, the test performed to verify the existence of statistical significance between the two groups is the *Wilcoxon rank sum* test. Otherwise, the parametric *t-test* has been used. As shown, only $\tau = 2$ entropy values have been tested with the *t-test* and the remaining ones were tested with *Wilcoxon rank sum*.

For both statistical tests, a statistical significance for a $p < 0.05$ has been considered. The results are shown in table 5.15.

Table 5.15 proves that the ability of $\text{FuzEn}_{3D}$ to identify statistical differences between the two groups for 5 out of 10 scale factors ($\tau = 3, 4, 6, 7, 8$) for $p < 0.05$.

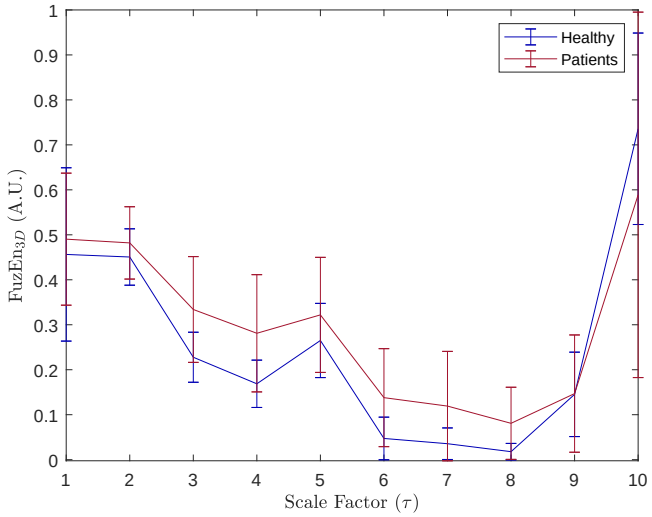


**Figure 5.22:** $MFE_{3D}$ mean values for $1 \leq \tau \leq 10$ for the healthy individuals and subjects suffering IPF (patients).

So, the first goal for this biomedical application was achieved. Nonetheless, knowing the importance of quantification, there is a demand of amplifying this analysis to include more ROI's volumes with similar selection methods (eventually, volumes from both lungs), or considering the lung as a whole for processing purposes, which will necessarily consume an huge amount of time.

**Table 5.15:** $p$-values for each scale factor considering a statistical significance for a $p$ inferior to 0.05 (corresponding to the symbol $^*$) between the two groups: subjects suffering IPF and healthy ones.

| **Scale Factor** $\tau$ | ***p*-value** |
|---|---|
| 1 | 2.1E-01 |
| 2 | 1.2E-01 |
| 3 | 2.9E-05* |
| 4 | 7.0E-06* |
| 5 | 1.4E-01 |
| 6 | 1.9E-05* |
| 7 | 3.9E-05* |
| 8 | 2.5E-05* |
| 9 | 5.3E-01 |
| 10 | 7.4E-01 |

# 6 Conclusion and final remarks

During the development of this Master thesis project, the applicability of fuzzy entropy as an entropy measurement algorithm to uni-, bi-, and tridimensional data has been studied. For the three cases, the algorithms required validation before being applied in biomedical datasets. Through simulated data the proposed algorithms based on fuzzy entropy were validated. Moreover, real data has been tested to demonstrate these algorithms applicability in the biomedical field.

## 6.1 Main conclusions

Regarding the unidimensional analysis, fuzzy entropy was proven to outstand sample entropy in several aspects. First, $\text{FuzEn}_{1D}$ showed only a decrease of 54.6% within an tolerance interval of $[0.06; 0.48]$ in opposition to the 60.9% decrease of $\text{SampEn}_{1D}$. Therefore, being clearly less sensitive to tolerance change than the sample entropy. When considering the multiscale approach, more accurate values of $\text{MFE}_{1D}$ were achieved regarding pink and white noise than for $\text{MSE}_{1D}$. In addition, for short signals, the choice of $\text{FuzEn}_{1D}$ to determine entropy can reveal to be decisive in order to avoid undefined values. Having pink signals of $N = 100$ points, $\text{MFE}_{1D}$ is still able to determine entropy values for all 20 scale factors (even if with less consistency than considering larger signals). The lack of baseline removal of $\text{FuzEn}_{1D}$ was shown to translate in a steeper slope than the original definition (with a baseline removal), for an increase of $p$-value on $\text{MIX}_{1D}(p)$ processes-based signals. In addition, through $\text{MIX}_{1D}(p)$ processes-based signals testing, *shuffling* data was proven to increase the entropy. Finally, regarding validation of $\text{FuzEn}_{1D}$, through $\text{MFE}_{1D}$ it is possible to establish a complexity order of several noise signals, with pink noise being the most complex noise compared to white, brown, and blue noise.

As a biomedical application, a study on audio snore related signals was conducted. This analysis revealed the importance of determining complexity of each stage of SAHS. Nevertheless, the identification of statistical significance between different sleep disorder SAHS stages is not yet possible. However, the study once it includes more patients and snores might reveal to be promising, and have, in the future, that goal achieved.

In the multidimensional field, dermoscopy allied to fuzzy entropy measures color-based can become a strong and helpful medical tool. During the validation tests, low sensitivity to tolerance and embedding dimension parameter for $\text{FuzEn}_{C2D}$ was verified. Similar behavior for all RGB channels was verified when testing $\text{MIX}_{2D}(p)$ processes-based images (with checkerboard background), as expected. Moreover, $\text{FuzEn}_{C2D}$ was able to successfully differentiating different randomness levels, either when the $p$-value associated to $\text{MIX}_{2D}(p)$ is increased or, when shuffling is applied to the image being tested. Further on, $\text{FuzEn}_{C2D}$ was proven to be a reliable measure. When comparing original textural images from the *Colored Brodatz* database [76, 77] and the mean value of their sub-images, the SD value was never higher than 0.04.

Concerning the microcirculation study, statistical differences were encountered

between a relaxed and vasodilated skin state with $\text{FuzEn}_{C2D}$. On the other hand, classical textural evaluators, like *Haralick features* [40], revealed a minimum $p$-value of 0.098 regarding the same dataset. Moreover, even though differentiating *common nevi* lesions from *atypical* ones is still a difficult task, the study of PH2 dataset [79, 80], $\text{FuzEn}_{\text{R2D}}$ can differentiate both. Furthermore, $\text{FuzEn}_{C2D}$ can determine statistical differences, independently of the channel, between *melanoma* lesions and *common* ones. At last, through the green channel differentiating *melanoma* and *atypical nevi* is possible.

Besides relatively low sensitivity to change in parameters, $\text{FuzEn}_{3D}$ has proven to be a helpful tool in discriminating different irregularity levels. Further on, several textural-based volumes were analysed according to their inherent regularity (or irregularity). The most regular volumes were shown to have an entropy of zero (volume composed by close values to zero and checkerboard-based volume). In addition, the most irregular one (composed by an uniform random distribution) revealed to have the highest entropy. On the subject of multiscale analysis, the brown noise volume was found out to be the most complex compared to the remaining noise types (white, pink, and blue noise).

As for the tridimensional biomedical application, the study can already reveal that this entropy measure is able to detect the existence of the studied deathly pulmonary disease for 5 out of 10 scale factors.

## 6.2 Future work and developments

According to the previous results, regarding the application of unidimensional fuzzy entropy to snoring signals, promising results were obtained on the stage progression of obstructive SAHS. Increasing both the amount of snores for each patient, and gathering more subjects for each stage could allow us to have a more accurate analysis.

In addition, the snoring analysis with fuzzy entropy could be extended for different types of snoring, discriminating the results of regular and non-regular snore. Moreover, in the future, detection and snore selection could be done with a protocol procedure and already verified in literature in order to improve these primary results.

In the imaging field, using a colored bidimensional entropy measure could lead to several applications in the biomedical area. Even though only applied on dermoscopic images, it could be a relevant tool in other imaging fields like on histological images, for example.

Furthermore, implying this analysis to assist in microcirculatory assessment can be medical relevant since the tools to do so are still limited. In a further study, continuing the research and increase the number of volunteers is essential towards a proper validation of this measure by the medical community.

Regarding textural behavior, since most comparisons between several methods only concerned gray-scaled versions of images, this can be an opportunity to extend this type of studies to colored textures.

Since melanoma and related skin lesions are still difficult to evaluate, quantify in terms of progression, and in dubious cases difficult to diagnose by a less-experienced

dermatologist, having an entropy-based measure able to do this can be of the utmost importance in the medical and imaging field. Besides extending the database used, interconnecting this assessment method with verified classification and segmentation tools can have a great importance.

In the tridimensional field, some barriers were already broken in terms of using entropy to assess the regularity of volumetric data. Nonetheless, since it is very time-consuming, a code optimization might be needed or modifications in the definition of the algorithm without interfering the consistency expected of a fuzzy entropy measure. Additionally, another imperative goal to be fulfilled is to extend the IPF analysis to a more global view to guarantee that $\text{FuzEn}_{3D}$ is able to quantify this disease, a medical challenge of great importance in the medical field. Including more subjects and therefore, more data will also be a very important task to perform in the future.

This new fuzzy entropy measure in other types of 3D data can be performed and reveal other important results in several other biomedical imaging applications.

To conclude, these entropy determination-based tools can be of utmost importance to establish a bridge between biomedical engineering and medical doctors, allowing a simple, cheap, and efficient analysis.

# Appendices

# A Vascularisation dermoscopy protocol

Authors: Andreia Gaudêncio[1] and Dr. Clémence Berthin[2]
*Based on a french version of Dr. Clémence Berthin*

[1] *LIBPhys-UC, Physics Department, University of Coimbra, Portugal*

[2] *Dermatology Department, University Hospital Center of Angers,France*

## A.1 Task

The dermoscopic images were collected to be used in a study of differentiating two micro circulation states. For more detailed information on the results of this study, please consult the work of Hilal *et al.* [75] and the *Results* chapter of this document. The collection conditions are specified in this protocol, along with other important informations.

## A.2 Introduction

Dermoscopy or Epiluminescence Microscopy (ELM) is non invasive technique of high-resolution that allows the visualization of deeper skin structures [8, 14]. This technique can characterize visual and morphologically skin lesions [30].

## A.3 Experiment procedure

The dermoscopic images were collected by *Dr. Clémence Berthin*, at the Dermatology department of Angers Hospital, France, showing skin regions at rest and upon heating with the goal of differentiating two different micro circulation states. These images were taken from nine healthy volunteers with an average of $36.5 \pm 11$ years, including eight women and one man, using a *Medicam 800 HD* system with a resolution of $1920 \times 1080$ full HD and 2 megapixels.

All nine volunteers provided written consents to participate and the aim study was done according to *Declaration of Helsinki*.

The collecting region was at 3 cm from the antecubital fossa on the left arm of every volunteer. The heat in that region was locally applied to dilate the blood vessels and increase blood flow. One image was taken at rest, one microcirculation state, and another one was taken after the local application during 2 minutes of a warmed bottle water, the second microcirculation state.

The condition to be fulfilled by all volunteers was the absence of inflammatory dermatitis in the collection skin area.

In addition, several informations about the volunteers were also collected, namely:

- Gender

- Age
- Contraception/THS
- Existence/Absence of Skin Pathologies
- Smoking routine (if existent)
- Phototype
- Medical Treatments (medicines)

# B Normality assessment tests

## B.1 PH2 dataset

The PH2 dataset [79, 80] is composed by 80 dermoscopic images of *common nevus* skin lesions, 80 dermoscopic images of *atypical nevus* skin lesions and 40 dermoscopic images of *melanoma* skin lesions, making a total of 200 dermoscopic images.

In case of having small number of samples, we could have done a non-parametric test right away. Since we had the groups had considerable number of samples (N¿15), we needed to infer what statistical test would be more correct to perform.

In order to identify statistical differences upon the results obtained with $\text{FuzEn}_{C2D}$ for these 200 colored dermoscopic images, we first applied the *Shapiro-Wilk* normality test. This statistical test allowed us to find out for each group and channel, considering an $\alpha = 0.05$, if the obtained entropy values followed a normal distribution or not [81]. We used the MATLAB® function developed by Öner and Deveci Kocakoç [82].

Within each channel, considering the $\text{FuzEn}_{C2D}$ values for three groups (common nevus, atypical nevus and melanoma), we represented in table B.1 the statistical parameters of the *Shapiro-Wilk* test, including the $p$-value for a statistical significance of $\alpha < 0.05$. Through this test, we were able to assess the normality or not of these groups for each image's channel entropy values.

According to the table B.1, only the atypical nevi group for the blue channel follows a normal distribution. The reaming data are not normal- Therefore, in order to differentiate the groups, we should apply a non-parametric test. Knowing we have three groups to compare we should apply the *Kruskal-Wallis* test, an extension of the Wilcoxon rank sum test for more than two groups (non-parametric version of *ANOVA* test).

**Table B.1:** Normality distribution assessment through the Shapiro-Wilk normality test on the PH2 dataset composed by 200 colored dermoscopic images of common nevi, atypical nevi, and melanoma lesions.

| **Channel** $U_K$ | **Skin Condition** | **W (test statistic)** | **p-value** | **Normality (1-normal; 0-not normal)** |
|---|---|---|---|---|
| $U_R$ | Common Nevi | 0.941 | 0.001 | 0 |
| | Atypical Nevi | 0.967 | 0.039 | 0 |
| | Melanoma | 0.924 | 0.010 | 0 |
| $U_G$ | Common Nevi | 0.885 | 0.000 | 0 |
| | Atypical Nevi | 0.937 | 0.001 | 0 |
| | Melanoma | 0.910 | 0.004 | 0 |
| $U_B$ | Common Nevi | 0.899 | 0.000 | 0 |
| | Atypical Nevi | 0.987 | 0.570 | 1 |
| | Melanoma | 0.901 | 0.002 | 0 |

The final statistical test (*Kruskal-Wallis* analysis) is presented in chapter 5 to

identify the statistical differences between the three groups, within entropy of each channel.

## B.2 Volumetric CT scans data

For the study of idiopathic pulmonary fibrosis, we conducted a multiscale analysis on a volumetric dataset composed by two groups of subjects: 26 healthy individuals and 26 patients.

For similar reasons to the PH2 dataset, we evaluated the normality of each group for each scale factor through the *Shapiro-Wilk* test, using a MATLAB® function [82].

In table B.2, we show the values obtained with the *Shapiro-Wilk* normality test, including the $p$-value considering a statistical significance of $\alpha < 0.05$. Moreover, we display which statistical test was chosen to evaluate the significant statistical differences between the two groups considering their distributions. As we can verify, only for $\tau = 2$ both groups are identified as following normal distributions and therefore, we use a *t-test* further on. For the remaining scale factors, we use a *Wilcoxon rank sum* test, equivalent to *Mann-Whitney U* test, and a non-parametric version of the *t-test*.

The final results regarding the volumetric dataset tested are shown and discussed in chapter 5.

**Table B.2:** Normality distribution assessment through the *Shapiro-Wilk* normality test of the volumetric CT scans dataset.

| **Scale Factor** $\tau$ | **Healthy** | | | **Patients** | | | **Statistical test** |
|---|---|---|---|---|---|---|---|
| | **W (test statistic)** | **p-value** | **Normality (1-normal; 0-not normal)** | **W** | **p-value** | **Normality (1-normal; 0-not normal)** | |
| **1** | 0,7008 | 0 | 0 | 0,9501 | 0,2332 | 1 | *Wilcoxon rank sum* |
| **2** | 0,9387 | 0,1249 | 1 | 0,9692 | 0,6014 | 1 | *t-test (unpaired)* |
| **3** | 0,7993 | 0,0002 | 0 | 0,8621 | 0,0025 | 0 | *Wilcoxon rank sum* |
| **4** | 0,7172 | 0 | 0 | 0,8467 | 0,0012 | 0 | *Wilcoxon rank sum* |
| **5** | 0,8363 | 0,0008 | 0 | 0,9457 | 0,1838 | 1 | *Wilcoxon rank sum* |
| **6** | 0,6653 | 0 | 0 | 0,8325 | 0,0007 | 0 | *Wilcoxon rank sum* |
| **7** | 0,6309 | 0 | 0 | 0,6957 | 0 | 0 | *Wilcoxon rank sum* |
| **8** | 0,7931 | 0,0001 | 0 | 0,7944 | 0,0001 | 0 | *Wilcoxon rank sum* |
| **9** | 0,9306 | 0,08 | 1 | 0,8637 | 0,0027 | 0 | *Wilcoxon rank sum* |
| **10** | 0,921 | 0,0475 | 0 | 0,9394 | 0,1299 | 1 | *Wilcoxon rank sum* |

# C Internship Report

The following appendix will be dedicated to present the Internship Report that includes the work developed in LARIS, University of Angers, France inserted in the ERASMUS+ program. Although the entire project involved the collaboration between two laboratories, *LIBPhys-UC* and *LARIS*, the internship period was fully dedicated to approach the fuzzy entropy algorithm in the multidimensional data field. This work allowed to later on make corrections and choose more accurate approaches for the biomedical applications involved.

# Entropy Algorithms for biomedical applications

*Erasmus Internship in LARIS,*
*University of Angers, France*

March of 2019

*Andreia Sofia F. Gaudêncio*[1]

**Supervisor:** PhD Anne Humeau-Heurtier [2]

**Co-Supervisor:** MSc Mirvana Hilal [2]

[1] LIBPhys-UC, Department of Physics, University of Coimbra, Portugal

[2] LARIS, University of Angers, France

*This report has been developed under the supervision of Ph.D. Professor Anne Humeau-Heurtier and Ph.D. Student Mirvana Hilal, during the two month Erasmus internship for Master thesis research, in University of Angers, France*

# Contents

# List of Abbreviations

| | |
|---|---|
| $ApEn_{1D}$ | **Ap**proximate **En**tropy for **1 D**imensional data |
| CT | **C**omputerized **T**omography |
| ECM | **E**xtra**C**ellular **M**atrix |
| ELM | **E**pi**l**uminescence **M**icroscopy |
| EMG | **E**lectro**m**yo**g**raphy |
| $FuzEn_{2D}$ | **Fuz**zy **En**tropy for **2 D**imensional data |
| $FuzEn_{3D}$ | **Fuz**zy **En**tropy for **3 D**imensional data |
| $FuzEn_{C2D}$ | **Fuz**zy Entropy for **C**olored **2 D**imensional data |
| $FuzzyEn_{1D}$ | **Fuzzy En**tropy for **1 D**imensional data (original definition) |
| IPF | **I**diopathic **P**ulmonary **F**ibrosis disease |
| $MIX_{2D}(p)$ | **MIX** for **2 D**imensions |
| $MSE_{1D}$ | **M**ultiscale **S**ample **E**ntropy for **1 D**imensional data |
| $MSE_{2D}$ | **M**ultiscale **S**ample **E**ntropy for **2 D**imensional data |
| PF | **P**ulmonary **F**ibrosis disease |
| ROI | **R**egion **O**f **I**nterest |
| $SampEn_{1D}$ | **Samp**le **En**tropy for **1 D**imensional data |
| $SampEn_{2D}$ | **Sam**ple **En**tropy for **2 D**imensional data |
| SD | **S**tandard **D**eviation |
| UIP | **U**sual **I**nterstitial **P**neumonia |

# 1 Introduction

New entropy measures have been developed these last few years, based on information theory [1]. The goal has been acquiring consistency and removing bias, towards the understanding of signals or images complexity [2]. In addition, a new method to analyze data in multiple scales was proposed [3, 4], collecting more information about the data's complexity. These entropy measures and their multiscale versions can be studied, either in one, two or even three dimensions.

The main goal of the internship was to develop an entropy measure based on *Fuzzy Entropy* to analyze images and sets of images (3D visualization), using for example, dermoscopic images (microscopic images from the skin) and CT (computerized tomography) scans. In this work, therefore, we developed two main algorithms: a bi-dimensional fuzzy entropy measure dedicated to the processing of colored images, $\text{FuzEn}_{C2D}$, and a tri-dimensional fuzzy entropy measure dedicated to processing of 3D data (volumes), $\text{FuzEn}_{3D}$.

In the next chapters, the theoretical background will be presented, including the algorithm's equations and mathematical background for both 2D and 3D versions. This section will include the new $\text{FuzEn}_{2D}$ applied to colored images, $\text{FuzEn}_{C2D}$, that we also developed, based on a previous work by *Santos* et al. [5]. In the end, the multiscale procedure applied to these entropy measures will be explained.

Afterwards, also included in theoretical background, some synthetic signals notions will be explained, including the mathematical definition of *Mix(p) processes*.

Taking into account the main biomedical applications in our work, both will be introduced with some medical notes on the topic. First, Dermoscopy and its applicability to skin lesions diagnosis will be introduced and then, Pulmonary Fibrosis and the use of CT scans for its diagnosis will be approached too.

In the end, results obtained will be shown and discussed, ending this report with the main conclusions for both biomedical applications.

# 2 Theoretical background

## 2.1 Entropy algorithms

Based on information theory, many algorithms to determine data's irregularity have been developed. Chen *et al.* [6, 7] developed a new entropy measure based on *Zadeh's* fuzzy sets [8] with the objective of improving consistency for short amounts of data.

Several studies proposed to use *Sample entropy* [2] ($\text{SampEn}_{1D}$), and its multiscale version, *Multiscale Sample Entropy* [9] ($\text{MSE}_{1D}$) to determine biomedical signals' entropy. For short time series, $\text{SampEn}_{1D}$ starts to show less consistency, leading to some undefined values [6, 7, 9].

$\text{SampEn}_{1D}$ was an improvement from *Approximate entropy* [10] ($\text{ApEn}_{1D}$). $\text{ApEn}_{1D}$ allowed self-matches to occur which lead to biased results [2, 10]. $\text{SampEn}_{1D}$ removed those self-matches in order to prevent this. In addition, templates comparisons already tested are not taken into account in the other iterations [2].

Shortly after, $\text{SampEn}_{2D}$ [11] came along to analyze texture in small images [11]. Afterwards, the multiscale version [9], $\text{MSE}_{2D}$, has also been developed, with a coarse-graining procedure being performed [9]. It revealed itself as a promising algorithm to assess irregularities on images' patterns. The issue of consistency, as it was shown for short time series, was also a drawback for small images/textures [11].

Currently $\text{FuzzyEn}_{1D}$ [6, 7], a more consistent entropy measure, has several related studies that developed many versions: with and without local mean removal, or even removal of both local and global mean [6, 7, 12–14].

As all of these $\text{FuzzyEn}_{1D}$-based measures have presented better results with higher relative consistency, continuity, flexibility in parameter selection and lower dependence on time series length [7]. The next step was to apply this measure on bidimensional data [14] and the associated multiscale versions [5, 12–14]. For EMG (electromyography) signals, $\text{FuzzyEn}_{1D}$ have already revealed to be a measure with best characterization and smaller standard deviations for the results [6].

Bidimensional fuzzy entropy, in a global view, is very similar to unidimensional fuzzy entropy but, with the remaining challenge of reducing the computational cost [14].

$\text{FuzEn}_{2D}$ and $\text{FuzEn}_{3D}$, are extensions from the original algorithm, $\text{FuzzyEn}_{1D}$, defined by *Chen* et al. [6, 7]. However, neither of the algorithms have a baseline removal [1].

## 2.2 Synthetic Signals

### 2.2.1 Mix 2D processes

Based on the one dimensional process, $\text{MIX}_{2D}(p)$ can be defined as [11]:

$$MIX_{2D}(p) = (1 - Z_{i,j})X_{i,j} \; + \; Z_{i,j}Y_{i,j} \tag{1}$$

The signal $X_{i,j} = \sin(\frac{2\pi i}{12}) + \sin(\frac{2\pi j}{12})$ is a sinusoidal image and $Y_{i,j} = [-\sqrt{3}, +\sqrt{3}]$ is a white noise image. $Z_{i,j}$ is a random variable which can assume the value 0 with probability $1 - p$ and $p$ probability of assuming the value 1[11].

### 2.2.2 Mix 3D processes

Based on the one dimensional process, $\text{MIX}_{2D}(p)$ can be defined as:

$$MIX_{3D}(p) = (1 - Z_{i,j,k})X_{i,j,k} \; + \; Z_{i,j,k}Y_{i,j,k} \tag{2}$$

The volume $X_{i,j,k}$ can be defined as a deterministic sinusoidal cube $X_{i,j,k} = \sin(\frac{2\pi i}{12}) \; + \; \sin(\frac{2\pi j}{12}) + \; \sin(\frac{2\pi k}{12})$.

The second volume, $Y_{i,j,k}$ can be defined as random cube following normal distribution between two values, i.e, $Y_{i,j,k} \; = \; [-\sqrt{3}, +\sqrt{3}]$.

Finally, $Z_{i,j,k}$ is a random variable which can assume the value $Z_{i,j,k} = 0$ with probability $1 - p$ and $Z_{i,j,k} = 1$ for $p$ probability.

[1] Since we chose not to perform a baseline removal, the nomenclature for both is $\text{FuzEn}_{2D}$ and $\text{FuzEn}_{3D}$ instead of $\text{FuzzyEn}_{2D}$ and $\text{FuzzyEn}_{3D}$

# 3 Biomedical applications

## 3.1 Dermoscopy applied to skin lesions

Melanoma is the deadliest skin cancer, with an increasing incidence [15]. According to *Bray* et al. [16], the non-melanoma represents 5.8% of all new cancer cases appearing globally and 0.7% number of deaths for 36 types of cancer. In addition, the melanoma represents 1.6% of all new cases world wide and 0.6% global deaths by cancer [16].

Melanoma usually present certain characteristics like asymmetry, irregular borders, uneven color distributions and a diameter wider than 6 mm. These lesions also evolve in size, shape and color [17].

Initially, the medical doctor's opinion was only based in naked eye visualization of the lesions. This procedure was unaided and lacked in accuracy [15, 18]. Also, this process tended to be difficult in identifying early stages of the disease, leading to unnecessary biopsies [15].

Nowadays, the trained specialists use dermoscopic images in order to assist the diagnosis of skin lesions. Dermoscopy or Epiluminescence Microscopy (ELM) is a high-resolution and non invasive technique that allows the visualization of deeper skin structures [15, 17].

Dermoscopy allows to look into the visual and morphological characterization of skin pigmented lesions [18].

Once dermoscopic images were taken into account for the patient's diagnosis, the accuracy improved. Still, if not performed by trained dermatologists there can be limitations. However, even for the specialists, the diagnosis remains subjective [15, 18].

This field still have space to improve in aided diagnosis. The entropy techniques can reveal new information about the dermoscopic images and hopefully, in the future, aid in the diagnosis of skin lesions and cancer, improving the accuracy of diagnosis.

## 3.2 CT scans and pulmonary fibrosis

As *Wynn* [19] mentioned, *Pulmonary Fibrosis* (PF) is a disease with high mortality rate, with the only effective treatment being the lung transplantation. This disease is characterized by a "progressive and irreversible destruction of the lung architecture caused by scar formation" [19]. The fibrotic scar can be developed after a wound healing response getting out of control, leading to extracellular matrix (ECM) components accumulation at the injury site [19]. Such components can be hyaluronic acid, fibronectin, proteoglycans, collagen, among others [19].

The fibrosis is developed if the wound is severe, if there is persistent damaged tissue and deregulation of the repair processes. Since the active inflammatory response is not a prerequisite, this explains why the most common therapies like anti-inflammatory ones, have shown little effect in the idiopathic form of this disease, that does not present signs of detectable inflammation like other types of the disease [19].

Idiopathic pulmonary fibrosis (IPF) is a very severe form of PF with a short life expectancy [19]. Therefore, an early diagnosis is imperative as well as an assessment of the disease stage. To diagnose IPF, high-resolution CT scans are performed in the patient's chest region. The radiologist needs to identify a probable usual interstitial pneumonia (UIP) pattern [20]. This can exclude the need of a surgical lung biopsy [20]. The CT pattern identified by the radiologist can then be classified into one of four categories: typical UIP CT pattern, probable UIP CT pattern, CT pattern indeterminate for UIP and CT features most consistent with non-IPF diagnosis [20].

*Honeycombing* is a key characteristic to identify the UIP pattern and can be defined as "clustered, thick-walle cystic spaces of similar diameters, generally measuring between 3 and 5 mm" [20].

The analysis of these CT scans with entropy-based algorithms might help in the future in an early diagnosis and in stage disease classification.

# 4 Tests

## 4.1 Validation tests

The validation tests were performed to assess their validity with parameters selection, computational time, relative consistency, among other factors.

These algorithms require some parameters definition. Both $\text{FuzEn}_{C2D}$ and $\text{FuzEn}_{3D}$ depend on the embedding dimension, $m$, on tolerance, $r$, and on the exponential function boundary gradient or fuzzy power, $n$, besides the image or volume.

Usually the tolerance, $r$, is defined as a percentage of the standard deviation, SD, of the considered signal, image, or volume. The tolerance was set to $r = 0.2 \times SD_{data}$. This value (i.e. 0.2) was based on literature [2, 4]. When testing the sensitivity to change in $r$ value, the entropy was determined tolerance values between $0.06 \times SD_{data}$ and $0.48 \times SD_{data}$.

The $n$ value was established as $n = 2$, for both bi-, and tridimensional algorithms. This value should be a small integer, maintaining the continuous exponential behavior [6].

The used embedded dimension for $\text{FuzEn}_{C2D}$ was $m = 2$ and for $\text{FuzEn}_{3D}$ we used $m = 3$.

When the analysis involved Mix*(p)* processes, the probability, $p$, was varied between 0 and 1 (step of 0.1).

These validation tests will allow to choose wisely the fixed parameters to perform the tests on medical images.

### 4.1.1 Bidimensional fuzzy entropy applied to colored images

The entropy determination through $\text{FuzEn}_{C2D}$ included the values for three color channels, measuring separately the entropy for each one. In this way, we can specify the most predominant color irregularity, without missing any information given by other color channels. If considering only the maximum distance from the three, during entropy calculations, as performed by *Santos* et al. [5], the specific information for each channel is lost.

The following tests were performed during the internship:

1. Sensitivity to change of tolerance and embedding dimension values on noise-based images (to establish the $r$-, and $m$-value);
2. Entropy verification of a textural image with a checkerboard pattern (for further tests);
3. Analysis of $\text{MIX}_{2D}$ (p) processes (to establish the $m$-parameter; to determine the ability of differentiating different levels of irregularity);
4. Analysis of shuffled versions of $\text{MIX}_{2D}$ (p) processes-based images (to recognize increased randomness).

### 4.1.2 Tridimensional fuzzy entropy

This algorithm was validated on several volumetric synthetic data for further use on volumetric CT scans as biomedival application.

The following tests were performed during the internship:

1. Sensitivity to change of tolerance and embedding dimension values on noise-based volumes (to establish the $r$-, and $m$-value);
2. Analysis of $\text{MIX}_{3D}$ (p) processes-based volumes (to establish the $m$-parameter; to determine the ability of differentiating different levels of irregularity);
3. Analysis of shuffled versions of $\text{MIX}_{3D}$ (p) processes-based volumes (to recognize increased randomness);
4. Analysis of texture-based volumes (to compare different regularity levels of textures);

## 4.2 Medical Images Tests

The first tests performed with $\text{FuzEn}_{3D}$ on CT scans started during the internship. The goal was to select a relevant region of interest for the medical problem in question: idiopathic pulmonary fibrosis that is mainly found on peripheral and basal areas of the lungs. One of the main issues was that a large volume to analyze from each subject would translate in very consuming computational time.

This study included a dataset of 12 individuals: 6 healthy individuals and 6 patients suffering idiopathic pulmonary fibrosis.

- $m =$
- $n = 2$
- $r = 0.2 \times SD_{volume}$
- Each subject had a ROI of $256 \times 256$ pixels, with two studied conditions (at rest and heat), for the subject being studied.

Afterwards, regarding the $\text{FuzEn}_{C2D}$ algorithm, dermoscopic images were studied. These images, obtained using a microscope to record an image from the skin, are usually very helpful to study the evolution of skin related diseases. In this case, the goal was to differentiate two states of microcirculatory conditions: at rest and in presence of vasodilation. The common visual effect of this is the redness of the skin when there is vasodilation.

The parameters used for $\text{FuzEn}_{C2D}$ algorithm, based on the validation tests, were the following ones:

- $m = 2$
- $n = 2$
- $r = 0.2 \times SD^{K}_{ROI}$ with K=R, G,and B.
- Each subject had a ROI of $256 \times 256$ pixels, with two studied conditions (at rest and heat), for the subject being studied.

# 5 Conclusion

The internship was mainly focused on the study of fuzzy entropy measures in the imaging field. Having in mind biomedical bi- and tridimensional applications, the first weeks were dedicated to bibliographic study and development of the algorithms. Once the development phase for each algorithm here studied was concluded, several validation tests were performed, considering previous tests referred in literature. Both algorithms, $\text{FuzEn}_{3D}$ and $\text{FuzEn}_{C2D}$, suffered some adjustments along the way but their final versions here mentioned, were successfully validated for future medical tests.

For the fuzzy entropy in a 3D level, several CT scans were tested, showing promising results. In the future, the guidance of radiologists in choosing the volumes being tested can lead to a improvement of the initial results. In addition, increasing the number of subjects in each group can improve the results and might allow a classification study based on this entropy measure. Ultimately, the goal is to identify subjects that suffer from *Idiopathic Pulmonary Fibrosis* with enough statistical relevance. In a more advanced study, identifying different stages can also be a goal.

$\text{FuzEn}_{C2D}$ as an entropy measure might reveal itself as a powerful tool to assess the presence of skin lesions besides microcirculation conditions. The goal is that this algorithm can distinguish the vasodilation from a relaxed state. This might reveal the ability to detect different situations, associated with the skin morphological and visual characteristics. Further on, tests with dermoscopic images of different skin lesions can also be an interesting study.

# References


[1] Anne Humeau-Heurtier. "Evaluation of Systems' Irregularity and Complexity: Sample Entropy, Its Derivatives, and Their Applications across Scales and Disciplines". In: *Entropy* 20.10 (2018), p. 794. DOI: 10.3390/e20100794.

[2] Joshua S Richman and J Randall Moorman. "Physiological time-series analysis using approximate entropy and sample entropy". In: *American Journal of Physiology-Heart and Circulatory Physiology* 278.6 (2000), H2039–H2049.

[3] Madalena Costa, Ary L. Goldberger, and C.-K. Peng. "Multiscale Entropy Analysis of Complex Physiologic Time Series". In: *Physical Review Letters* 89.6 (2002). DOI: 10.1103/physrevlett.89.068102.

[4] Madalena Costa, Ary L. Goldberger, and C.-K. Peng. "Multiscale entropy analysis of biological signals". In: *Physical Review E* 71.2 (2005). DOI: 10.1103/physreve.71.021906.

[5] Luiz Fernando Segato dos Santos, Leandro Alves Neves, Guilherme Botazzo Rozendo, Matheus Gonçalves Ribeiro, Marcelo Zanchetta do Nascimento, and Thaína Aparecida Azevedo Tosta. "Multidimensional and fuzzy sample entropy (SampEnMF) for quantifying H&E histological images of colorectal cancer". In: *Computers in Biology and Medicine* 103 (2018), pp. 148–160. DOI: 10.1016/j.compbiomed.2018.10.013.

[6] Weiting Chen, Zhizhong Wang, Hongbo Xie, and Wangxin Yu. "Characterization of surface EMG signal based on fuzzy entropy". In: *IEEE Transactions on neural systems and rehabilitation engineering* 15.2 (2007), pp. 266–272.

[7] Weiting Chen, Jun Zhuang, Wangxin Yu, and Zhizhong Wang. "Measuring complexity using FuzzyEn, ApEn, and SampEn". In: *Medical Engineering & Physics* 31.1 (2009), pp. 61–68. DOI: 10.1016/j.medengphy.2008.04.005.

[8] L. A. Zadeh. "Fuzzy Sets". In: *Advances in Fuzzy Systems - Applications and Theory*. World Scientific, 1996, pp. 19–34. DOI: 10.1142/9789814261302_0001.

[9] Luiz EV Silva, Juliano J Duque, Joaquim C Felipe, Luiz O Murta Jr, and Anne Humeau-Heurtier. "Two-dimensional multiscale entropy analysis: Applications to image texture evaluation". In: *Signal Processing* 147 (2018), pp. 224–232.

[10] S. M. Pincus. "Approximate entropy as a measure of system complexity." In: *Proceedings of the National Academy of Sciences* 88.6 (1991), pp. 2297–2301. DOI: 10.1073/pnas.88.6.2297.

[11] LEV Silva, ACS Senra Filho, VPS Fazan, JC Felipe, and LO Murta Junior. "Two-dimensional sample entropy: assessing image texture through irregularity". In: *Biomedical Physics & Engineering Express* 2.4 (2016), p. 045002.

[12] Guo liang Xiong, Long Zhang, He sheng Liu, Hui jun Zou, and Wei zhong Guo. "A comparative study on ApEn, SampEn and their fuzzy counterparts in a multiscale framework for feature extraction". In: *Journal of Zhejiang University SCIENCE A* 11.4 (2010), pp. 270–279. DOI: 10.1631/jzus.a0900360.

[13] Chengyu Liu, Ke Li, Lina Zhao, Feng Liu, Dingchang Zheng, Changchun Liu, and Shutang Liu. "Analysis of heart rate variability using fuzzy measure entropy". In: *Computers in Biology and Medicine* 43.2 (2013), pp. 100–108. DOI: 10.1016/j.compbiomed.2012.11.005.

[14] Mirvana Hilal, Clémence Berthin, Ludivic Martin, Hamed Azami, and Anne Humeau-Heurtir. "Bidimensional Multiscale Fuzzy Entropy and its Application to Pseudoxanthoma Elasticum". (submitted). 2019.

[15] M. Emre Celebi, Noel Codella, and Allan Halpern. "Dermoscopy Image Analysis: Overview and Future Directions". In: *IEEE Journal of Biomedical and Health Informatics* 23.2 (2019), pp. 474–478. DOI: 10.1109/jbhi.2019.2895803.

[16] Freddie Bray, Jacques Ferlay, Isabelle Soerjomataram, Rebecca L. Siegel, Lindsey A. Torre, and Ahmedin Jemal. "Global cancer statistics 2018: GLOBOCAN estimates of incidence and mortality worldwide for 36 cancers in 185 countries". In: *CA: A Cancer Journal for Clinicians* 68.6 (2018), pp. 394–424. DOI: 10.3322/caac.21492.

[17] Fulgencio Navarro, Marcos Escudero-Vinolo, and Jesus Bescos. "Accurate Segmentation and Registration of Skin Lesion Images to Evaluate Lesion Change". In: *IEEE Journal of Biomedical and Health Informatics* 23.2 (2019), pp. 501–508. DOI: 10.1109/jbhi.2018.2825251.

[18] Jeremy Kawahara, Sara Daneshvar, Giuseppe Argenziano, and Ghassan Hamarneh. "Seven-Point Checklist and Skin Lesion Classification Using Multitask Multimodal Neural Nets". In: *IEEE Journal of Biomedical and Health Informatics* 23.2 (2019), pp. 538–546. DOI: 10.1109/jbhi.2018.2824327.

[19] Thomas A. Wynn. "Integrating mechanisms of pulmonary fibrosis". In: *The Journal of Experimental Medicine* 208.7 (2011), pp. 1339–1350. DOI: 10.1084/jem.20110551.

[20] David A Lynch, Nicola Sverzellati, William D Travis, Kevin K Brown, Thomas V Colby, Jeffrey R Galvin, Jonathan G Goldin, David M Hansell, Yoshikazu Inoue, Takeshi Johkoh, Andrew G Nicholson, Shandra L Knight, Suhail Raoof, Luca Richeldi, Christopher J Ryerson, Jay H Ryu, and Athol U Wells. "Diagnostic criteria for idiopathic pulmonary fibrosis: a Fleischner Society White Paper". In: *The Lancet Respiratory Medicine* 6.2 (2018), pp. 138–153. DOI: 10.1016/s2213-2600(17)30433-2.

# Bibliography


[1] Kun Qian, Yaqi Wu, Zhao Zhao, Zhiyong Xu, and Huijie Xu. "Automatic detection, segmentation and classification of snore related signals from overnight audio recording". In: *IET Signal Processing* 9.1 (2015), pp. 21–29. DOI: 10.1049/iet-spr.2013.0266.

[2] Dirk Pevernagie, Ronald M. Aarts, and Micheline De Meyer. "The acoustics of snoring". In: *Sleep Medicine Reviews* 14.2 (2010), pp. 131–144. DOI: 10.1016/j.smrv.2009.06.002.

[3] Katsuhisa Banno and Meir H. Kryger. "Sleep apnea: Clinical investigations in humans". In: *Sleep Medicine* 8.4 (2007), pp. 400–426. DOI: 10.1016/j.sleep.2007.03.003.

[4] Terry Young, Linda Evans, Laurel Finn, and Mari Palta. "Estimation of the Clinically Diagnosed Proportion of Sleep Apnea Syndrome in Middle-aged Men and Women". In: *Sleep* 20.9 (1997), pp. 705–706. DOI: 10.1093/sleep/20.9.705.

[5] J. Mesquita, J. Solà-Soler, J. A. Fiz, J. Morera, and R. Jané. "All night analysis of time interval between snores in subjects with sleep apnea hypopnea syndrome". In: *Medical & Biological Engineering & Computing* 50.4 (2012), pp. 373–381. DOI: 10.1007/s11517-012-0885-9.

[6] Clete A. Kushida, Timothy I. Morgenthaler, Michael R. Littner, Cathy A. Alessi, Dennis Bailey, Jack Coleman, Leah Friedman, Max Hirshkowitz, Sheldon Kapen, Milton Kramer, Teofilo Lee-Chiong, Judith Owens, and Jeffrey P. Pancer. "Practice Parameters for the Treatment of Snoring and Obstructive Sleep Apnea with Oral Appliances: An Update for 2005". In: *Sleep* 29.2 (2006), pp. 240–243. DOI: 10.1093/sleep/29.2.240.

[7] Clete A. Kushida, Michael R. Littner, Timothy Morgenthaler, Cathy A. Alessi, Dennis Bailey, Jack Coleman, Leah Friedman, Max Hirshkowitz, Sheldon Kapen, Milton Kramer, Teofilo Lee-Chiong, Daniel L. Loube, Judith Owens, Jeffrey P. Pancer, and Merrill Wise. "Practice Parameters for the Indications for Polysomnography and Related Procedures: An Update for 2005". In: *Sleep* 28.4 (2005), pp. 499–523. DOI: 10.1093/sleep/28.4.499.

[8] M. Emre Celebi, Noel Codella, and Allan Halpern. "Dermoscopy Image Analysis: Overview and Future Directions". In: *IEEE Journal of Biomedical and Health Informatics* 23.2 (2019), pp. 474–478. DOI: 10.1109/jbhi.2019.2895803.

[9] Freddie Bray, Jacques Ferlay, Isabelle Soerjomataram, Rebecca L. Siegel, Lindsey A. Torre, and Ahmedin Jemal. "Global cancer statistics 2018: GLOBOCAN estimates of incidence and mortality worldwide for 36 cancers in 185 countries". In: *CA: A Cancer Journal for Clinicians* 68.6 (2018), pp. 394–424. DOI: 10.3322/caac.21492.

[10] Nudrat Nida, Aun Irtaza, Ali Javed, Muhammad Haroon Yousaf, and Muhammad Tariq Mahmood. "Melanoma lesion detection and segmentation using deep region based convolutional neural network and fuzzy C-means clustering". In: *International Journal of Medical Informatics* 124 (2019), pp. 37–48. DOI: 10.1016/j.ijmedinf.2019.01.005.

[11] Zongyuan Ge, Sergey Demyanov, Rajib Chakravorty, Adrian Bowling, and Rahil Garnavi. "Skin Disease Recognition Using Deep Saliency Features and Multimodal Learning of Dermoscopy and Clinical Images". In: *Medical Image Computing and Computer Assisted Intervention - MICCAI 2017*. Springer International Publishing, 2017, pp. 250–258. DOI: 10.1007/978-3-319-66179-7_29.

[12] Claus Garbe, Ketty Peris, Axel Hauschild, Philippe Saiag, Mark Middleton, Lars Bastholt, Jean-Jacques Grob, Josep Malvehy, Julia Newton-Bishop, Alexander J. Stratigos, Hubert Pehamberger, and Alexander M. Eggermont. "Diagnosis and treatment of melanoma. European consensus-based interdisciplinary guideline – Update 2016". In: *European Journal of Cancer* 63 (2016), pp. 201–217. DOI: 10.1016/j.ejca.2016.05.005.

[13] Arlo J. Miller and Martin C. Mihm. "Melanoma". In: *New England Journal of Medicine* 355.1 (2006), pp. 51–65. DOI: 10.1056/nejmra052166.

[14] Fulgencio Navarro, Marcos Escudero-Vinolo, and Jesus Bescos. "Accurate Segmentation and Registration of Skin Lesion Images to Evaluate Lesion Change". In: *IEEE Journal of Biomedical and Health Informatics* 23.2 (2019), pp. 501–508. DOI: 10.1109/jbhi.2018.2825251.

[15] Aurora Saez, Begona Acha, Amalia Serrano, and Carmen Serrano. "Statistical Detection of Colors in Dermoscopic Images With a Texton-Based Estimation of Probabilities". In: *IEEE Journal of Biomedical and Health Informatics* 23.2 (2019), pp. 560–569. DOI: 10.1109/jbhi.2018.2823499.

[16] Ralph Peter Braun, Harold S. Rabinovitz, Margaret Oliviero, Alfred W. Kopf, and Jean-Hilaire Saurat. "Dermoscopy of pigmented skin lesions". In: *Journal of the American Academy of Dermatology* 52.1 (2005), pp. 109–121. DOI: 10.1016/j.jaad.2001.11.001.

[17] Christian Sturesson, Jan Nilsson, and Sam Eriksson. "Non-invasive imaging of microcirculation: a technology review". In: *Medical Devices: Evidence and Research* (2014), p. 445. DOI: 10.2147/mder.s51426.

[18] A. Humeau-Heurtier, E. Guerreschi, P. Abraham, and G. Mahe. "Relevance of Laser Doppler and Laser Speckle Techniques for Assessing Vascular Function: State of the Art and Future Trends". In: *IEEE Transactions on Biomedical Engineering* 60.3 (2013), pp. 659–666. DOI: 10.1109/tbme.2013.2243449.

[19] Can Ince. "Hemodynamic coherence and the rationale for monitoring the microcirculation." In: *Critical care (London, England)* 19 Suppl 3 (2015), S8. ISSN: 1466-609X. DOI: 10.1186/cc14726.

[20] Thomas A. Wynn. "Integrating mechanisms of pulmonary fibrosis". In: *The Journal of Experimental Medicine* 208.7 (2011), pp. 1339–1350. DOI: 10.1084/jem.20110551.

[21] Dominic C. Marshall, Justin D. Salciccioli, Barry S. Shea, and Praveen Akuthota. "Trends in mortality from idiopathic pulmonary fibrosis in the European Union: an observational study of the WHO mortality database from 2001–2013". In: *European Respiratory Journal* 51.1 (2018), p. 1701603. DOI: 10.1183/13993003.01603-2017.

[22] F. Soares Pires, P. Caetano Mota, N. Melo, D. Costa, J.M. Jesus, R. Cunha, S. Guimarães, C. Souto-Moura, and A. Morais. "Fibrose pulmonar idiopática: apresentação clínica, evolução e fatores de prognóstico basais numa coorte portuguesa". In: *Revista Portuguesa de Pneumologia* 19.1 (2013), pp. 19–27. DOI: 10.1016/j.rppneu.2012.05.002.

[23] David A Lynch, Nicola Sverzellati, William D Travis, Kevin K Brown, Thomas V Colby, Jeffrey R Galvin, Jonathan G Goldin, David M Hansell, Yoshikazu Inoue, Takeshi Johkoh, Andrew G Nicholson, Shandra L Knight, Suhail Raoof, Luca Richeldi, Christopher J Ryerson, Jay H Ryu, and Athol U Wells. "Diagnostic criteria for idiopathic pulmonary fibrosis: a Fleischner Society White Paper". In: *The Lancet Respiratory Medicine* 6.2 (2018), pp. 138–153. DOI: 10.1016/s2213-2600(17)30433-2.

[24] Ganesh Raghu, Harold R. Collard, Jim J. Egan, Fernando J. Martinez, Juergen Behr, Kevin K. Brown, Thomas V. Colby, Jean-François Cordier, Kevin R. Flaherty, Joseph A. Lasky, David A. Lynch, Jay H. Ryu, Jeffrey J. Swigris, Athol U. Wells, Julio Ancochea, Demosthenes Bouros, Carlos Carvalho, Ulrich Costabel, Masahito Ebina, David M. Hansell, Takeshi Johkoh, Dong Soon Kim, Talmadge E. King, Yasuhiro Kondoh, Jeffrey Myers, Nestor L. Müller, Andrew G. Nicholson, Luca Richeldi, Moisés Selman, Rosalind F. Dudden, Barbara S. Griss, Shandra L. Protzko, and Holger J. Schünemann. "An Official ATS/ERS/JRS/ALAT Statement: Idiopathic Pulmonary Fibrosis: Evidence-based Guidelines for Diagnosis and Management". In: *American Journal of Respiratory and Critical Care Medicine* 183.6 (2011), pp. 788–824. DOI: 10.1164/rccm.2009-040gl.

[25] Ganesh Raghu, Martine Remy-Jardin, Jeffrey L. Myers, Luca Richeldi, Christopher J. Ryerson, David J. Lederer, Juergen Behr, Vincent Cottin, Sonye K. Danoff, Ferran Morell, Kevin R. Flaherty, Athol Wells, Fernando J. Martinez, Arata Azuma, Thomas J. Bice, Demosthenes Bouros, Kevin K. Brown, Harold R. Collard, Abhijit Duggal, Liam Galvin, Yoshikazu Inoue, R. Gisli Jenkins, Takeshi Johkoh, Ella A. Kazerooni, Masanori Kitaichi, Shandra L. Knight, George Mansour, Andrew G. Nicholson, Sudhakar N. J. Pipavath, Ivette Buendía-Roldán, Moisés Selman, William D. Travis, Simon L. F. Walsh, and Kevin C. Wilson. "Diagnosis of Idiopathic Pulmonary Fibrosis. An Official ATS/ERS/JRS/ALAT Clinical Practice Guideline". In: *American Journal of Respiratory and Critical Care Medicine* 198.5 (2018), e44–e68. DOI: 10.1164/rccm.201807-1255st.

[26] A. Nicolas, J. Lemerre, M. Tas, S. Jouneau, and M. Lederlin. "15 minutes pour comprendre : PIC, PINS, PHS, POC..." In: *Journal dimagerie diagnostique et interventionnelle* 2.2 (2019), pp. 73–77. DOI: 10.1016/j.jidi.2019.01.005.

[27] Wen-Qing Li, Eunyoung Cho, Martin A. Weinstock, Suyun Li, Meir J. Stampfer, and Abrar A. Qureshi. "Cutaneous nevi and risk of melanoma death in women and men: A prospective study". In: *Journal of the American Academy of Dermatology* 80.5 (2019), pp. 1284–1291. DOI: 10.1016/j.jaad.2018.12.058.

[28] Harold Kittler, Hubert Pehamberger, Klauss Wolff, and Michael Binder. "Follow-up of melanocytic skin lesions with digital epiluminescence microscopy: Patterns of modifications observed in early melanoma, atypical nevi, and common nevi". In: *Journal of the American Academy of Dermatology* 43.3 (2000), pp. 467–476. DOI: 10.1067/mjd.2000.107504.

[29] Lowell A. Goldsmith. "Diagnosis and Treatment of Early Melanoma". In: *JAMA* 268.10 (1992), p. 1314. DOI: 10.1001/jama.1992.03490100112037.

[30] Jeremy Kawahara, Sara Daneshvar, Giuseppe Argenziano, and Ghassan Hamarneh. "Seven-Point Checklist and Skin Lesion Classification Using Multitask Multimodal Neural Nets". In: *IEEE Journal of Biomedical and Health Informatics* 23.2 (2019), pp. 538–546. DOI: 10.1109/jbhi.2018.2824327.

[31] Sahar Sabbaghi Mahmouei, Mohammad Aldeen, William V. Stoecker, and Rahil Garnavi. "Biologically Inspired QuadTree Color Detection in Dermoscopy Images of Melanoma". In: *IEEE Journal of Biomedical and Health Informatics* 23.2 (2019), pp. 570–577. DOI: 10.1109/jbhi.2018.2841428.

[32] Johann Saphier. "Die Dermatoskopie". In: *Archiv für Dermatologie und Syphilis* 128.1 (1921), pp. 1–19. DOI: 10.1007/bf01991493.

[33] Leon Goldman. "Some Investigative Studies of Pigmented Nevi with Cutaneous Microscopy". In: *Journal of Investigative Dermatology* 16.6 (1951), pp. 407–427. DOI: 10.1038/jid.1951.48.

[34] Cátia S. P. Silva, André R. S. Marcal, Marta A. Pereira, Teresa Mendonça, and Jorge Rozeira. "Separability Analysis of Color Classes on Dermoscopic Images". In: *Lecture Notes in Computer Science*. Springer Berlin Heidelberg, 2012, pp. 268–277. DOI: 10.1007/978-3-642-31298-4_32.

[35] Joshua S. Richman and J. Randall Moorman. "Physiological time-series analysis using approximate entropy and sample entropy". In: *American Journal of Physiology-Heart and Circulatory Physiology* 278.6 (2000), H2039–H2049. DOI: 10.1152/ajpheart.2000.278.6.h2039.

[36] S. M. Pincus. "Approximate entropy as a measure of system complexity." In: *Proceedings of the National Academy of Sciences* 88.6 (1991), pp. 2297–2301. DOI: 10.1073/pnas.88.6.2297.

[37] Douglas E. Lake, Joshua S. Richman, M. Pamela Griffin, and J. Randall Moorman. "Sample entropy analysis of neonatal heart rate variability". In: *American Journal of Physiology-Regulatory, Integrative and Comparative Physiology* 283.3 (2002), R789–R797. DOI: 10.1152/ajpregu.00069.2002.

[38] H. Viertio-Oja, V. Maja, M. Sarkela, P. Talja, N. Tenkanen, H. Tolvanen-Laakso, M. Paloheimo, A. Vakkuri, A. Yli-Hankala, and P. Merilainen. "Description of the Entropytm algorithm as applied in the Datex-Ohmeda S/5tm Entropy Module". In: *Acta Anaesthesiologica Scandinavica* 48.2 (2004), pp. 154–161. DOI: 10.1111/j.0001-5172.2004.00322.x.

[39] Madalena Costa, Ary L. Goldberger, and C.-K. Peng. "Multiscale entropy analysis of biological signals". In: *Physical Review E* 71.2 (2005). DOI: 10.1103/physreve.71.021906.

[40] R.M. Haralick. "Statistical and structural approaches to texture". In: *Proceedings of the IEEE* 67.5 (1979), pp. 786–804. DOI: 10.1109/proc.1979.11328.

[41] Anne Humeau-Heurtier. "Evaluation of Systems' Irregularity and Complexity: Sample Entropy, Its Derivatives, and Their Applications across Scales and Disciplines". In: *Entropy* 20.10 (2018), p. 794. DOI: 10.3390/e20100794.

[42] Constantino Tsallis. *Introduction to Nonextensive Statistical Mechanics*. Springer New York, 2009. DOI: 10.1007/978-0-387-85359-8.

[43] Madalena Costa, Ary L. Goldberger, and C.-K. Peng. "Multiscale Entropy Analysis of Complex Physiologic Time Series". In: *Physical Review Letters* 89.6 (2002). DOI: 10.1103/physrevlett.89.068102.

[44] Chengyu Liu, Ke Li, Lina Zhao, Feng Liu, Dingchang Zheng, Changchun Liu, and Shutang Liu. "Analysis of heart rate variability using fuzzy measure entropy". In: *Computers in Biology and Medicine* 43.2 (2013), pp. 100–108. DOI: 10.1016/j.compbiomed.2012.11.005.

[45] Weiting Chen, Zhizhong Wang, Hongbo Xie, and Wangxin Yu. "Characterization of Surface EMG Signal Based on Fuzzy Entropy". In: *IEEE Transactions on Neural Systems and Rehabilitation Engineering* 15.2 (2007), pp. 266–272. DOI: 10.1109/tnsre.2007.897025.

[46] Weiting Chen, Jun Zhuang, Wangxin Yu, and Zhizhong Wang. "Measuring complexity using FuzzyEn, ApEn, and SampEn". In: *Medical Engineering & Physics* 31.1 (2009), pp. 61–68. DOI: 10.1016/j.medengphy.2008.04.005.

[47] Shuen-De Wu, Chiu-Wen Wu, Kung-Yen Lee, and Shiou-Gwo Lin. "Modified multiscale entropy for short-term time series analysis". In: *Physica A: Statistical Mechanics and its Applications* 392.23 (2013), pp. 5865–5873. DOI: 10.1016/j.physa.2013.07.075.

[48] Shuen-De Wu, Chiu-Wen Wu, Shiou-Gwo Lin, Chun-Chieh Wang, and Kung-Yen Lee. "Time Series Analysis Using Composite Multiscale Entropy". In: *Entropy* 15.3 (2013), pp. 1069–1084. DOI: 10.3390/e15031069.

[49] Pedro Vaz, Diana Capela, Tânia Pereira, Carlos Correia, Requicha Ferreira, Anne Humeau-Heurtier, and João Cardoso. "Use of laser speckle and entropy computation to segment images of diffuse objects with longitudinal motion". In: *Second International Conference on Applications of Optics and Photonics*. Ed. by Manuel Filipe P. C. Martins Costa and Rogério Nunes Nogueira. SPIE, 2014. DOI: 10.1117/12.2060845.

[50] Yi-Cheng Zhang. "Complexity and 1/f noise. A phase space approach". In: *Journal de Physique I* 1.7 (1991), pp. 971–977. DOI: 10.1051/jp1:1991180.

[51] C. E. Shannon. "A Mathematical Theory of Communication". In: *Bell System Technical Journal* 27.3 (1948), pp. 379–423. DOI: 10.1002/j.1538-7305.1948.tb01338.x.

[52] L E V Silva, A C S Senra Filho, V P S Fazan, J C Felipe, and L O Murta Junior. "Two-dimensional sample entropy: assessing image texture through irregularity". In: *Biomedical Physics & Engineering Express* 2.4 (2016), p. 045002. DOI: 10.1088/2057-1976/2/4/045002.

[53] Christopher John Moore. "A Threshold Structure Metric for Medical Image Interrogation: The 2D Extension of Approximate Entropy". In: *2016 20th International Conference Information Visualisation (IV)*. IEEE, 2016. DOI: 10.1109/iv.2016.30.

[54] Christopher Moore and Thomas Marchant. "The approximate entropy concept extended to three dimensions for calibrated, single parameter structural complexity interrogation of volumetric images". In: *Physics in Medicine & Biology* 62.15 (2017), pp. 6092–6107. DOI: 10.1088/1361-6560/aa75b0.

[55] Luiz E.V. Silva, Juliano J. Duque, Joaquim C. Felipe, Luiz O. Murta Jr, and Anne Humeau-Heurtier. "Two-dimensional multiscale entropy analysis: Applications to image texture evaluation". In: *Signal Processing* 147 (2018), pp. 224–232. DOI: 10.1016/j.sigpro.2018.02.004.

[56] Hamed Azami, Javier Escudero, and Anne Humeau-Heurtier. "Bidimensional Distribution Entropy to Analyze the Irregularity of Small-Sized Textures". In: *IEEE Signal Processing Letters* 24.9 (2017), pp. 1338–1342. DOI: 10.1109/lsp.2017.2723505.

[57] Guo liang Xiong, Long Zhang, He sheng Liu, Hui jun Zou, and Wei zhong Guo. "A comparative study on ApEn, SampEn and their fuzzy counterparts in a multiscale framework for feature extraction". In: *Journal of Zhejiang University SCIENCE A* 11.4 (2010), pp. 270–279. DOI: 10.1631/jzus.a0900360.

[58] Mirvana Hilal, Clémence Berthin, Ludivic Martin, Hamed Azami, and Anne Humeau-Heurtier. "Bidimensional Multiscale Fuzzy Entropy and its Application to Pseudoxanthoma Elasticum". 2019, submitted.

[59] Madalena Costa and Ary Goldberger. "Generalized Multiscale Entropy Analysis: Application to Quantifying the Complex Volatility of Human Heartbeat Time Series". In: *Entropy* 17.3 (2015), pp. 1197–1203. DOI: 10.3390/e17031197.

[60] Hamed Azami, Alberto Fernández, and Javier Escudero. "Refined multiscale fuzzy entropy based on standard deviation for biomedical signal analysis". In: *Medical & Biological Engineering & Computing* 55.11 (2017), pp. 2037–2052. DOI: 10.1007/s11517-017-1647-5.

[61] Anne Humeau-Heurtier. "The Multiscale Entropy Algorithm and Its Variants: A Review". In: *Entropy* 17.5 (2015), pp. 3110–3123. DOI: 10.3390/e17053110.

[62] Tiago Marçal, José Basílio Simões, José Moutinho dos Santos, Agostinho Rosa, and João Cardoso. "Snoring Analysis on Full Night Recordings based in the Energy and Entropy in PSG Basal Studies". In: *Proceedings of the International Conference on Bio-inspired Systems and Signal Processing*. SciTePress - Science, and Technology Publications, 2013. DOI: 10.5220/0004245202210227.

[63] Christoph Bandt and Bernd Pompe. "Permutation Entropy: A Natural Complexity Measure for Time Series". In: *Physical Review Letters* 88.17 (2002). DOI: 10.1103/physrevlett.88.174102.

[64] Jinde Zheng, Junsheng Cheng, Yu Yang, and Songrong Luo. "A rolling bearing fault diagnosis method based on multi-scale fuzzy entropy and variable predictive model-based class discrimination". In: *Mechanism and Machine Theory* 78 (2014), pp. 187–200. DOI: 10.1016/j.mechmachtheory.2014.03.014.

[65] Haroldo V. Ribeiro, Luciano Zunino, Ervin K. Lenzi, Perseu A. Santoro, and Renio S. Mendes. "Complexity-Entropy Causality Plane as a Complexity Measure for Two-Dimensional Patterns". In: *PLoS ONE* 7.8 (2012). Ed. by Luís A. N. u. n. e. s. Amaral, e40689. DOI: 10.1371/journal.pone.0040689.

[66] Shuen-De Wu, Chiu-Wen Wu, Shiou-Gwo Lin, Kung-Yen Lee, and Chung-Kang Peng. "Analysis of complex time series using refined composite multiscale entropy". In: *Physics Letters A* 378.20 (2014), pp. 1369–1374. DOI: 10.1016/j.physleta.2014.03.034.

[67] David P. Feldman and James P. Crutchfield. "Structural information in two-dimensional patterns: Entropy convergence and excess entropy". In: *Physical Review E* 67.5 (2003). DOI: 10.1103/physreve.67.051104.

[68] L. A. Zadeh. "Fuzzy Sets". In: *Advances in Fuzzy Systems - Applications and Theory*. World Scientific, 1996, pp. 19–34. DOI: 10.1142/9789814261302_0001.

[69] Jean-Marc Girault and Anne Humeau-Heurtier. "Centered and Averaged Fuzzy Entropy to Improve Fuzzy Entropy Precision". In: *Entropy* 20.4 (2018), p. 287. DOI: 10.3390/e20040287.

[70] Jose Fernando Valencia, Alberto Porta, Montserrat Vallverdu, Francesc Claria, Rafal Baranowski, Ewa Orlowska-Baranowska, and Pere Caminal. "Refined Multiscale Entropy: Application to 24-h Holter Recordings of Heart Period Variability in Healthy and Aortic Stenosis Subjects". In: *IEEE Transactions on Biomedical Engineering* 56.9 (2009), pp. 2202–2213. DOI: 10.1109/tbme.2009.2021986.

[71] Tom Marchant, Mark Murphy, Greg Madden, and Christopher Moore. "Quantifying structure regularity in fluorescence microscopy cell images using a novel multi-dimensional approximate entropy metric". In: *2011 18th IEEE International Conference on Image Processing*. IEEE, 2011. DOI: 10.1109/icip.2011.6116317.

[72] Hamed Azami, Luiz Eduardo Virgilio da Silva, Ana Carolina Mieko Omoto, and Anne Humeau-Heurtier. "Two-dimensional dispersion entropy: An information-theoretic method for irregularity analysis of images". In: *Signal Processing: Image Communication* 75 (2019), pp. 178–187. DOI: 10.1016/j.image.2019.04.013.

[73] Mirvana Hilal and Anne Humeau-Heurtier. "Bidimensional Fuzzy Entropy: Principle Analysis and Biomedical Applications". In: *41st Annual International Conference of the IEEE Engineering in Medicine and Biology Society, Berlin.* (submitted). 2019, accepted.

[74] Luiz Fernando Segato dos Santos, Leandro Alves Neves, Guilherme Botazzo Rozendo, Matheus Gonçalves Ribeiro, Marcelo Zanchetta do Nascimento, and Thaína Aparecida Azevedo Tosta. "Multidimensional and fuzzy sample entropy (SampEnMF) for quantifying H&E histological images of colorectal cancer". In: *Computers in Biology and Medicine* 103 (2018), pp. 148–160. DOI: 10.1016/j.compbiomed.2018.10.013.

[75] Mirvana Hilal, Andreia Sofia F. Gaudêncio, Clémence Berthin, Pedro G. Vaz, João Cardoso, Ludovic Martin, and Anne Humeau-Heurtier. "Bidimensional Colored Fuzzy Entropy Measure: a Cutaneous Microcirculation Study". In: *5th International Conference on Advances in Biomedical Engineering, ICABME19, Lebanon.* 2019, accepted.

[76] Safia Abdelmounaime and He Dong-Chen. "New Brodatz-Based Image Databases for Grayscale Color and Multiband Texture Analysis". In: *ISRN Machine Vision* 2013 (2013), pp. 1–14. DOI: 10.1155/2013/876386.

[77] *"Colored Brodatz Texture Dataset"*. Accessed on 14-02-2019. URL: https://multibandtexture.recherche.usherbrooke.ca/colored\%20_brodatz.html.

[78] Marcin Konowalczyk. *Function randnd for Matlab®*. (2017). Acessed on 10-02-2019. URL: https://www.mathworks.com/matlabcentral/fileexchange/59305-randnd.

[79] Teresa Mendonca, Pedro M. Ferreira, Jorge S. Marques, Andre R. S. Marcal, and Jorge Rozeira. "PH2 - A dermoscopic image database for research and benchmarking". In: *2013 35th Annual International Conference of the IEEE Engineering in Medicine and Biology Society (EMBC)*. IEEE, 2013. DOI: 10.1109/embc.2013.6610779.

[80] Teresa Mendonça, Pedro M. Ferreira, Jorge Marques, and Jorge Rozeira Andre R. S. Marcal. *"PH2 Dataset - A dermoscopic image database for research and benchmarking"*. Accessed on 14-06-2019. URL: https://www.fc.up.pt/addi/ph2\%20database.html.

[81] Marius Marusteri and Vladimir Bacarea. "Comparing groups for statistical differences: how to choose the right statistical test?" In: *Biochemia Medica* (2010), pp. 15–32. DOI: 10.11613/bm.2010.004.

[82] M. Öner and İ. Deveci Kocakoç. *A Compilation of Some Popular Goodness of Fit Tests for Normal Distribution: Their Algorithms and MATLAB Codes (MATLAB)*. 2017.